Theoretical Studies of Dinuclear Transition Metal Complexes and the Exact Solution of the Schrödinger Equation

Yusaku Kurokawa

2009

Preface

"What is your major?" The author is often asked by his old friends. He replies, "My major is quantum chemistry." They always continue, "What is it?" This is a very difficult question. But the author's answer to it is as follows: "Quantum chemistry is one field of theoretical chemistry. So I do not carry out any experiments. Instead of experiment, I calculate everything based on theory with a computer."

However, his answer seems to be unclear for his friends. So, the author adds, "As you know, we can perfectly predict how and where a thrown ball will fly to and land on. It is because the motion of the ball is determined by the Newton's equation. Not only a ball but also everything around us, for example, pen, missile, and even the moon and earth, moves along the Newton's equation. If we solve it, we can know everything in the universe -- people 200 years ago believed so. However, very small particles such as atoms and electrons do not move along the equation. No one in the world exactly knows how these particles behave. So, if we could perfectly know how they behave, we would be able to predict what happens when *A* and *B* are mixed in a beaker before experimentalists actually do it. Furthermore, it would become possible to advise them, 'Mix *A* and *B*, and you will get a beautiful compound *C* without so much efforts, so try it soon!' My major is such a field."

The author, of course, recognizes that some incorrect and overblown explanations are included above. But the last part is one of the ideal situations for theoretical chemists: It is not possible in many cases now to provide useful chemical prediction before experiments actually do. The existing situation is that experimental chemists are going ahead of theoretical chemists, whereas theoreticians are always going ahead of experimentalists in the field of nuclear physics.

"Theoreticians must go ahead of experimentalists", the author has done and will do his study believing this saying.

This thesis is composed of the author's studies during the under graduate and graduate student of Department of Synthetic Chemistry and Biological Chemistry and Department of Molecular Engineering at Graduate School of Kyoto University. Fortunately, the author was working there with a lot of excellent teachers and senior friends there, and was able to receive well education and discipline at the highest level. The author would like to express his deepest appreciation to his supervisor, Prof. Shigeyoshi Sakaki, for his valuable suggestions and careful discussion. The studies in Part I of this thesis were carried out with his full cooperation and instruction. The author also appreciates very much Prof. Hiroshi Nakatsuji, from whom the author was taught the attitude and thought as a scientist. The studies in Part II of this thesis were performed with his full cooperation and instruction. The author is also thankful to Prof. Masahiro Ehara, Associate Prof. Hirofumi Sato, Lecture Jun-ya Hasegawa, Assistant Prof. Ryoichi Fukuda, Assistant Prof. Yoshihide Nakao, Dr. Tomoo Miyahara, Assistant Prof. Satoru Iuchi, Dr. Hiroyuki Nakashima, Dr. Atsushi Ikeda, and Dr. Takashi Hosoya for their kind advices not only about studies but also the author's school life. Acknowledgement is also made to all members of Laboratories of Prof. Sakaki and Prof. Nakatsuji.

Finally, the author sincerely thanks to his father and mother for their understanding, encouraging, and support from all sides.

December 2009

Yusaku I. Kurokawa

Contents

General Introduction

1. What is “Theoretical Chemistry”?

First of all, the author wishes to mention his idea about “theoretical chemistry”, before introducing the author’s study. The role and/or goal of theoretical study in science are, generally speaking, elucidation and prediction of natural phenomena. It is impossible to do those only by experiments.

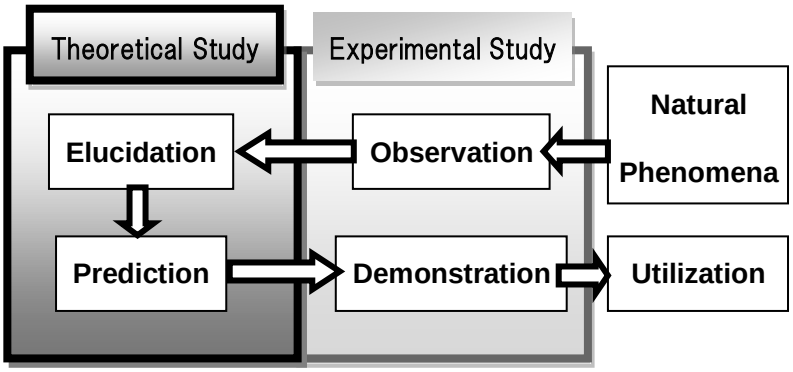

Figure 1. The role of theoretical study

There are two approaches to predict natural phenomena. One is inductive method, where prediction is given based on accumulated experiences. If we accumulate a lot of experiences, the prediction will be trustworthy. This methodology is very powerful within our experiences. However, this approach is not useful at all for new phenomena which we have never experienced. The other approach to predict phenomena is deductive method, where prediction is provided from principles. If the starting principles are correct and reliable enough for everyone, the prediction will be correct and reliable.

In “theoretical chemistry”, chemical compound and chemical phenomena are investigated with theory. This implies that the most important roles and/or goals of theoretical chemistry are to elucidate and predict chemical phenomena, such as geometry and chemical property of compound, chemical reaction, and so on. In particular, the author is much interested in elucidation and prediction of chemical

compounds based on electronic structure theory. To achieve such purposes, we need "quantum chemistry".

2. Quantum chemistry starting from the Schrödinger equation

The starting principle of quantum chemistry is the Pauli's principle and the Schrödinger equation (SE). The original SE includes time parameter, *t*. However we eliminate it and use time-independent SE when we are interested in time-independent state of phenomena:

$$(H - E)\psi = 0. \tag{1}$$

Any states of time-independent systems are described by the solution of the SE, eq. (1): In other words, the atoms and molecules are described by the solution of the SE. Therefore, if we could solve the SE exactly, we could understand and predict any chemical phenomena. However, it is very difficult to exactly, generally, and analytically solve the SE, even though it consists of only three strings.

Instead of solving the SE directly, quantum chemists and physicists have tried to solve it by introducing various kinds of approximations; for example, Born-Oppenheimer approximation and neglect of nuclear size *etc*. are often employed as approximation of Hamiltonian. Hartree-Fock approximation, LCAO (linear combination of atomic orbital) expansion, limited basis set expansion and Gauss type function *etc.* are often employed as approximation on wave function. From the viewpoint of science, we must evaluate the validity of approximations introduced. It is, however, impossible in many cases to validate the approximations because we cannot have the exact solution of the SE except for very simple case.

Frankly speaking, the SE itself includes some approximations: we have already experienced that we can neglect the relativistic and quantum electrodynamics (QED) effects when we treat light atoms and molecules.

Instead of comparison with the exact solution of the SE, quantum chemists often compare their computed results with the corresponding results of experiment. If their computational results agree well with experiments, the approximations employed are regarded to be acceptable. Many computational methods depending on various levels of approximation have been proposed, such as Hartree-Fock (HF) method, functionals of the Density Functional Theory (DFT) method, Complete Active Space Self Consistent Field (CASSCF) method, Full Configuration Interaction (Full CI) method, F12 method, *etc*. All of these methods are based on one or more approximations. The choice of method is made depending on one's experiences and knowledge; what method should be applied to the target to present good results. This is the reason why modern quantum chemistry is criticized to be "state-of-the-art".

Of course, we must remember that though computational results with certain approximate method agree well with experimental results, they do not always agree with other systems. Thus, we need to accumulate a lot of experiences to apply theoretical method to chemical phenomena of various kinds. Once the approximation and/or method are confirmed to be reliable about systems in interest, we can employ it and investigate other similar systems. In this regard, the theoretical study in chemistry is still not the perfect.

3. Purpose of this thesis

This thesis consists of Part I and Part II. The Part I is titled "Theoretical Study of Dinuclear Transition Metal Complexes", where the author employed the post-HF and DFT methods. The title of Part II is "The Exact Solution of the Schrödinger Equation", where the author directly solved the SE.

Part I is contains three chapters. In Chapter 1, metal-metal multiple bonds were investigated by the DFT, CASSF, and MRMP2 methods. Since the discovery of the

Re-Re quadruple bond by Cotton, a lot of the interests in the similar compounds possessing metal-metal multiple bond has been devoted to the elucidation of their geometry, bonding nature, and electronic structure. Nowadays, we recognize growing interests these compounds in wide areas of chemistry such as inorganic chemistry, physical chemistry, material science and so on. These compounds provide a rich and fruitful field of research because the metal-metal bonding nature is expected to be completely different from those of organic molecules. However, quantum chemists have failed in obtaining satisfactory agreements of their computational result about these compounds with the corresponding experimental ones because of their poor approximations employed. Thus, theoretical chemists do not have enough experience of theoretical study of such compounds possessing metal-metal multiple bonds. In particular, dinuclear chromium complex is one of the most difficult and challenging species to describe its electronic structure and bonding nature because the chromium atom itself suffers from strong correlation effects. In Part I, the author tried to elucidate them through post-HF methods.

In Chapter 1, the author successively investigated dinuclear transition metal (TM) complexes with the MRMP2 method which can incorporate both non-dynamical and dynamical correlation effects. In Chapters 2 and 3, the author investigated the inverted sandwich type complexes (ISTC) of the first- and second-row TMs with the DFT and MRMP2 method like Chapter 1. Since ISTC of chromium was synthesized for the first time as the ISTC of TMs very recently, its electronic structure and bonding nature have not been clarified. In these chapters, the author not only clarified them but also provided theoretical predictions of the spin multiplicities of various ISTCs of TMs.

Part II is composed of Chapters 4 and 5, where the author solved the SE of the hydrogen molecule and helium atom. As introduced above, the SE was believed to be too complicated to solve it in general case. The only exceptions are some of one

electron systems and non-real systems such as hydrogen atom, a particle in a box, harmonic oscillator, and Hooke's atom *etc*. This "fact" was true until the end of the 20^{th} century, as it was stated in many textbooks of quantum chemistry. In 2004, Prof. Nakatsuji proposed a new method to solve the SE exactly and analytically without any approximation. His method is named the Free Iterative Compliment Interaction (ICI) method. In Chapter 4, the author applied it for the first time to molecular system, hydrogen molecule. In Chapter 5, the author introduced the exponential integral (Ei) function, which is a new type of wave function and reported that the exact wave function of the helium atom is described by the Ei function. The Ei function was naturally derived from the Free ICI concept. The author strongly believes that his works will provide a lot of fundamental information in the future.

Part I

Theoretical Study of Dinuclear Transition Metal Complexes

Chapter 1

Bonding Nature of Open Lantern–type Dinuclear Cr(II) Complexes. Theoretical Study with MRMP2 Method

1. Introduction

Metal-Metal multiple bond is one of the interesting and challenging research targets in inorganic, physical, and theoretical chemistries. For instance, Re-Re quadruple bond was very previously proposed by Cotton and his collaborators,[1, 2] but correct understanding of its bonding nature has been recently achieved by theoretical works with CASPT2 and MRMP2 methods.[3, 4] Another good example is dinuclear Cr compounds including Cr-Cr multiple bond. Cr dimer, Cr_2, is of considerable interest because it is believed to possess a hextuple Cr-Cr bond in a formal sense, which is the largest bond order at this moment.[5] Theoretical calculation of this compound is challenging because of the presence of very large electron correlation effects. Actually, a lot of theoretical works have been carried out with sophisticated methods including CASPT2, MR-CI, and similar methods.[6] Also, RCrCrR (R = C_6H_3-2,6 (C_6H_3-2,6-Pr^i_2)$_2$), which was recently synthesized by Power and his collaborators,[7] has drawn a lot of interests because it possesses a Cr-Cr quintuple bond and its trans-bent geometry is similar to that of E_2R_2 molecule bearing E-E triple bond (E = Si to Pb; R = bulky

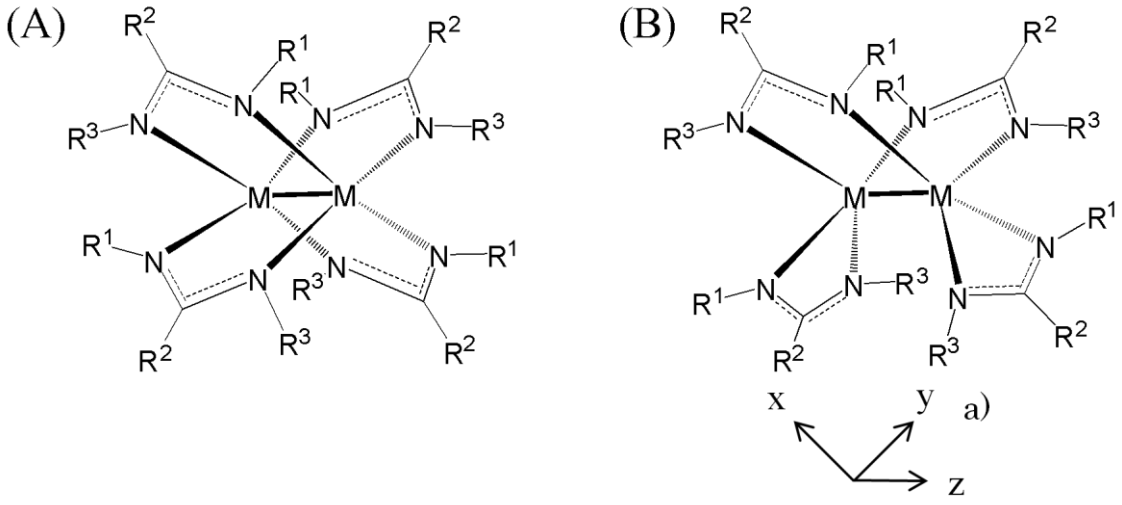

Scheme 1-1. (A) Lantern type complex and (B) open lantern type complex
[a] z-axis is along the M-M bond, and the x and y axes are along M-N bonds.

aryl or silyl ligand). Theoretical studies of this compound have been carried out with DFT[8, 9] and CASPT2 methods.[10] Though the Cr-Cr bond order was calculated to be 4.64 with the DFT method, it was 3.52 by the CASSCF calculation, indicating that the non-dynamical correlation effects are considerably large in this complex.[9] Recently, lantern-type Cr(I) dinuclear complex was experimentally reported.[11] Interestingly, its Cr-Cr distance is very short.

Besides these dinuclear Cr(I) complexes, experimental and theoretical studies on dinuclear Cr(II) complexes bearing Cr-Cr quadruple bond have been reported previously.[12-28] Though most of them take lantern type structure (Scheme 1-1(A)), open-lantern type dinuclear Cr(II) complex was recently reported (Scheme 1-1(B)).[28] This complex possesses short Cr-Cr bond (1.9601 Å) like $[Li(L)]_4[Cr_2Me_8]$ (Cr-Cr = 1.98 Å, L = THF or Et_2O) and [(tetraazaannulene)Cr_2] (Cr-Cr = 2.096 Å). Interestingly, this complex easily dissociates to two mononuclear Cr(I) complexes in solution unlike $[Li(L)]_4[Cr_2Me_8]$ (L = THF or Et_2O) in spite of its short Cr-Cr bond, even when Lewis base is not added. Though there remain these interesting issues to be investigated, theoretical study of the open-lantern type dinuclear Cr(II) complex has not been carried out yet, to our best knowledge.

In this theoretical study, we investigated open-lantern type dinuclear Cr(II) complex, $[Cr(R^1NC(R^2)NR^3)_2]_2$ (R^1 = Et, R^2 = Me, and R^3 = ^{t}Bu) (**R1**), with DFT, CASSCF, and MRMP2 methods. Our purposes here are to clarify the Cr(II)-Cr(II) bonding nature and to characterize the Cr(II)-Cr(II) quadruple bond by making comparison with the Mo(II)-Mo(II) quadruple bond, and to present clear comparison between the Cr(II)-Cr(II) quadruple and Si-Si multiple bonds.

2. Models and Computational Details

Because the real complex, $[Cr(R^1NC(R^2)NR^3)_2]_2$ (R^1 = Et, R^2 = Me, and R^3 = ^{t}Bu) (**R1**), is very large, we employed small model (**M1**) in preliminary calculations. In **M1**, all alkyl substituents were replaced with hydrogen atoms, as shown in Figure 1-1.

Their geometries were optimized at various Cr-Cr distances in singlet spin state, where the DFT method was employed with B3LYP functional.[29] Potential energy surface (PES) was calculated with the MRMP2 method,[4] where CASSCF wave function was taken as the

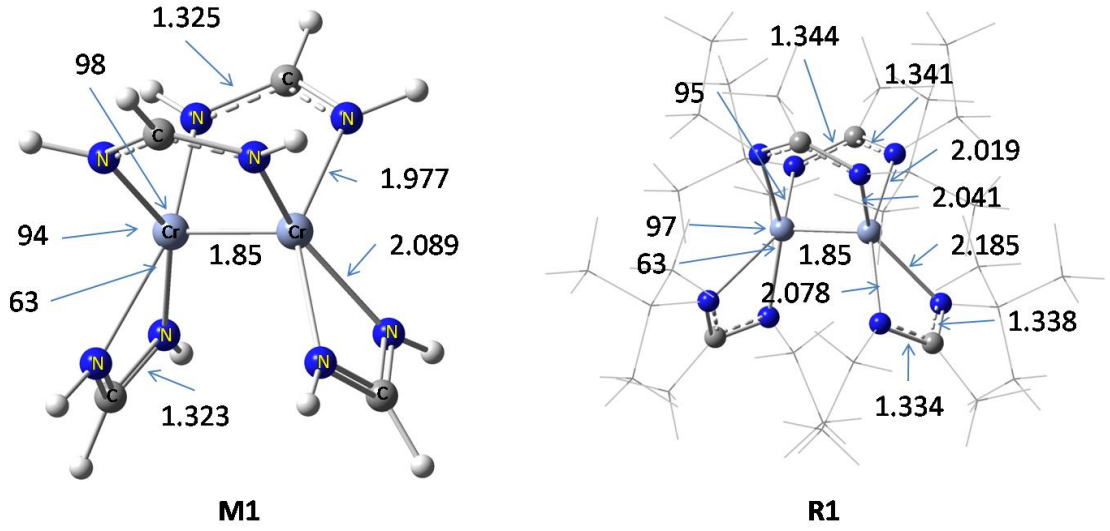

Figure 1-1. DFT-optimized geometries of $[Cr(R^1NC(R^2)NR^3)_2]_2$ ($R^1 = R^2 = R^3 = H$) (**M1**) and $[Cr(R^1NC(R^2)NR^3)_2]_2$ (R^1 = Et, R^2 = Me, and R^3 = ^{t}Bu) (**R1**) at R(Cr-Cr) = 1.85 Å. **M1** and **R1** take C_{2v} and C_2 symmetries, respectively. In **R1**, the high level region of the ONIOM calculation is drawn with balls and sticks, and the low level region is drawn with wire frame. Length in Å and angle in degree.

reference. In the CASSCF calculation, 8 electrons in such 8 orbitals as σ_d, $\pi 1_d$, $\pi 2_d$, δ_d, σ_d^*, $\pi 1_d^*$, $\pi 2_d^*$, and δ_d^* were taken as active space because these orbitals exist around HOMO and LUMO, as shown in Scheme 1-2. This calculation is named CASSCF(8,8) hereafter. The $d_{x^2-y^2}$ orbital was excluded from the active space because it exists at much high energy due to the strong anti-bonding interaction with the lone pair orbitals of ligands; see Scheme 1-1 for the coordinate. This active space is the same as those of CASPT2 and MRMP2 calculations of dinuclear Re complex, $[Re_2Cl_8]^{2-}$, bearing a Re-Re quadruple bond.[30, 31]

The total energy of the real system, E_{real}, was evaluated by the ONIOM method.[32] The ONIOM-calculated energy is represented as

$$E_{real} = E_{real,\,low} - E_{model,\,low} + E_{model,\,high}\,, \qquad (1)$$

where $E_{real,\,low}$ and $E_{model,\,low}$ are the energies of the real and model systems calculated at low level of theory, respectively, and $E_{model,\,high}$ is that of the model system calculated at high level of theory. These energy values were calculated separately and assembled according to eq. (1). We applied the DFT method to the whole system and either CASSCF or MRMP2

method to the high-quality region throughout the present study. They are named ONIOM(CASSCF:DFT) and ONIOM(MRMP2:DFT), respectively, hereafter.

Core electrons (up to 2p) of Cr were replaced with Stuttgart-Dresden-Born effective core potentials (ECPs), and its valence electrons were represented with a (311111/22111/411/1) basis set.[33] This basis set is named SDD hereafter. For C, N, and H, cc-pVDZ basis sets were employed. The s-, p-, and d-type augmented functions were added to N because it is anionic in the ligand. The SDD basis set was employed for Mo, too.

To clarify the characteristic features of the Cr-Cr quadruple bond, we compared it with the Si-Si triple bond of Si_2H_2 molecule (**S1**) and Si-Si double bond of Si_2H_4 molecule (**S2**). The geometries of **S1** and **S2** were optimized in C_{2h} symmetry by the DFT method with B3LYP functional, where cc-pVTZ basis sets were employed for Si and cc-pVDZ basis set for H. The optimized geometries are shown in Figure A1-1. Also, we carried out the CASSCF(6,6) calculation of **S1** and the CASSCF(4,4) calculation of **S2** using the

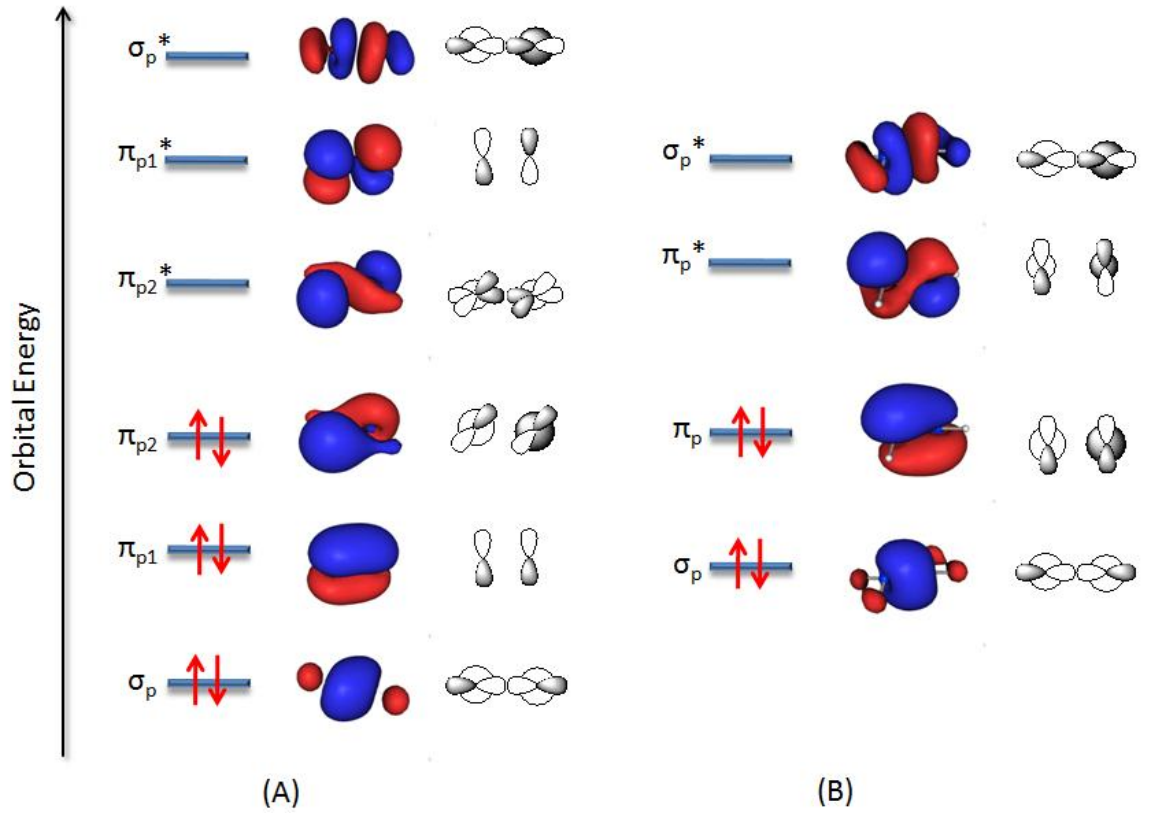

Scheme 1-3. The active orbitals employed in the CASSCF(6,6) calculation of HSi≡SiH (**S1**) (A) and the CASSCF(4,4) calculation of $H_2Si=SiH_2$ **S2** (B). Arrows represent Hartree-Fock configuration.

DFT-optimized geometry. In the CASSCF(6,6) calculation of **S1**, 6 electrons in such 6 orbitals as σ_p, $\pi 1_p$, $\pi 2_p$, σ_p^*, $\pi 1_p^*$, and $\pi 2_p^*$ were taken as an active space, as shown in Scheme 1-3. In the CASSCF(4,4) calculation of **S2**, 4 electrons in such 4 orbitals as σ_p, π_p, σ_p^*, and π_p^* were taken as an active space. We ascertained that the shapes of Kohn-Sham orbitals of **S1** are similar to those of real compounds, 1, 1, 4, 4-tetrakis[bis(trimethslsilyl)methyl]-1, 4-diisopropyl-2-tetrasilyne;[34] see Supporting Information Figure A1-2.

Gaussian 03[35] and GAMESS[36] program packages were used for DFT, CASSCF, and MRMP2 calculations, respectively. Molecular orbitals (MOs) were drawn with Molekel program.[37]

3. Results and Discussion

3.1 Preliminary Examination of Model Compound $[Cr(R^1NC(R^2)NR^3)_2]_2$ ($R^1 = R^2 = R^3 =$ H) (M1)

We optimized the structure of **M1** at various Cr-Cr distances under C_{2v} symmetry, as shown in Figure 1-1. Very small imaginary frequency with B_2 symmetry does not disappear in the optimized geometry,[38] probably because the Cr-Cr distance is fixed. In the DFT-optimized geometry, the Cr-Cr distance is 1.757 Å, as shown in Figure 1-2, which is much shorter than

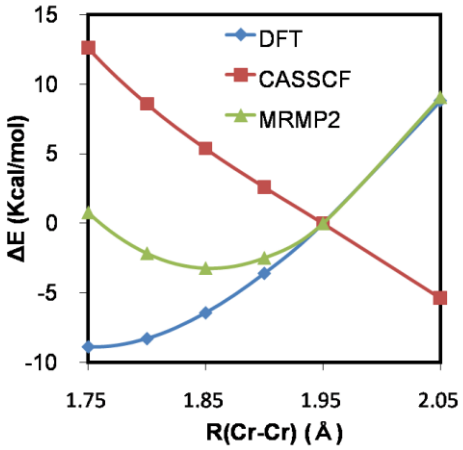

Figure 1-2. PESs of $[Cr(R^1NC(R^2)NR^3)_2]_2$ ($R^1 = R^2 = R^3 =$ H) (**M1**) calculated by the DFT, CASSCF, and MRMP2 methods. The energy of R(Cr-Cr) = 1.95Å is taken to be standard (energy zero); E_{DFT} = -771.82445 a.u., E_{CASSCF} = -766.90180 a.u., and E_{MRMP2} = -769.85197 a.u. at this distance.

the experimental value by 0.2 Å. One can expect that geometry optimization of **M1** in nonet state yields longer Cr-Cr distance. However, the minimum energy was not observed in the range of R(Cr-Cr) = 1.85 Å to 3.6 Å, and the nonet spin state is more than 100 kcal/mol above the singlet spin state at R(Cr-Cr) = 1.85 Å; see Supporting Information Figure A1-4. Also, we carried out the CASSCF(8,8) calculation of **M1**, using the DFT-optimized geometry. The PES smoothly decreases as the Cr-Cr distance increases unlike the DFT-calculated PES, as shown in Figure 1-2. However, the equilibrium structure is not presented in the range of R(Cr-Cr) = 1.75 Å to 2.15 Å. Completely different PES between CASSCF and DFT calculations suggests the presence of very large non-dynamical correlation effect.

In MRMP2 calculations, the Cr-Cr distance is optimized to be 1.855 Å (Figure 1-2), which is moderately longer than that of the DFT-optimized distance by 0.1 Å but moderately shorter than that of the experimental value by 0.1 Å.[28] These results suggest that both of non-dynamical and dynamical correlations play important roles to present correctly the Cr-Cr distance of **M1**.

The occupation number of each natural orbital was calculated with the CASSCF(8,8) method, as shown in Table 1-1. The difference in the occupation number between δ_d and δ_d* is

TABLE 1-1: The occupation numbers of the natural orbitals and the bond order of $[Cr(R^1NC(R^2)NR^3)_2]_2$ ($R^1 = R^2 = R^3 = H$) (**M1)**, $[Cr(R^1NC(R^2)NR^3)_2]_2$ (R^1 = Et, R^2 = CH_3, and R^3 = ^{t}Bu) (**R1)**, and $[Mo(R^1NC(R^2)NR^3)_2]_2$ ($R^1 = R^2 = R^3 = H$) (**Mo1**).[a]

	M1	**R1**	**Mo1**
R(M-M) (Å)	1.85	1.85	2.15
σ_d	1.740	1.723	1.895
$\pi 1_d$	1.707	1.693	1.88
$\pi 2_d$	1.713	1.683	1.884
δ_d	1.372	1.299	1.753
δ_d*	0.629	0.702	0.247
$\pi 2_d$*	0.294	0.318	0.117
$\pi 1_d$*	0.287	0.308	0.12
σ_d*	0.259	0.276	0.104
Bond Order			
σ_d	0.741	0.724	0.896
π_d	1.420	1.375	1.764
δ_d	0.372	0.299	0.753
Total	2.532	2.397	3.412

[a] The CASSCF(8,8) method was employed.

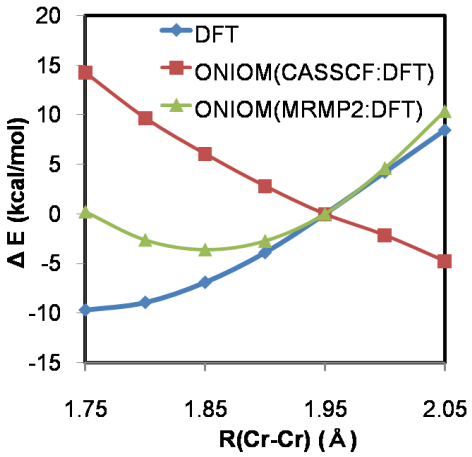

Figure 1-3. PESs of $[Cr(R^1NC(R^2)NR^3)_2]_2$ (R^1 = Et, R^2 = Me, and R^3 = ^{t}Bu) (**R1)** calculated by the DFT, ONIOM(CASSCF:DFT), and ONIOM(MRMP2:DFT) methods. The energy of R(Cr-Cr)=1.95Å is taken to be standard (energy zero); E_{DFT} = -1872.52005 a.u., $E_{ONIOM(CASSCF:DFT)}$ = -1867.60636 a.u., and $E_{ONIOM(MRMP2:DFT)}$ = -1870.55263 a.u. at this distance.

orbitals is 0.743, which is much smaller than 2. This is the main source of the large non-dynamical correlation. The bond order is defined as one half of the difference between the sum of occupation numbers in the bonding orbitals and that of the anti-bonding orbitals. In **M1**, the bond order is evaluated to be 2.53 at R(Cr-Cr) = 1.850 Å. This value is much smaller than the formal bond order (4.0) of the quadruple bond. This very small bond order arises from the occupations of anti-bonding orbitals, σ_d^*, $\pi 1_d^*$, $\pi 2_d^*$, and δ_d^* orbitals, which will be discussed below in more detail.

3.2 Geometry and Bonding Nature of Real Complex, $[Cr(R^1NC(R^2)NR^3)_2]_2$ (R^1 = Et, R^2 = Me, and R^3 = ^{t}Bu) (R1)

The geometry of **R1** was optimized by the DFT method at various Cr-Cr distances. The optimized geometry at each Cr-Cr distance takes C_2 symmetry in which no imaginary frequency is observed. The DFT-calculated PES decreases as the Cr-Cr distance becomes shorter but the equilibrium structure is not found in the range R(Cr-Cr) > 1.75 Å, as shown in Figure 1-3. In contrast to the DFT-calculated PES, the ONIOM(CASSCF:DFT)-calculated PES decreases as the Cr-Cr distance becomes longer. The equilibrium structure is not found, too, in the range of R(Cr-Cr) < 2.05 Å. On the other hand, the ONIOM(MRMP2:DFT)-calculated PES exhibits the minimum at R(Cr-Cr) = 1.851 Å.

These features of the PESs are essentially the same as those of **M1**.

The Cr-Cr bond order is evaluated to be 2.40 with the CASSCF(8,8) method at R(Cr-Cr) = 1.850 Å. This value is moderately smaller than that of **M1**, as shown in Table 1-1. It is noted that the π_d and δ_d bond orders are considerably smaller in **R1** than in **M1** by 0.045 and 0.073, respectively, though the σ_d bond order is slightly smaller in **R1** than in **M1** by 0.017. The smaller π_d and δ_d bond orders arise from the fact that **M1** takes C_{2v} symmetry but **R1** takes C_2 symmetry. The d_π and d_δ atomic orbitals of one Cr atom overlap worse with those of the other Cr atom in the C_2 symmetry than in the C_{2v} symmetry, because the d_π and d_δ atomic orbitals of one Cr atom twist with respect to those of the other Cr atom in the C_2 symmetry. Thus, their bonding interactions become weaker in **R1**. However, the σ_d bond order is not different very much between **M1** and **R1** because the d_σ atomic orbital of one Cr atom overlaps well with that of the other Cr atom in both C_2 and C_{2v} symmetries; note that the twist distortion little changes the direction of d_σ atomic orbital.

The CASSCF(8,8) wave function of the high quality region of **R1**, $\Psi_{\mathbf{R1},\,\mathrm{CAS(8,8)}}$, is

TABLE 1-2: Important electron configurations and their coefficients $[Cr(R^1NC(R^2)NR^3)_2]_2$ (R^1 = Et, R^2 = Me, and R^3 = ^{t}Bu) (**R1**) and $[Mo(R^1NC(R^2)NR^3)_2]_2$ ($R^1 = R^2 = R^3$ = H) (**Mo1**)[a]

R1		**Mo1**	
coefficients	configuration	coefficients	configuration
0.63275	$\sigma_d^2\pi 1_d^2\pi 2_d^2\delta_d^2$	0.86716	$\sigma_d^2\pi 1_d^2\pi 2_d^2\delta_d^2$
-0.39494	$\sigma_d^2\pi 1_d^2\pi 2_d^2\delta_d^{*2}$	-0.25924	$\sigma_d^2\pi 1_d^2\pi 2_d^2\delta_d^{*2}$
-0.15446	$\sigma_d^2\pi 1_d^2\delta_d^2\sigma_d^{*2}$	-0.11754	$\sigma_d^2\pi 1_d^2\delta_d^2\pi 1_d^{*2}$
0.11381	$\sigma_d^2\pi 1_d^2\delta_d^{*2}\sigma_d^{*2}$	-0.10346	$\sigma_d^2\pi 1_d^2\pi 2_d^2\pi 1_d^{*2}$
-0.19669	$\sigma_d^2\pi 1_d^2\pi 2_d^1\delta_d^1\delta_d^{*1}\sigma_d^{*1}$	-0.11221	$\sigma_d^2\pi 2_d^2\delta_d^2\pi 2_d^{*2}$
-0.15384	$\sigma_d^2\pi 1_d^1\pi 2_d^2\delta_d^1\delta_d^{*1}\pi 1_d^{*1}$	-0.13737	$\sigma_d^2\pi 1_d^2\pi 2_d^1\delta_d^1\delta_d^{*1}\pi 1_d^{*1}$
-0.13033	$\sigma_d^2\pi 1_d^1\pi 2_d^2\delta_d^1\delta_d^{*1}\pi 2_d^{*1}$	-0.13360	$\sigma_d^1\pi 1_d^2\pi 2_d^2\delta_d^1\delta_d^{*1}\sigma_d^{*1}$
-0.12491	$\sigma_d^1\pi 1_d^2\pi 2_d^2\delta_d^1\delta_d^{*1}\pi 2_d^{*1}$	0.10762	$\sigma_d^2\pi 1_d^1\pi 2_d^2\delta_d^1\delta_d^{*1}\pi 2_d^{*1}$
0.12102	$\sigma_d^1\pi 1_d^2\pi 2_d^2\delta_d^1\delta_d^{*1}\pi 1_d^{*1}$		
-0.10468	$\sigma_d^2\pi 1_d^1\pi 2_d^1\delta_d^2\pi 2_d^{*1}\sigma_d^{*1}$		
-0.10186	$\sigma_d^2\pi 1_d^1\pi 2_d^1\delta_d^2\pi 2_d^{*1}\pi 1_d^{*1}$		

[a] The CASSCF(8,8) method was employed.

represented as follows:

$$\psi_{\mathbf{R1},\mathrm{CAS}(8,8)} = 0.633\Phi_{\mathrm{main}} - 0.395\Phi_{\delta^2\rightarrow\delta^{*2}} - 0.197\Phi_{\pi 2^2\delta^2\rightarrow\pi 2\delta\delta^*\sigma^*} - 0.154\Phi_{\pi 2^2\rightarrow\sigma^{*2}} - 0.154\Phi_{\pi 1^2\delta^2\rightarrow\pi 1\delta\delta^*\pi 1^*} + \cdots \quad (2)$$

where δ, δ^* etc. represent δ_d, δ_d^* etc. (see Scheme 1-2), respectively, here. The main configuration is $\sigma_d^2\,\pi 1_d^2\,\pi 2_d^2\,\delta_d^2$ which is the same as the Hartree-Fock configuration. However, its expansion coefficient is only 0.633 and its weight is 40.1 %. The second leading configuration is $\sigma_d^2\,\pi 1_d^2\,\pi 2_d^2\,\delta_d^{*2}$, the weight of which is very large, being over one-third of that of the main configuration. This configuration corresponds to excitation of two electrons from d_δ to d_δ^*, as expected. The expansion coefficient of the third leading configuration, $\sigma_d^2\,\pi 1_d^2\,\pi 2_d^1\,\delta_d^1\,\delta_d^{*1}\,\sigma_d^{*1}$, is unexpectedly large, 0.197, too. Also, it is noted that not π_d^* orbital but σ_d^* orbital participates in the third and fourth excited configurations (see Table 1-2). This is against our expectation that the $\delta_d\rightarrow\pi_d^*$ excited configuration is energetically lower than the $\delta_d\rightarrow\sigma_d^*$ excited configuration because the σ_d^* is in general at higher energy than the π_d^*. This unexpected result will be discussed below in detail. The other configurations with large expansion coefficients are listed in Table 1-2. Apparently, the wave function of **R1** consists of many electron configurations including various kinds of excitations. This result clearly indicates that the non-dynamical electron correlation is very large.

We wish to mention here the possibility that the third and fourth leading configurations involve one-electron excitation due to mixing of metal d_δ, d_π and d_σ orbitals because of the low symmetry (C_2) of **R1** and that it is not any more the case for the open-lantern complexes.[21b] To check this possibility, we carried out CASSCF(8,8) calculation of closed-lantern type dinuclear Cr(II) complex taking D_{2h} symmetry (Scheme 1-1(A)). This calculation indicates that similar one electron excited configuration is involved in the third leading term in the CASSCF(8,8) wavefunction. Thus, one electron excited configuration is not a result of low symmetry of open-lantern type structure: See Supporting Information pages S-18 to S-21 for details.

3.3 Geometry and Electronic Structure of the Molybdenum Analogue, $[Mo(R^1NC(R^2)NR^3)_2]_2$ ($R^1 = R^2 = R^3 = H$) (Mo1)

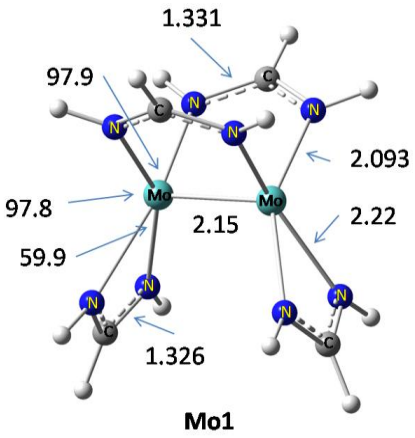

Figure 1-4. DFT-optimized geometry of $[Mo(R^1NC(R^2)NR^3)_2]_2$ ($R^1 = R^2 = R^3$ = H) (**Mo1**) at R(Mo-Mo) = 2.15 Å. Length in Å and angle in degree.

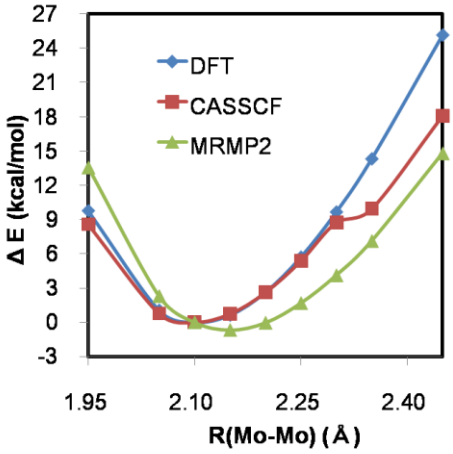

Figure 1-5. PESs of $[Mo(R^1NC(R^2)NR^3)_2]_2$ ($R^1 = R^2 = R^3$ = H) (**M2)** calculated by the DFT, CASSCF, and MRMP2 methods. The energy of R(Mo-Mo) = 2.10Å is taken to be standard (energy zero); E_{DFT} = -734.39894 a.u., E_{CASSCF} = -729.46970 a.u., and E_{MRMP2} = -732.53151 a.u. at this distance.

Though the Mo analogue of **R1** has not been synthesized yet, we investigated the Mo analogue of **M1**, $[Mo(R^1NC(R^2)NR^3)_2]_2$ ($R^1 = R^2 = R^3$ = H) (**Mo1**), to shed clear light on characteristic features of the dinuclear Cr(II) complex by making comparison between **M1** and **Mo1**. We optimized the geometry of **Mo1** with the DFT(B3LYP) method under C_{2v} symmetry, as shown in Figure 1-4. No imaginary frequency was observed at each optimized geometry. The DFT-calculated energy minimum is found at R(Mo-Mo) = 2.106 Å, as shown in Figure 1-5. CASSCF(8,8) and MRMP2 calculations present the energy minimum at R(Mo-Mo) = 2.101 Å and 2.151 Å, respectively. It is noted that all these methods present almost the same equilibrium Mo-Mo distance. This result is completely different from that of the dinuclear Cr(II) complex, indicating that very large difference in electronic structure exists between dinuclear Cr(II) and Mo(II) complexes.

The occupation numbers of important natural orbitals calculated by the CASSCF(8,8) method are shown in Table 1-1. Apparently, the occupation numbers of bonding orbitals are considerably larger than those of anti-bonding orbitals. The bond order at R(Mo-Mo) = 2.150 Å is evaluated to be 3.41, which is much larger than that of **M1**; see Table 1-1. The σ_d bond order is close to 1.0. The π_d and δ_d bond orders are 1.764 and 0.572, respectively,

which are much larger than those of **M1**. From these results, it should be concluded that all the σ_d, π_d, and δ_d-bonding interactions are much stronger in **Mo1** than in **M1**.

The CASSCF(8,8) wave function of **Mo1**, $\Psi_{\mathbf{Mo1},\,\mathrm{CAS(8,8)}}$, is represented as follows:

$$\begin{aligned}\psi_{\mathbf{Mo1},\mathrm{CAS(8,8)}} = {} & 0.867\Phi_{\mathrm{main}} - 0.259\Phi_{\delta^2\rightarrow\delta^{*2}} - 0.137\Phi_{\pi 2^2\delta^2\rightarrow\pi 2\delta\delta^*\pi 1^*} \\ & - 0.133\Phi_{\pi 1^2\delta^2\rightarrow\pi 1\delta\delta^*\pi 2^*} - 0.118\Phi_{\pi 2^2\rightarrow\pi 2^{*2}} + \cdots\end{aligned} \tag{3}$$

The main configuration is $\sigma_d^2\,\pi 1_d^2\,\pi 2_d^2\,\delta_d^2$. Though this is the same as that of **M1**, its expansion coefficient is much larger than that of **M1**. The second leading configuration is $\sigma_d^2\,\pi 1_d^2\,\pi 2_d^2\,\delta_d^{*2}$. Though this configuration is the same as that of **M1**, its expansion coefficient is much smaller than that of **M1**. The other configurations with large expansion coefficients are listed in Table 1-2. Apparently, the numbers of electron configurations are less in **Mo1** than in **M1.** All these results clearly show that the non-dynamical correlation is much smaller in **Mo1** than in **M1**, as expected above.

3.4 The Reason Why Non-dynamical Correlation is Much Larger in the Dinuclear Cr(II) Complex than in the Dinuclear Mo(II) Complex.

In many cases, the Cr-Cr distance was discussed on the basis of the Cotton's formal shortness ratio (*FSR*).[12b] *FSR* for A-B bond is defined by eq. 4,

$$FSR_{AB} \equiv \frac{R_{A-B}}{R_A + R_B}, \tag{4}$$

where $R_{\text{A-B}}$ is the A-B bond length in a molecule and R_{A} and R_{B} are the atomic radii of A and B, respectively. Many dinuclear Cr complexes have been reported to exhibit *FSR* value either similar to or smaller than that of dinitrogen molecule ($FSR_{\text{N-N}} = 0.783$);[12b] for instance, $FSR_{\text{Cr-Cr}}$ for **R1** is 0.780 at R(Cr-Cr) = 1.850 Å and 0.826 at R(Cr-Cr) = 1.96 Å which is the experimental value. These results suggest that the Cr-Cr bond of **R1** is similar to the very strong N-N triple bond. Actually, the M-M bond shorter than 2.0 Å is found in many dinuclear Cr and several dinuclear V comlexes[12b, 39] but not at all in the other transition metal complexes.[12b] Based on these facts, the Cr-Cr distance of 1.96 Å was discussed to be "short".[12b] However, the non-dynamical correlation is very large in the dinuclear Cr(II) complex. This is against our expectation that the non-dynamical correlation tends to be small when the bond distance is short. This unexpected result suggests that the *FSR* is not

TABLE 1-3: The <r>[a] and R_{Smax}[b] values of valence orbitals of Si, Cr, and Mo

	Si 3p[c]	Cr 3d[c]	Mo 4d[d]
<r> (Å)	1.4719	0.7333	0.9785
2×<r> (Å)	2.9438	1.4666	1.9571
R_{smax} (Å)			
σ–σ	2.4529	1.5200	2.5144
π–π	-	1.1473	1.4697

[a] Mean value of radial distribution function
[b] The distance between two atoms which provides the maximum overlap integral.
[c] Calculated with ANO basis proposed by Roos *et al.*[42]
[d] Calculated with Huzinaga's basis[43]

useful to discuss the Cr-Cr distance of this complex. Actually, it is likely that the *FSR* calculated with the atomic radius of neutral Cr(0) leads to unusually small *FSR* value because the atomic radius of Cr(0) is determined by the 4s orbital but the valence orbital of Cr(II) is 3d; note that the Cr(0) 4s orbital is much larger than the Cr(II) 3d orbital.

Because the bond distance depends on the orbital expansion, the bond distance must be discussed on the basis of orbital overlap. Here, we evaluated the mean radii, <*r*> of the radial distribution function of valence orbital and the distance, $R_{S\max}$, providing the maximum overlap integral. It is likely that the bond distance directly depends on the 2×<r> and $R_{S\max}$ values. In Cr atom, 2×$<r_{3d}>$, $R_{S\max}^{3d_\sigma}$, and $R_{S\max}^{3d_\pi}$ values are calculated to be 1.466 Å, 1.520 Å, and 1.147 Å, respectively,[42] as shown in Table 1-3 and Figure A1-11. The Cr-Cr distance (1.960 Å) of this open lantern-type dinuclear complex[28] is much longer than these values. On the other hand, the Mo-Mo distance (2.15 Å) of **Mo1** is moderately longer than 2×$<r_{4d}>$ and $R_{S\max}^{4d_\pi}$ values but much shorter than $R_{S\max}^{4d_\sigma}$ value, as shown in Table 1-3. These results indicate that the Cr-Cr quadruple bond of 1.960 Å is "long" but the Mo-Mo quadruple bond of 2.151 Å is either "medium" or "short". This understanding is consistent with the fact that the non-dynamical correlation is very large in the dinuclear Cr(II) complex but moderate in the Mo analogue.

From the above results, it should be concluded that the 2×<*r*> and $R_{S\max}$ values of valence d orbital must be employed to discuss whether the M-M bond is short or long. We wish to propose orbital shortness ratio (*OSR*) to discuss the M-M bond distance, as follows;

$$OSR = \frac{R_{M-M}}{R_{S\max}^{\sigma}} \qquad (5)$$

TABLE 1-4: The d-d and p-p overlap integrals[a] of Cr-Cr, Mo-Mo, and Si-Si pairs.

	M = Cr[a] (R = 1.85 Å)	M = Mo[b] (R = 2.15 Å)	M = Si[a] (R = 2.10 Å)
d_σ-d_σ (or p_σ-p_σ)	0.0764	0.1061	0.3143
d_π-d_π (or p_π-p_π)	0.1295	0.2036	0.3282
d_δ-d_δ	0.0672	0.0692	-

[a] Calculated with ANO basis proposed by Roos *et al*.[42]
[b] Calculated with Huzinaga's basis.[43]

where $R^{\sigma}_{S\max}$ is employed because the σ-bonding interaction is always more important than the π-bonding interaction and also the π-bonding interaction is not always involved in dinuclear complexes. The *OSR* value is 1.217 for this open-lantern type dinuclear Cr(II) complex and 0.854 for the Mo(II) analogue, indicating that the Cr-Cr distance should be understood to be long but the Mo-Mo distance is to be short. This *OSR* value also shows that the N-N distance of dinitrogen molecule is short; see $OSR_{N\text{-}N}$ = 0.752. Note that this *OSR* value is similar to the *FSR* value in dinitrogen molecule.

The long separation between two Cr atoms leads to small overlap integral. Actually, the overlap integral for the Cr-Cr pair is much smaller than that for the Mo-Mo pair: The overlap integral is calculated to be 0.0764, 0.130, and 0.0672 for d_σ–d_σ, d_π–d_π, and d_δ–d_δ pairs, respectively, at R = 1.85 Å in the Cr complex and 0.106, 0.204, and 0.0692 at R = 2.15 Å in the Mo complex, as shown in Table 1-4.

It should be noted that the Cr-Cr distance providing the maximum overlap integral of the d_σ orbital is very short (1.52 Å) but the Mo-Mo distance is long (2.51 Å). The overlap integral of d_σ orbital is 0.0810 for the Cr-Cr pair at R = 1.52 Å and 0.117 for the Mo-Mo pair at R = 2.51 Å. These results clearly show that the d orbital of Cr is intrinsically much smaller than that of Mo, as was discussed previouly.[45] It is very difficult for the Cr-Cr pair to approach each other at the Cr-Cr distance of 1.52 Å; note that this distance is similar to the C-C single bond. Therefore, the Cr-Cr bond must stay at much longer distance than the $R^{3d_\sigma}_{S\max}$ value, leading to the very small overlap integral in the Cr-Cr pair than in the Mo-Mo pair. As a result, the non-dynamical correlation is much larger in the dinuclear Cr(II) complex than in the dinuclear Mo(II) complex.

3.5. Comparison between d_σ-d_σ and d_π-d_π Molecular Orbitals

It should be noted that the d_σ-d_σ overlap integral is much smaller than the d_π-d_π overlap integral in both Cr-Cr and Mo-Mo pairs, as presented in Table 1-4. This is against our expectation that the overlap integral of the σ type orbital is much larger than that of the π type orbital. This unexpected result has not been reported yet, to our knowledge. However, this is not surprising because the d_π-d_π overlap presents two overlap regions, as shown in Scheme 1-4. Despite of the much larger overlap integral of the d_π-d_π pair, the occupation numbers of the $\pi 1_d$ and $\pi 2_d$ natural orbitals are moderately smaller than that of the σ_d orbital in both Cr and Mo dinuclear complexes, as shown in Table 1-1. It is worthy investigating the reason why the occupation number of the σ_d orbital is moderately larger than those of the $\pi 1_d$ and $\pi 2_d$ orbitals in spite of the much smaller d_σ-d_σ overlap than the d_π-d_π overlap in **R1** and **M1**.[41]

The d_π atomic orbital expands perpendicular to the Cr-Cr axis, as shown in Scheme 1-4. Because the C-N bonds of the ligand exist near the d_π-d_π overlap region, the exchange repulsion is induced between the $\pi 1_d$ and $\pi 2_d$ orbitals and doubly occupied orbitals of the C-N bonds, to push up the $\pi 1_d$ and $\pi 2_d$ orbital energies, which further leads to decrease of the occupation numbers of these orbitals. On the other hand, the σ_d orbital expands along the Cr-Cr axis and little suffers from such exchange repulsion (Scheme 1-4). Thus, the occupation number of the σ_d orbital becomes larger but those of the $\pi 1_d$ and $\pi 2_d$ orbitals become smaller than those expected from overlap integral.

Another reason is that the $\pi 1_d$ and $\pi 2_d$ orbitals induce larger electrostatic repulsion with the negatively charged N atoms than does the σ_d orbital. This is because the $\pi 1_d$ and $\pi 2_d$ orbitals are closer to the N atoms than the σ_d orbital. As a result, the $\pi 1_d$ and $\pi 2_d$ orbital energies become higher and their occupation numbers become smaller than those expected from the overlap integral. This Coulombic repulsion also leads to the participation

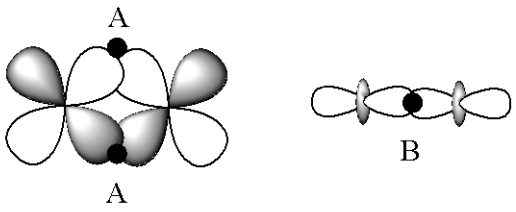

Scheme 1-4. Electron accumulation regions in d_π-d_π bonding orbital (π_d) and d_σ-d_σ bonding orbital (σ_d)

of the σ_d* orbital in the third and fourth leading terms of the CASSCF wavefunction. Because the $\pi 1_d$* and $\pi 2_d$* orbitals are also more destabilized by the Coulombic repulsion with the negatively charged N atom than the σ_d* orbital, electron occupations of the $\pi 1_d$* and $\pi 2_d$* orbitals lead to larger destabilization energy but that of the σ_d* orbital leads to smaller destabilization energy than those expected from overlap integral. This is one of the reasons why not the $\pi 1_d$* orbital but the σ_d* orbital participates in the third and fourth excited configurations of **R1**; see eq. 1 and above discussion.

Also, the nuclear-electron Coulombic attraction participates in the larger occupation number of the σ_d orbital than expected from overlap integral, as follows: Electron accumulation mainly occurs around the region A in the $\pi 1_d$ and $\pi 2_d$ orbitals and the region B in the σ_d orbital; see Scheme 1-4 for regions A and B. Because the region B is closer to the Cr atoms than the region A, the electron density in the region B yields larger nuclear-electron stabilization energy than that in the region A. Thus, the occupation number of the σ_d orbital becomes larger and those of the $\pi 1_d$ and $\pi 2_d$ orbitals become smaller than expected from overlap integral.

All these are plausible factor for the smaller occupation numbers of the $\pi 1_d$ and $\pi 2_d$ orbitals and the larger one of the σ_d orbital than expected from overlap integral.

3.6 Comparison between M-M and Si-Si Multiple Bonds

Comparison of the multiple bonds between transition metal and non-transition metal compounds is expected to present clear insight into their bonding natures. We investigated here Si_2H_2, **S1**, and Si_2H_4, **S2**. The σ_p and π_p bond orders of **S1** were evaluated with the CASSCF method to be 0.981 and 1.674 (0.837 per one π_p orbital, in average), respectively, and those of **S2** were evaluated to be 0.980 and 0.857, as shown in Table 1-5. It is noted that the occupation number of the σ_p orbital is considerably larger than that of the π_p orbital. This feature is different from that of the Cr-Cr and Mo-Mo multiple bonds.

In Si atom, $2\times\langle r_{3p}\rangle$, $R_{S\,\max}^{3p_\sigma}$, and $R_{S\,\max}^{3p_\pi}$ values were calculated to be 2.944 Å, 2.318 Å, and 2.453 Å, respectively, as shown in Table 1-3 and Figure A1-10. In the usual Si-Si double and triple bonds, the Si-Si distance is 2.0 Å to 2.3 Å,[44] which is much shorter

than $2\times\langle r_{3p}\rangle$, $R_{S\max}^{3p_\sigma}$, and $R_{S\max}^{3p_\pi}$ values. As a result, the *OSR* is small; the *OSR* value is 0.938 and 0.815 for the Si-Si double and triple bonds, respectively. Thus, the usual Si-Si double and triple bonds are defined to be "short", which leads to large overlap integral between two Si atoms. Actually, the overlap integrals of the p_σ-p_σ and p_π-p_π orbital pairs in the Si-Si multiple bond are much larger than those of d_σ-d_σ and d_π-d_π orbital pairs in the M-M multiple bond, as shown in Table 1-4. Thus, the non-dynamical correlation is small in **S1** and **S2**, as clearly shown by the considerably large bond order.

It is noted here that the p_σ-p_σ overlap integral is moderately smaller than the p_π-p_π one, unexpectedly. However, the σ_p bond order is much larger than the π_p bond order in both **S1** and **S2**, unlike those of **M1** and **R1**. In these molecules, no group is present to destabilize the π_p orbital energy, like the C-N bonds and negatively charged N atoms in **M1** and **R1**. Here, different factors are responsible to the larger occupation number of the σ_p orbital than expected from the overlap integral. One plausible factor is nuclear-electron attraction like **M1** and **R1**. Another factor is the bonding participation of Si 3s orbital in the σ_p orbital, which lowers the energy level of the σ_p orbital through the bonding mixing, as shown in Scheme 1-3. On the other hand, the Si 3s orbital does not participate at all in the out-of-plane π_p bonding orbital. In the in-plane π_p orbital, the Si 3s orbitals participate in an

TABLE 1-5: The occupation numbers of the natural orbitals and the bond orders of **S1** (Si_2H_2) and **S2** (Si_2H_4)

	S1[a]	**S2**[b]
σ_p	1.981	1.980
$\pi 1_p$[c]	1.880	1.867
$\pi 2_p$[d]	1.794	-
$\pi 2_p$*[d]	0.202	-
$\pi 1_p$*[c]	0.124	0.133
σ_p*	0.020	0.021
Bond Order		
σ_p	0.981	0.980
π_p	1.674	0.867
Total	2.655	1.847

[a] The CASSCF(6,6) method was employed.
[b] The CASSCF(4,4) method was employed.
[c] Out-of plane π orbital
[d] In-plane π orbital

anti-bonding manner, as shown in Scheme 1-3, which pushes up the in-plane π_p orbital energy. In **M1** and **R1**, the 4s orbital of Cr little contributes to the σ_d orbital because the Cr 4s orbital is at much higher energy than Cr 3d orbital in Cr(II). Moreover, the difference between p_σ-p_σ overlap integral and p_π-p_π one in the Si-Si pair is much smaller than that between d_σ-d_σ overlap integral and d_π-d_π one in the Cr-Cr pair, as shown in Table 1-4. Therefore, despite of the absence of the C-N bonds and the negatively charged N atom, the participation of Si 3s orbital and the nuclear-electron attraction are enough to overcome the consequence of the smaller p_σ-p_σ overlap integral, leading to the larger occupation number of the σ_p orbital than that of the π_p orbital.

In conclusion, the interesting differences between M-M and Si-Si multiple bonds are summarized, as follows: (1) The non-dynamical correlation is much smaller in the Si-Si multiple bond than in the Cr(II)-Cr(II) multiple bond. And, (2) the σ-bonding interaction much more contributes to the Si-Si multiple bond than that to M-M multiple bond.

4. Conclusion

We investigated open-lantern type dinuclear Cr(II) complex, $[Cr(R^1NC(R^2)NR^3)_2]_2$ (R^1 = Et, R^2 = Me, and R^3 = ^{t}Bu) with DFT, CASSCF, and MRMP2 methods. The DFT-calculated potential energy decreases as the Cr-Cr distance becomes shorter and the equilibrium structure is not found in the range R(Cr-Cr) > 1.75 Å. In contrast to the DFT-calculated result, the CASSCF(8,8)-calculated potential energy decreases as the Cr-Cr distance becomes longer but does not present the minimum in the range R(Cr-Cr) < 2.05 Å. The MRMP2 calculation exhibits the minimum at R(Cr-Cr) = 1.851 Å, as shown in Figures 1-2 and 1-3. These results suggest that both non-dynamical and dynamical correlations are considerably large in this complex. On the other hand, the non-dynamical correlation is small in the Mo analogue; actually, the DFT, CASSCF, and MRMP2 methods present almost the same equilibrium Mo-Mo distance. The reason why the non-dynamical correlation in the dinuclear Mo complex is smaller than in the dinuclear Cr complex is explained in terms of the overlap integral: actually the overlap integral of valence d orbitals in the Cr-Cr pair is much smaller than that of Mo-Mo pair. We wonder why the non-dynamical correlation is very large though the Cr-Cr bond was experimentally discussed to be short in many dinuclear Cr complexes. To

find answer to this issue, we wish to propose *OSR* (orbital shortness ratio) here to discuss the M-M multiple bond distance. The *OSR* value is 1.217 for real Cr complex **R1** and 0.854 for **Mo1**. Thus, we must understand that the Cr-Cr distance of 1.96 Å is long in **R1** but the Mo-Mo distance of 2.151 Å is short in **Mo1**. These understandings are consistent with the fact that the non-dynamical correlation is much larger in the dinuclear Cr(II) complex than in the Mo(II) analogue.

The bond order of the real complex **R1** is evaluated to be 2.40, which is much smaller than the formal bond order of 4. That of the Mo analogue is evaluated to be 3.41, which is much larger than that of **R1**. These results agree with the fact that the non-dynamical correlation is larger in the dinuclear Cr complex than in the Mo analogue.

Our calculations reveal that the overlap integral of valence d_π orbital is much larger than that of d_σ orbital in both Cr and Mo dinuclear complexes, and that of p_π orbital is moderately larger than that of p_σ orbital in Si_2H_2 and Si_2H_4. However, the occupation number of the σ_d orbital is moderately larger than those of the π_d orbitals in both the dinuclear Cr and Mo complex, and that of the σ_p orbital is much larger than that of the π_p orbital in both Si-Si double and triple bonds, against the expectation from overlap integrals. In the Si-Si multiple bond, the Si 3s orbital contributes to the σ_p orbital, leading to the lower orbital energy and the larger occupation number of the σ_p orbital than expected from overlap integral. In the M-M multiple bond, the moderately larger occupation number of the σ_d orbital arises from the smaller exchange repulsion between the σ_d and bridging ligand, the smaller Coulombic repulsion between the σ_d and the negatively charged N atoms of ligands, and the larger nuclear-electron attraction between the electron density of the σ_d and the M atoms than those of the π_d. Important differences between Cr-Cr and Si-Si multiple bonds are summarized, as follows: (1) The non-dynamical correlation is much larger in the Cr-Cr multiple bond than in the Si-Si multiple bond, and (2) the σ-bonding interaction is much more important than does the π-boning interaction in the Si-Si multiple bond, while the σ-bonding interaction is moderately more important than the π-bonding interaction in the Cr-Cr multiple bond.

References and Notes

(1) Cotton, F. A.; Harris, C. B. *Inorg. Chem.* **1965**, *4*, 330.

(2) Cotton, F. A. *Inorg. Chem.* **1965**, *4*, 334.

(3) (a) Roos, B. O. *Adv. Chem. Phys.* **1987**, 399. (b) Andersson, K; Malmqvist, P. A.; Roos, B. O.; Sadlej, A. J.; Wolinski, K. *J. Phys. Chem.* **1990**, *94*, 5483.

(4) (a) Hirao, K. *Chem. Phys. Lett.* **1992**, *190*, 374. (b) Hirao, K. *Chem. Phys. Lett.* **1992**, *196*, 397. (c) Nakano, H. *J. Chem. Phys.* **1993,** *99*, 7983.

(5) Goodgame, M. M.; Goddard, III W. A. *J. Phys. Chem.* **1981**, *85*, 215.

(6) (a) Werner, H.-J.; Knowles, P. J. *J. Chem. Phys.* **1988**, *89*, 5803. (b) Andersson, K.; Roos, B. O.; Malmqvist, P.-A.; Widmark, P.-O.; *Chem. Phys. Lett.* **1994**, *230*, 391. (c) Roos, B. O.; Andersson, K.; *Chem. Phys. Lett.* **1995**, *245*, 215. (d) Edgecombe, K. E.; Becke, A. D. *Chem. Phys. Lett.* **1995**, *244*, 427. (e) Thomas, E. J.; Murray, J. S.; O'Connor, C. J.; Politzer, P. *J. Mol. Struct.* (*Theochem*) **1999**, *487*, 177. (f) Barden, C. J.; Rienstra-Kiracofe, J. C.; Schaefer, H. F. *J. Chem. Phys.* **2000**, *113*, 690. (g) Angell, C.; Cimiraglia, R.; Malrieu, J.-P. *J. Chem. Phys.* **2002**, *117*, 9138. (h) Celani, P.; Stoll, H.; Werner, H.-J.; Knowles P. *J. Mol. Phys.* **2004**, *102*, 2369. (i) Roos, B. O.; Borin, A. C.; Gagliardi, L. *Angew. Chem. Int. Ed.* **2007**, *46*, 1469.

(7) Nguyen, T.; Sutton, A. D.; Brynda, M.; Fettinger, J. C.; Long, G. J.; Power, P. P. *Science* **2005**, *310*, 844.

(8) Landis, C. R.; Weinhold, F. *J. Am. Chem. Soc.* **2006**, *128*, 7335

(9) Merino, G; Donald, K, J; D'Acchioli, J. S; Hoffmann, R. *J. Am. Chem. Soc.* **2007**, *129*, 15295.

(10) Brynda, M.; Gagliardi, L.; Widmark, P-O; Power, P. P.; Roos, B. O. *Angew. Chem. Int. Ed*. **2006**, *45*, 3804.

(11) Hsu, C.-W.; Yu, K. J.-S.; Yen, C.-H.; Lee, G.-H.; Wang, Y.; Tsai, Y.-C. *Angew. Chem. Int. Ed*. **2008**, *47*, 9933.

(12) (a) Cotton, F. A.; Extine, M.; Rice, G. W. *Inorg. Chem*. **1978** *17*, 176. (b) Cotton, F. A.; Murillo, C. A.; Walton, R. A. *Multiple Bond between Metal Atoms*, Springer, Berlin, 3rd ed., **2005**.

(13) (a) Mashima, K.; Tanaka, M.; Tani, K.; Nakamura, A.; Takeda, S.; Mori, W.; Yamaguchi,

K. *J. Am. Chem. Soc.* **1997**, *119*, 4307. (b) Nishino, M.; Yamanaka, S.; Yoshioka, Y.; Yamaguchi, K. *J. Phys. Chem. A.* **1997**, *101*, 705. (c) Nishino, M; Yoshioka, Y; Yamaguchi, K; Mashima, K.; Tani, K; Nakamura, A. *Bull. Chem. Soc. Jpn.* 1**998**, *71*, 99.

(14) de Mello, P. C.; Edwards, W. D.; Zerner, M. C. *J. Am. Chem. Soc.* **1982**, *104*, 1440.

(15) (a) Hao, S.; Gambarotta S.; Bensimon, C. *J. Am. Chem. Soc.* **1992** *114*, 3556. (b) Edema, J. J. H.; Gambarotta, S.; Bolhuis, F. V.; Spek, A. L. *J. Am. Chem. Soc.* **1989**, *111*, 2142. (c) Edema, J. J. H.; Gambarotta, S.; Meetsma, A.; Bolhuis, F. V.; Spek, A. L.; Smeets, W. J. J. *Inorg. Chem.* **1990**, *29*, 2147. (d) Hao, S.; Song, J.-I.; Berno, P.; Gambarotta, S. *Organometallics*, **1994**, *13*, 1326. (e) Edema, J. J. H.; Gambarotta, S.; van der Sluis, P.; Smeets, W. J. J.; Spec, A. L. *Inorg. Chem*. **1989**, *28*, 3782. (f) Hao, S.; Gambarotta, S.; Bensimon, C.; Edema, J. J. H. *Inorg. Chim. Acta.* **1993**, *213*, 65.

(16) Li, S.; King, R. B.; Schaefer, H. F., III *J. Phys. Chem. A.* **2004**, *108*, 6879.

(17) Becke, F.; Wiegeleben, P.; Ruffer, T.; Wagner, C.; Boese, R.; Blaser, D.; Steinborn, D. *Organometallics* **1998**, *17*, 475.

(18) Losada, J.; Alvarez, S.; Novoa, J. J.; Mota, F.; Hoffmann, R.; Silvestre, J. *J. Am. Chem. Soc*. **1990**, *112*, 8998.

(19) Brauer, D. J.; Krueger, C. *Inorg. Chem.* **1976**, *15*, 2511.

(20) Ziegler, T. *J. Am. Chem. Soc.* **1985**, *107*, 4453.

(21) (a) Mitschler, A.; Rees, B.; Wiest, R.; Benard, M. *J. Am. Chem. Soc.* **1982**, *104*, 7501. (b) Benard, M. *J. Am. Chem. Soc.* **1978**, *100*, 2354.

(22) Manning, M. C.; Trogler, W. C. *J. Am. Chem. Soc.* **1983**, *105*, 5311.

(23) Lichtenberger, D. L.; Lynn, M. A.; Chisholm, M. H. *J. Am. Chem. Soc.* **1999**, *121*, 12167.

(24) El-Kadri, O. M.; Heeg, M. J.; Winter, C. H. *Inorg. Chem.* **2006**, *45*, 5278.

(25) Chang, H. C.; Li, J. T.; Wang, C. C.; Lin, T. W.; Lee, H. C.; Lee, G. H.; Peng, S. M. *Eur. J. Inorg. Chem.* **1999**, *8*, 1243.

(26) Morse, P. M.; Spencer, M. D.; Wilson, S. R.; Girolami, G. S. *Organometallics* **1994,** *13*, 1646.

(27) Garner, C. D.; Senior, R. G.; King, T. J. *J. Am. Chem. Soc.* **1976**, *98*, 3526.

(28) Sadique, A. R.; Heeg, M. J.; Winter, C. H.; *J. Am. Chem. Soc.* **2003**, *125*, 7774.

(29) (a) Becke, A. D. *J. Chem. Phys.* **1993**, 98, 5648. (b) Lee, C.; Yang, W.; Parr, R. G. *Phys.*

Rev. B **1988**, *37*, 785.

(30) Saito, K.; Nakao, Y.; Sato, H.; Sakaki, S. *J. Phys. Chem. A* **2006**, *110*, 9710.

(31) Blaudeau, J.-P.; Ross, R. B.; Pitzer, R. M. *J. Phys. Chem.* **1994**, *98*, 7123.

(32) Dapprich, S.; Komaromi, I.; Byun, K. S.; Morokuma, K.; Frisch, M. J. *J. Mol. Struct. (Theochem)* **1999**, *461*, 1.

(33) (a) Bergner, A.; Dolg, M.; Kuechle, W.; Stoll, H.; Preuss, H. *Mol. Phys.* **1993**, *80*, 1431.

(b) M. Dolg, U. Wedig, H. Stoll, and H. Preuss *J. Phys. Chem.* **1987**, *86*, 866.

(34) Sekiguchi, A.; Kinjo, R.; Ichinohe, M.; *Science*, **2004**, *305*, 1755.

(35) Gaussian 03, Revision C.02, M. J. Frisch, G. W. Trucks, H. B. Schlegel, G. E. Scuseria, M. A. Robb, J. R. Cheeseman, J. A. Montgomery, Jr., T. Vreven, K. N. Kudin, J. C. Burant, J. M. Millam, S. S. Iyengar, J. Tomasi, V. Barone, B. Mennucci, M. Cossi, G. Scalmani, N. Rega, G. A. Petersson, H. Nakatsuji, M. Hada, M. Ehara, K. Toyota, R. Fukuda, J. Hasegawa, M. Ishida, T. Nakajima, Y. Honda, O. Kitao, H. Nakai, M. Klene, X. Li, J. E. Knox, H. P. Hratchian, J. B. Cross, V. Bakken, C. Adamo, J. Jaramillo, R. Gomperts, R. E. Stratmann, O. Yazyev, A. J. Austin, R. Cammi, C. Pomelli, J. W. Ochterski, P. Y. Ayala, K. Morokuma, G. A. Voth, P. Salvador, J. J. Dannenberg, V. G. Zakrzewski, S. Dapprich, A. D. Daniels, M. C. Strain, O. Farkas, D. K. Malick, A. D. Rabuck, K. Raghavachari, J. B. Foresman, J. V. Ortiz, Q. Cui, A. G. Baboul, S. Clifford, J. Cioslowski, B. B. Stefanov, G. Liu, A. Liashenko, P. Piskorz, I. Komaromi, R. L. Martin, D. J. Fox, T. Keith, M. A. Al-Laham, C. Y. Peng, A. Nanayakkara, M. Challacombe, P. M. W. Gill, B. Johnson, W. Chen, M. W. Wong, C. Gonzalez, and J. A. Pople, Gaussian, Inc., Wallingford CT, **2004**..

(36) M.W.Schmidt, K.K.Baldridge, J.A.Boatz, S.T.Elbert, M.S.Gordon, J.H.Jensen, S.Koseki, N.Matsunaga, K.A.Nguyen, S.Su, T.L.Windus, M.Dupuis, J.A.Montgomery., J.COMPUT.CHEM. **1993**, *14*, 1347-1363.

(37) Swiss National Supercomputing Centre. See

http://www.bioinformatics.org/molekel/wiki/

(38) Fully optimized geometry of **M1** takes C_s symmetry with reflection mirror being on the C-Cr-Cr-C plane (Supporting Information Figure A1-3). This geometry is considerably different from that of real complex. We carried out preliminary examination with the geometry of **M1** shown in Figure 1-1, because the imaginary frequency is very small and moreover PESs of **M1** are essentially the same as those of **R1**.

(39) Cotton, F. A.; Hillard, E. A.; Murillo, C. A.; *J. Am. Chem. Soc.*, **2003**, *123*, 2026.

(40) Li, Q-s; Zhang, X.; Xie, Y.; King, R. B.; Schaefer, H. F. *J. Am. Chem. Soc.* **2007**, *129*, 3433.

(41) In CASSCF calculation, the orbital energy is not defined. The large occupation number corresponds, in general, to the low energy of the canonical orbital which is the main

contributor of the natural orbital.

(42) (a) Pou-Amerigo, R.; Merchan, M.; Nebot-Gil, I.; Widmark, P-O.; Roos, B. O. *Theor. Chim. Acta.* **1995**, *92*, 149. (b) Widmark, P-O.; B. Joakim, Persson; Roos, B. O. *Theor. Chim. Acta.* **1991**, *79*, 419.

(43) Huzinaga, S. *Gaussian basis sets for molecular calculations*, **1984**, Elsevier Science Publishing Company Inc., New York.

(44) Wang, Y.; Xie, Y.; Wei, P.; King, R. B. ; Schaefer, H. F.; Schleyer, P. v. R.; Robinson, G. H. *Science* **2008**, *321*, 1069.

(45) Frenking, G; Fröhlich, N. *Chem. Rev* **2000**, *100*, 717.

Appendix:

Optimized geometries of **S1** and **S2** (Figure A1-1). Kohn-Sham orbitals of **S1** (Figure A1-2). Fully optimized geometries of **M1** (Figure A1-3). The PES of **M1** in the nonet spin state (Figure A1-4). The occupation numbers of **M1** (Figure A1-5), **R1** (Figure A1-6), and **Mo1** (Figure A1-7). PES of closed-lantern type complex (Figure A1-8) and its important CASSCF configuration and coefficients (Table A1-4). Overlap integrals between two valence orbitals of M atom, $S^{M}_{d_a - d_a}(R)$, as function of nuclear distance R where M = N (Figure A1-9), M = Si (Figure A1-10), M = Cr (Figure A1-11), and M = Mo (Figure A1-12).

Optimized geometries of disilicon compounds.

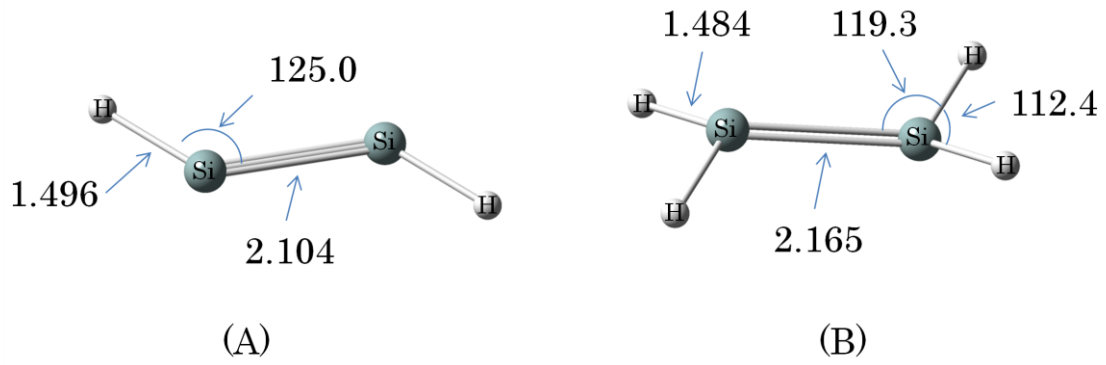

Figure A1-1. DFT-optimized geometries of HSi≡SiH (**S1**) (A) and $H_2Si{=}SiH_2$ (**S2**) (B). Length in Å and angle in degree.

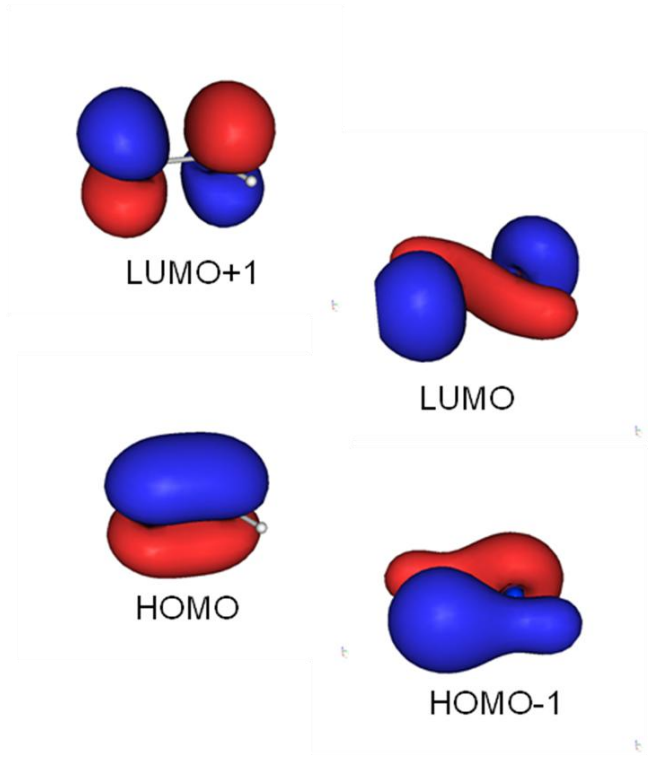

Figure A1-2. The Kohn-Sham orbitals of Si_2H_2 (**S1)** calculated by the DFT method with the B3LYP functional using cc-pVTZ basis functions.

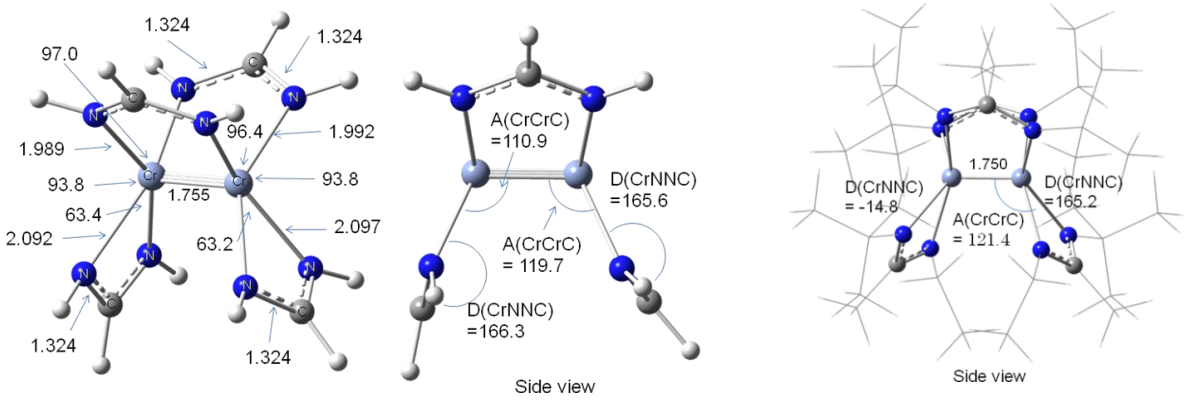

Figure A1-3. Fully optimized geometry of $[Cr(R^1NC(R^2)NR^3)_2]_2$ (R^1=H, R^2=H, R^3=H) (**M1**) in the singlet state calculated with the DFT(B3LYP) method. The optimized geometry takes Cs symmetry with reflection mirror being on the C-Cr-Cr-C plane. Length in Å and angle in degree.

It should be noted that the diheadral angle, D(CrNNC), is 165 and -14.8 º in **R1** but 165-166º in this fully optimized geometry of **M1**. In other words, **R1** has the C_2 axis perpendicular to the Cr-Cr bond at its midpoint, but its disappears in the fully optimized geometry of **M1**.

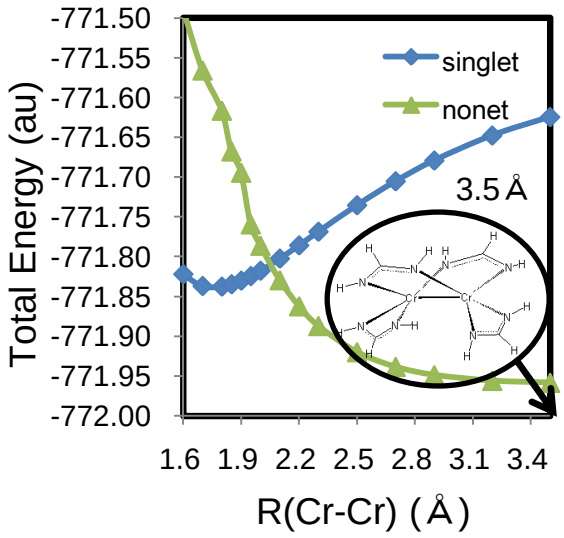

Figure A1-4. The PES of $[Cr(R^1NC(R^2)NR^3)_2]_2$ (R^1=H, R^2=H, R^3=H) (**M1**) in the singlet (blue) and nonet (green) spin states calculated with the DFT(B3LYP) method in C_{2v} symmetry.

The occupation numbers of $[Cr(R_1NC(R_2)NR_3)_2]_2$ (R_1=H, R_2=H, R_3=H) (M1), $[Cr(R_1NC(R_2)NR_3)_2]_2$ (R_1=Et, R_2=CH_3, R_3=^{t}Bu) (R1), and $[Mo(R_1NC(R_2)NR_3)_2]_2$ (R_1=H, R_2=H, R_3=H) (Mo1) calculated by the CASSCF(8,8) method with SDD basis

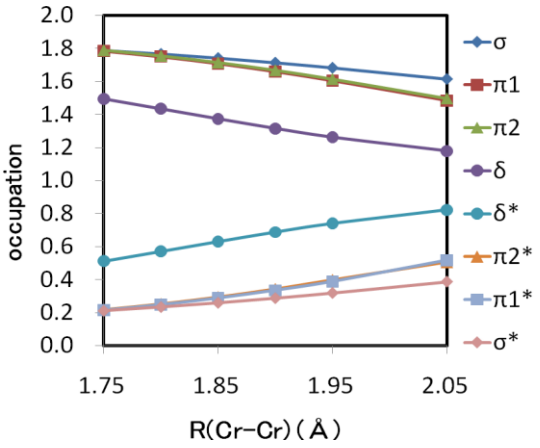

Figure A1-5. The occupation number of $[Cr(R_1NC(R_2)NR_3)_2]_2$ (R_1=H, R_2=H, R_3=H) (**M1**)

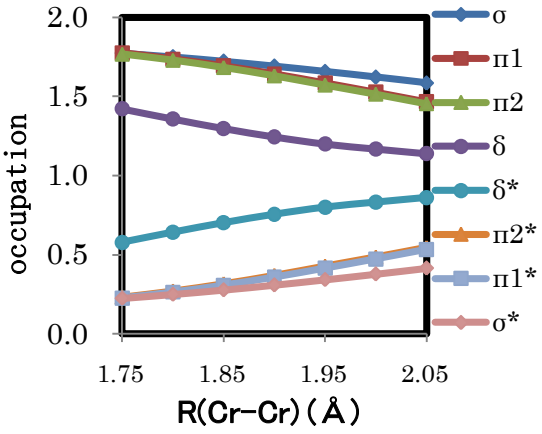

Figure A1-6. The occupation number of $[Cr(R_1NC(R_2)NR_3)_2]_2$ (R_1=Et, R_2=Me, R_3=^{t}Bu) (**R1**)

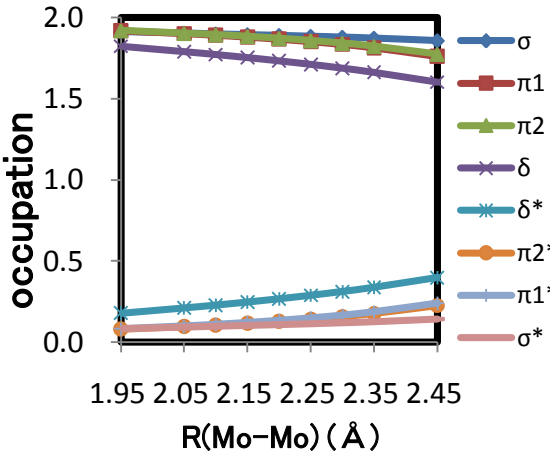

Figure A1-7. The occupation number of $[Mo(R_1NC(R_2)NR_3)_2]_2$ (R_1=H, R_2=H, R_3=H) (**Mo1**)

Comparison of open-lantern type complex with closed-lantern type complex

As mentioned in section 3.2 of the main text, one-electron excited configurations have somewhat large coefficients in the CASSCF(8,8) wave function of **R1**. One may suspect that this is induced by the mixing of metal d_δ, d_π and d_σ orbitals because **R1** takes low symmetry (C_2) and that it is not any more the case for the open-lantern complexes. To examine this issue, we investigated closed-lantern type complex (Scheme 1 (A)), $Cr_2(R^1NC(R^2)NR^3)_4$ ($R^1 = R^2 = R^3 = H$) (**M2**) with the DFT(B3LYP), CASSCF(8,8), and MRMP2 methds. This is because the σ_d, $\pi 1_d$, $\pi 2_d$, and δ_d orbitals and their anti-bonding orbitals never mix with each other due to different irreducible representation in D_{2h} symmetry geometry.

We optimized the geometry of **M2** in the same way as **M1**, where **M2** was restrected to take D_{2h} symmetry. The PESs calculated with the DFT(B3LYP), CASSCF(8,8), and MRMP2 methods are shown in Figure S8. The PESs of **M2** are similar to those of **M1** and **R1**: The DFT method underestimates the Cr-Cr distance, the CASSCF(8,8) method overestimates the Cr-Cr distance, and the MRMP2 method successfully presents energy minimum at R(Cr-Cr) = 1.851 Å.

The configurations with large expansion coefficients of the CASSCF(8,8) wave function of **M2** at R(Cr-Cr) = 1.85 Å are shown in Table S4. The main configuration of **M2** is $\sigma_d^2\pi 1_d^2\pi 2_d^2\delta_d^2$, and the second leading configuration is $\sigma_d^2\pi 1_d^2\pi 2_d^2\delta_d^{*2}$, which are the same as those of **R1**. The third and fourth leading configurations are degenerate, which are $\sigma_d^2\pi 1_d^2\pi 2_d^1\delta_d^1\delta_d^{*1}\pi 2_d^{*1}$ and $\sigma_d^2\pi 1_d^1\pi 2_d^2\delta_d^1\delta_d^{*1}\pi 1_d^{*1}$. The fourth configuration is the same as the fourth leading configuration in the CASSCF wave function of **R1**. The third configuration, on the other hand, has very tiny coefficient in **R1**. Instead, the $\sigma_d^2\pi 1_d^2\pi 2_d^1\delta_d^1\delta_d^{*1}\sigma_d^{*1}$ configuration is the third leading configuration in **R1**, as shown in Table 2 of the main text.

Thus, one-electron excited configurations are important in the CASSCF(8,8) wave function of closed-lantern type complex with high symmetry, indicating that the presence of those one-electron excited configurations is not the consequence of orbital mixing but is essential to these Cr dinuclear complexes. Though it is likely that the difference between the third leading configurations of **M2** and **R1** arise from the difference between closed-type and open-type lantern complexes, details are not clear, at this moment.

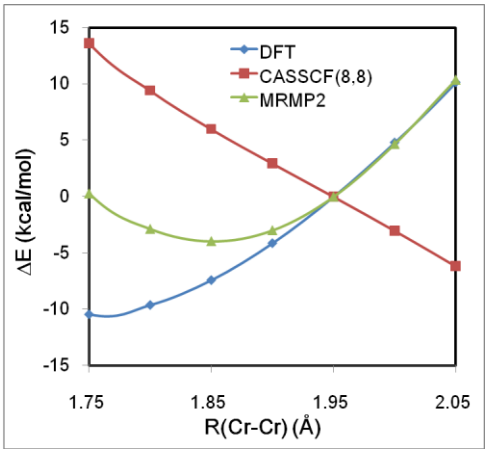

Figure A1-8. PESs of $Cr_2(R^1NC(R^2)NR^3)_4$ (R^1 = R^2 = R^3 = H) (**M2**) calculated by the DFT(B3LYP), CASSCF(8,8), and MRMP2 methods. The energy of R(Cr-Cr) = 1.95 Å is taken to be standard (energy zero); E_{DFT} = -771.86107 a.u., E_{CASSCF} = -766.93709 a.u., and E_{MRMP2} = -769.89658 a.u. at this distance.

TABLE A1-4: Important electron configurations and their coefficients of $Cr_2(R^1NC(R^2)NR^3)_4$ (R^1 = R^2 = R^3 = H) (**M2**) in D_{2h} symmetry[a]

M2	
coefficients	configuration
0.67204	$\sigma_d^2\pi 1_d^2\pi 2_d^2\delta_d^2$
-0.37410	$\sigma_d^2\pi 1_d^2\pi 2_d^2\delta_d^{*2}$
-0.20341	$\sigma_d^2\pi 1_d^2\pi 2_d^1\delta_d^1\delta_d^{*1}\pi 2_d^{*1}$
-0.20341	$\sigma_d^2\pi 1_d^1\pi 2_d^2\delta_d^1\delta_d^{*1}\pi 1_d^{*1}$
-0.17490	$\sigma_d^1\pi 1_d^2\pi 2_d^2\delta_d^1\delta_d^{*1}\sigma_d^{*1}$
-0.16200	$\sigma_d^2\pi 1_d^2\delta_d^2\pi 2_d^{*2}$
-0.16200	$\sigma_d^2\pi 2_d^2\delta_d^2\pi 1_d^{*2}$
-0.13238	$\pi 1_d^2\pi 2_d^2\delta_d^2\sigma_d^{*2}$
-0.12996	$\sigma_d^1\pi 1_d^2\pi 2_d^1\delta_d^2\pi 2_d^{*1}\sigma_d^{*1}$
-0.12996	$\sigma_d^1\pi 1_d^1\pi 2_d^2\delta_d^2\pi 1_d^{*1}\sigma_d^{*1}$
0.11359	$\sigma_d^2\pi 1_d^2\delta_d^2\pi 2_d^{*2}$
0.11359	$\sigma_d^2\pi 2_d^2\delta_d^2\pi 1_d^{*2}$
0.10234	$\sigma_d^2\pi 1_d^1\pi 2_d^1\delta_d^2\pi 2_d^{*1}\pi 1_d^{*1}$

[a] The CASSCF(8,8) method was employed.

Overlap integrals between two valence d_a orbitals of M atom, $S^{M}_{d_a-d_a}(R)$, as function of nuclear distance R.

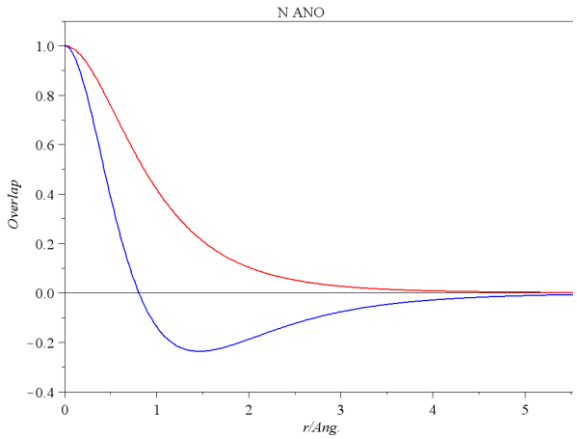

Figure A1-9. Overlap integrals between two valence p_σ (blue) and p_π (red) orbitals of N atom with Roos's ANO basis.[1]

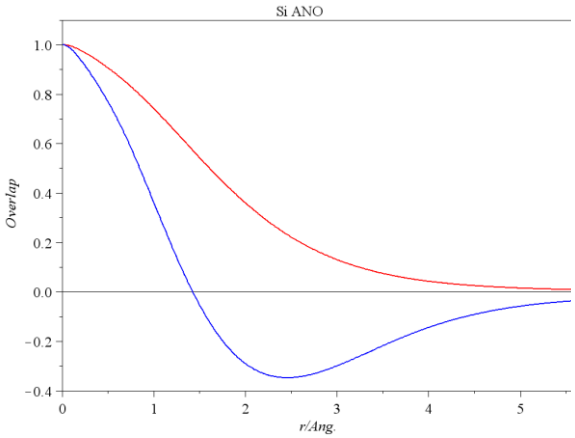

Figure A1-10. Overlap integrals between two valence p_σ (blue) and p_π (red) orbitals of Si atom with Roos's ANO basis.[1]

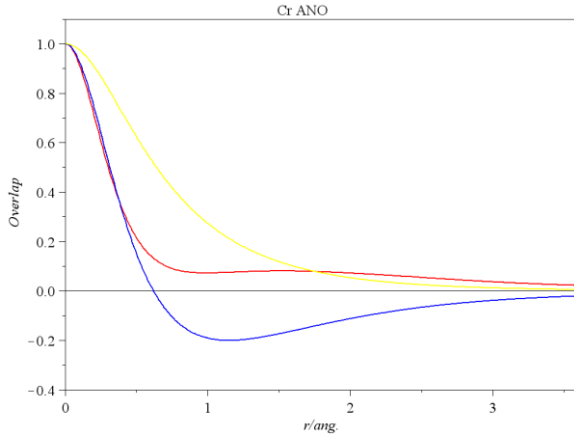

Figure A1-11. Overlap integrals between two valence d_σ (red), d_π (blue), and d_δ (yellow) orbitals of Cr atom with Roos's ANO basis.[1]

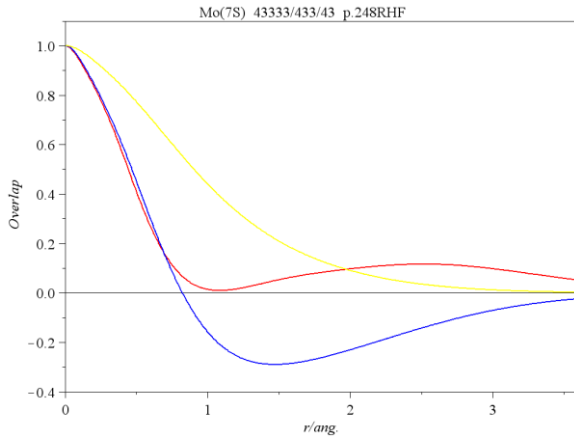

Figure A1-12. Overlap integrals between two valence d_σ (red), d_π (blue), and d_δ (yellow) orbitals of Mo atom with Huzinaga basis.[2]

Reference

(1) (a) Pou-Amerigo, R.; Merchan, M.; Nebot-Gil, I.; Widmark, P-O.; Roos, B. O. *Theor. Chim. Acta.*, **1995**, *92*, 149., (b) Widmark, P-O.; B. Joakim, Persson; Roos, B. O.; *Theor. Chim. Acta.*, **1991**, *79*, 419.

(2) Huzinaga, S. *Gaussian basis sets for molecular calculations*, **1984**, Elsevier Science Publishing Company Inc., New York.

Chapter 2
Inverted Sandwich Type Dinuclear Chromium(I) Complex and Its Analogues of Scandium(I), Titanium(I), Vanadium(I), Manganese(I), and Iron(I): Theoretical Study of Electronic Structure and Bonding Nature

1. Introduction:

Since the discovery of ferrocene, $Fe(C_5H_5)_2$, many kinds of sandwich type complexes (STCs) have been synthesized and studied experimentally and theoretically.[1,2] Kaminsky catalyst, in which Zr is sandwiched between two cyclopentadienyl (Cp) rings, is one of the most famous STCs,[3] because of its excellent polymerization catalysis.

Nowadays, various STCs, which consist of not only five-membered rings but also six-membered rings and more complicated rings with the first, second, and third row transition metals, are reported.[4] Swart theoretically studied STCs of the first-row transition metals (Sc-Zn) with two Cp rings and reported that these STCs could take singlet to quartet spin states by changing the metal center.[5] This result was explained in terms of the MO diagram:[5] Because of the presence of three quasi-degenerate e_2' and a_1' orbitals around HOMO and LUMO, the quartet spin state appears as the highest spin state when all of these MOs are singly occupied. The singlet spin state appears as the lowest spin state when all of them are either empty or doubly occupied.

According to this discussion, the highest spin multiplicity cannot exceed quartet even if we control the number of unpaired electrons by changing metal center and/or its oxidation state. Even if we change the Cp rings to six-membered rings, the highest spin multiplicity is expected to be quartet because the orbitals and their energies around HOMO and LUMO are similar to those of the STC of Cp. Actually, the electron configuration of ferrocene is similar to that of bis(benzene)chromium.

Recently, Tsai *et al.*[6] and Monillas *et al.*[7] synthesized inverted sandwich type complexes (ISTCs) of chromium, $(\mu\text{-}\eta^6\text{:}\eta^6\text{-}C_6H_5CH_3)[Cr(DDP)]_2$ $\mathbf{T_{Cr}}$ (DDPH = 2-{(2,6-diisopropyllhenyl)amino}-4-{(2,6-diisopropyllhenyl)imino}pent-2-ene, which is referred to "nacnac" in several works)[8] and $(\mu\text{-}\eta^6\text{:}\eta^6\text{-}C_6H_6)[Cr(DDP)]_2$ $\mathbf{B_{Cr}}$, respectively,

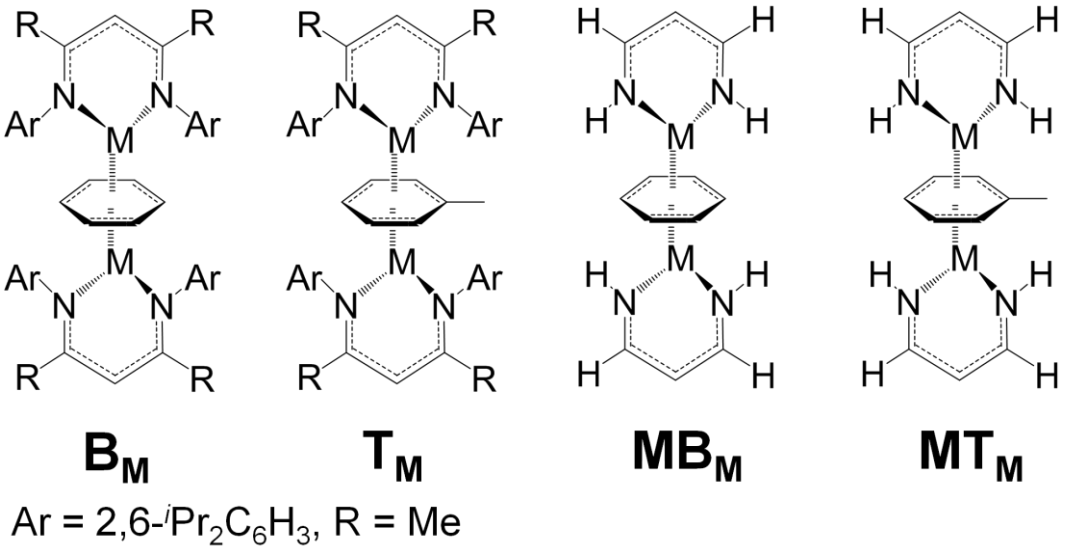

Scheme 2-1. (μ-η^6:η^6-C_6H_6)[M(DDP)]$_2$ (**B_M**), (μ-η^6:η^6-$C_6H_5CH_3$)[M(DDP)]$_2$ (**T_M**), (μ-η^6:η^6-C_6H_6)[M(AIP)]$_2$ (**MB_M**), and (μ-η^6:η^6-$C_6H_5CH_3$)[M(AIP)]$_2$ (**MT_M**) (M = Sc - Fe, DDPH = 2-{4-{(2,6-diisopropyllhenyl) imino} pent-2-ene, AIPH= (*Z*)-1-amino-3-imino-prop-1-ene)

where **T_{Cr}** and **B_{Cr}** represent ISTC of toluene with two Cr(DDP) moieties and that of benzene with two Cr(DDP) moieties, respectively; see Scheme 2-1. Interestingly, they take septet spin state. Also, Tsai *et al*. reported that ISTC of vanadium, (μ-η^6:η^6-$C_6H_5CH_3$)[V(DDP)]$_2$ (**T_V**) takes very high spin state of quintet.[9] These are surprisingly high spin state, considering that organometallic compounds tend to take in general low spin state; for example, ISTC of manganese, (μ-η^6:η^6-$C_6H_5CH_3$)[Mn(Ar*-3,5-^{i}Pr$_2$)]$_2$ (Ar*=C_6H_3-2,6-Trip$_2$, Trip=C_6H_2-2,4,6-^{i}Pr$_3$) synthesized by Ni *et al*. was reported to take singlet.[10]

Electronic structures of these ISTCs are of considerable interest from the point of view of physical chemistry, coordination chemistry, and material science. Fernandez *et al.* theoretically studied the ISTC of group-13 non-transition metals.[11] But, no theoretical work has been reported on ISTC of transition metals. In this work, we theoretically investigated

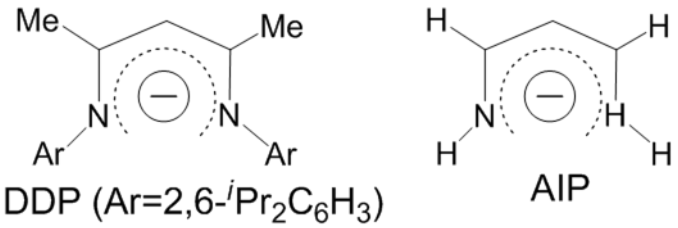

Scheme 2-2. DDP and AIP ligands (DDPH = 2-{4-{(2,6-diisopropyllhenyl) imino} pent-2-ene, AIPH= (*Z*)-1-amino-3-imino-prop-1-ene)

various ISTCs of the first-row transition metals, (μ-η^6:η^6-C_6H_6)[*M*(DDP)]$_2$ (**B$_M$**, M = Sc - Fe). Our main purposes here are to clarify the electronic structure and spin state of the ISTC and theoretically predict how much high spin state is presented in the ISTC by changing the transition metal element.

2. Models and Computational details

2-1 Model complexes

Because the real complexes, **T$_{Cr}$** and **B$_{Cr}$**, are very large, we employed models, **MT$_{Cr}$** and **MB$_{Cr}$**, respectively, in preliminary calculations, as shown in Scheme 2-1. In both models, the DDP ligands were replaced with AIP ligands (AIPH = 1-amino-3-imono-prop-1-ene; see Scheme 2-2).

We investigated **B$_{Cr}$** and **MB$_{Cr}$** in D_2 symmetry, where Cr(DDP) and Cr(AIP) moieties were fixed to be planar because the six-membered ring including chromium atom of the Cr(DDP) moiety was experimentally observed to be almost planar.[6, 7] **MB$_{Cr}$** takes D_{2h} symmetrical structure, when the dihedral angle between two Cr(AIP) moieties of **MB$_{Cr}$** is zero and benzene is on the reflection mirror. **T$_{Cr}$** and **MT$_{Cr}$** take C_1 symmetrical structure because the presence of toluene lowers symmetry.

2-2 Computational details

The geometries of **MB$_M$** and **MT$_M$** were optimized by the DFT method with B3LYP,[12,13] B3LYP*,[14] BP86,[12,15] and PW91PW91[16] functionals. The total energies of these models were evaluated by the DFT, CASSCF,[17] and MRMP2[17] methods. To examine the non-dynamical correlation effect in the geometry optimization, we also applied the CASSCF method to the geometry optimization of **MB$_M$** in the singlet to nonet spin states under D_2 symmetry, where the M-M distance was taken as the coordinate and the geometry of the remaining moiety was optimized at each M-M distance. Using the CASSCF-optimized geometry at each M-M distance, the potential energy surface (PES) was evaluated by the MRMP2 method. We introduced the energy denominator shift (EDS) in the MRMP2 calculations, where the EDS value of 0.02 a.u. was employed throughout the present study. Note that EDS little affected the equilibrium distance of R(Cr-Cr) in **MB$_{Cr}$** in the septet spin

Table 1. Energies[a] of $\mathbf{MB_{Cr}}$ calculated by the DFT method.

	B3LYP	B3LYP*	BP86	PW91PW91
11tet	46.0	48.5	56.3	56.6
9tet	24.7	26.9	32.8	33.0
7tet	0.0	0.0	0.0	0.0
5tet	38.5	43.2	12.5	13.4
3let	32.1	27.3	15.9	17.8
1let	45.4	37.6	19.0	20.9

[a] Relative energies to the septet spin state (in kcal/mol).

state, as shown in Figure A2-1, where the EDS values of 0.005, 0.01, and 0.02 a.u. were employed.

The BP86 functional was employed in the geometry optimization of the real complex $\mathbf{B_M}$ because the BP86-optimized geometry agrees well with the experimental structures of both V and Cr complexes, as shown below. The total energy E^M_{real} of real system $\mathbf{B_M}$ was evaluated by the ONIOM method.[18] The ONIOM-calculated energy is represented by

$$E^M_{real} = E^M_{real,low} - E^M_{\mathrm{mod}\,el,low} + E^M_{\mathrm{mod}\,el,high}, \qquad (1)$$

where $E^M_{real,low}$ and $E^M_{\mathrm{mod}\,el,low}$ are the energies of $\mathbf{B}_M$ and $\mathbf{MB_M}$ calculated by the DFT, and $E^M_{\mathrm{mod}\,el,high}$ is that of the model system calculated by either the CASSCF or the MRMP2 method. Each energy value is calculated separately and assembled according to eq. (1). They are named ONIOM(CASSCF: DFT) and ONIOM(MRMP2: DFT), respectively, hereafter.

Core electrons of the first-row transition metals (up to 2p) were replaced with Stuttgart-Dresden-Born effective core potentials (ECPs), and their valence electrons were represented with (311111/22111/411/1) basis set.[19] For C, N, and H, cc-pVDZ basis sets were employed.[20] The augmented functions were added to N because it is anionic in DDP and AIP.

Gaussian 03 package[21] was used for DFT calculation, and GAMESS package[22] was used for CASSCF and MRMP2 calculations. Molecular orbitals were drawn with Molekel ver. 5.3.[23]

3. Results and Discussions

First, we wish to discuss geometry, orbital diagram, and spin states of ISTCs of

chromium and vanadium, because they were experimentally reported. We employed model and real complexes, here. Then, we will report computational prediction of spin multiplicity of the other first-row transition metal complexes which have not been synthesized.

3-1 Geometries and spin states of $(\mu\text{-}\eta^6\text{:}\eta^6\text{-}C_6H_6)[Cr(AIP)]_2$ (MB_{Cr}) and $(\mu\text{-}\eta^6\text{:}\eta^6\text{-}C_7H_8)[Cr(AIP)]_2$ (MT_{Cr})

We optimized the geometries of the model complex, $\mathbf{MB_{Cr}}$, from singlet to undectet spin states under D_2 symmetry using the DFT method. The septet spin state was calculated to be the most stable with all functionals, as shown in Table 2-1; we abbreviate singlet, triplet, quintet, septet, nonet, and undectet spin states as 1let, 3let, 5tet, 7tet, 9tet, and 11tet, respectively, in all Tables and Figures hereafter. This result agrees with the experimental result that $\mathbf{B_{Cr}}$ takes septet state.[6,7] All functionals employed here present good agreement of optimized geometry with the experimental one, where the B3LYP presents slightly better

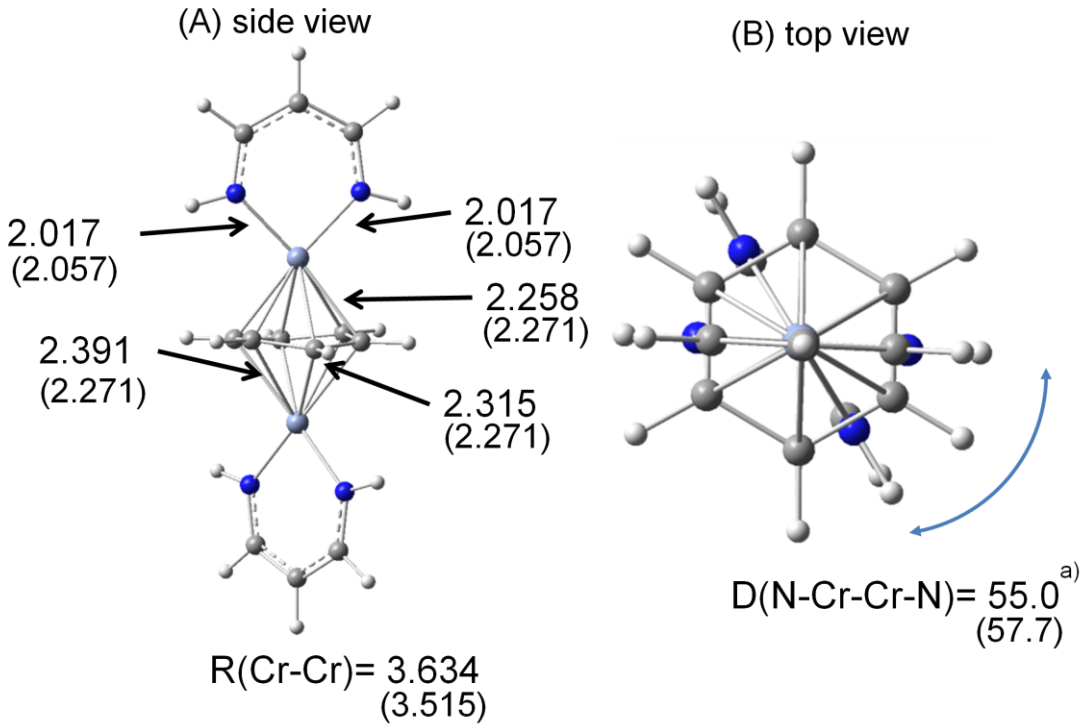

Figure 2-1. Optimized geometry of $\mathbf{MB_{Cr}}$ by the DFT (B3LYP) method in the septet state under D_2 symmetry. Parentheses represent experimental values. Length in Å and angle in degree.
[a] Dihedral angle

agreement than the others, as shown in Figure 2-1 and Table A2-1.

We also optimized the geometry of the model complex, $\mathbf{TB_{Cr}}$, by the DFT method with the B3LYP functional in the septet spin state under C_1 symmetry. The optimized geometry agrees well with the experimental structure,[6,7] as shown in Figure S2-2, indicating that $\mathbf{MB_{Cr}}$ and $\mathbf{MT_{Cr}}$ are good models of $\mathbf{B_{Cr}}$ and $\mathbf{T_{Cr}}$, respectively. Also, it is noted that no significant difference is observed between the geometries of $\mathbf{MB_{Cr}}$ and $\mathbf{MT_{Cr}}$. In the next section, therefore, we will mainly discuss $\mathbf{MB_{Cr}}$ and $\mathbf{B_{Cr}}$ instead of $\mathbf{MT_{Cr}}$ and $\mathbf{T_{Cr}}$.

3-2 Orbital Interaction Diagram of the Cr(AIP) Moiety

In this section, we wish to discuss the molecular orbital (MO) interaction diagram to understand the reason why $\mathbf{B_{Cr}}$ takes septet spin state as the ground state. Because $\mathbf{B_{Cr}}$ is considered to consist of two Cr(DDP) moieties and benzene, we first examine the MO diagram of the Cr(AIP) moiety which is a model of Cr(DDP). In the Cr(AIP) moiety, MOs of AIP anion interact with five 3d atomic orbitals (AOs) of Cr(I). Four MOs of the AIP anion are energetically near the 3d orbitals of Cr, as shown in Scheme 2-3. They are named π1(AIP), π2(AIP), lp1(AIP), and lp2(AIP), hereafter, where the "lp" represents lone pair orbital. These four orbitals belong to the different irreducible representations in the C_{2v} symmetry.

The d_{xz} of Cr strongly interacts with the lp2(AIP) to form a bonding orbital π2(CA) and an anti-bonding orbital $\pi2^*$(CA), where "CA" is an abbreviation of Cr(AIP). The energy destabilization of $\pi2^*$(CA) is very large because the d_{xz} orbital overlaps well with the lone pair orbital of AIP anion in σ manner. The d_{yz} somewhat interacts with the π2(AIP) to form a bonding MO π1(CA) and an anti-bonding MO $\pi1^*$(CA). The overlap between the d_{yz} and the π2(AIP) is less than that between the d_{xz} and the lp2(AIP) because the d_{yz} and π2(AIP) expand in π direction with respect to the Cr-N bond. The d_{xy} interacts with the π1(AIP) to form a bonding MO δ2(CA) and an anti-bonding MO $\delta2^*$(CA). The overlap between the d_{xy} and π1(AIP) is less than that between the d_{yz} and the π2(AIP) because the π1(AIP) expands perpendicular to the Cr-N bond and overlaps with the d_{xy} in δ manner. Consequently, the $\pi2^*$(CA) is at the highest energy, the $\pi1^*$(CA) is at the second highest energy, and the $\delta2^*$(CA) is at the lowest energy in these three MOs.

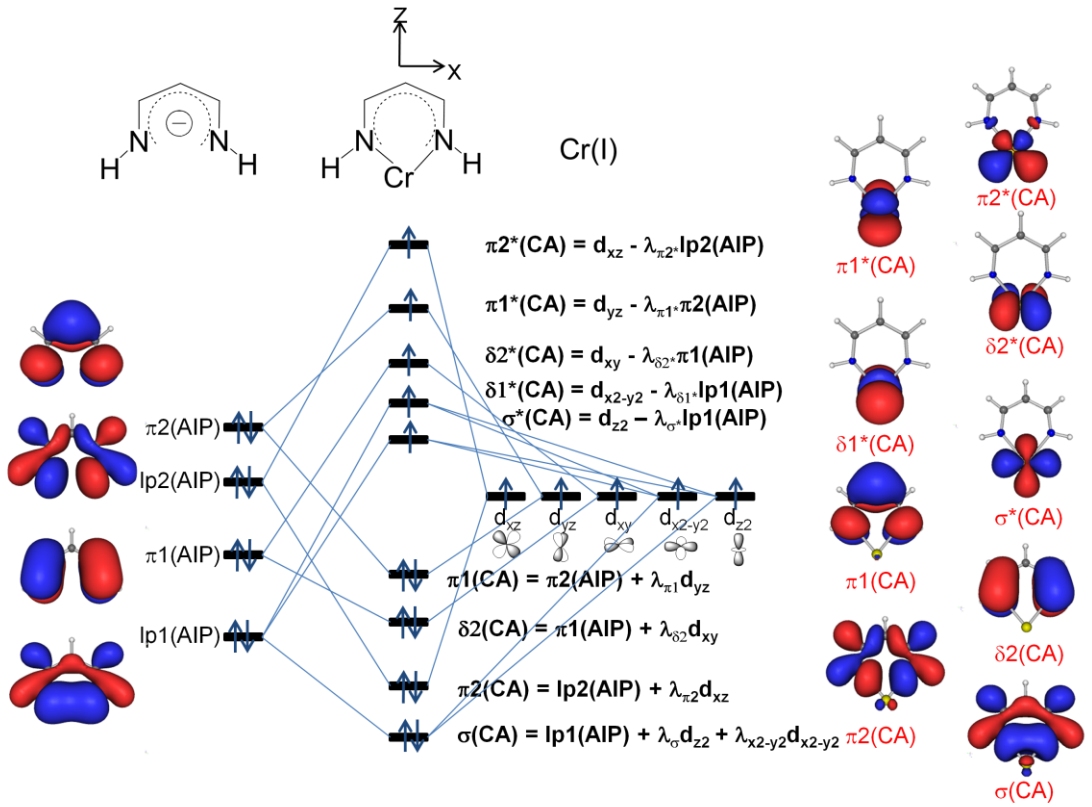

Scheme 2-3. MO diagram of the Cr(AIP) moiety. "CA" is an abbreviation of Cr(AIP).

Because the other three orbitals, lp1(AIP), $d_{x^2-y^2}$, and d_{z^2}, belong to the same irreducible representation in the C_{2v} symmetry, they interact with each other to form three MOs, σ(CA), $\delta1^*$(CA), and σ^*(CA), which mainly consist of the lp1(AIP), $d_{x^2-y^2}$, and d_{z^2}, respectively; see Scheme 2-3. The energy destabilization of $\delta1^*$(CA) and σ^*(CA) and the energy stabilization of σ(CA) are very small because the energy gap between lp1(AIP) and the 3d of Cr are very large. Thus, the $\delta1^*$(CA) and the σ^*(CA) lie at similar energy below the $\delta2^*$(CA).

In these MOs, totally 13 electrons are involved; five electrons in Cr(I) and four electrons of two N lone pair orbitals, and four electrons of two π orbitals of AIP. Among these orbitals, the σ(CA), π2(CA), δ2(CA), and π1(CA) lie at much lower energy than the other five MOs, the $\pi2^*$(CA), $\pi1^*$(CA), $\delta2^*$(CA), $\delta1^*$(CA), and σ^*(CA) MOs, as shown in Scheme 2-3; the former four MOs are doubly occupied and the latter five MOs are singly occupied.

3-3 Bonding Nature of MB_{Cr} in D_{2h} Symmetry

We will inspect here bonding interaction of $\mathbf{MB_{Cr}}$ by separating it to two parts, benzene and a pair of two Cr(AIP) moieties ($\mathbf{CA_2}$). First, we discuss $\mathbf{MB_{Cr}}$ in D_{2h} symmetry. MOs of Cr(AIP) mentioned above construct bonding and anti-bonding MOs in $\mathbf{CA_2}$, as follows: The $\sigma^*(CA)$, $\delta1^*(CA)$, $\delta2^*(CA)$, $\pi1^*(CA)$, and $\pi2^*(CA)$ orbitals form $\sigma(CA_2)$ and $\sigma^*(CA_2)$, $\delta1(CA_2)$ and $\delta1^*(CA_2)$, $\delta2(CA_2)$ and $\delta2^*(CA_2)$, $\pi1(CA_2)$ and $\pi1^*(CA_2)$, and $\pi2(CA_2)$ and $\pi2^*(CA_2)$ orbitals, respectively, as shown in Figure S2-3.

MOs of the total complex are constructed by these MOs of $\mathbf{CA_2}$ and MOs of benzene. Degenerate HOMOs (HOMO1 and HOMO2) and degenerate LUMOs (LUMO1 and LUMO2) of benzene mainly participate in the interaction with $\mathbf{CA_2}$. Because the phases of these MOs are always opposite in the upper side of benzene to those in the lower side, the $\sigma(CA_2)$, $\delta1(CA_2)$, $\delta2(CA_2)$, $\pi1(CA_2)$, and $\pi2(CA_2)$ orbitals do not interact with the HOMO1, HOMO2, LUMO1 and LUMO2 at all; note that the phases of the $\sigma(CA_2)$, $\delta1(CA_2)$, $\delta2(CA_2)$, $\pi1(CA_2)$, and $\pi2(CA_2)$ orbitals are different from the HOMOs and LUMOs of benzene as shown in Figure S2-3. In $\mathbf{MB_{Cr}}$, we name them ϕ_6, ϕ_7, ϕ_8, ϕ_9, and ϕ_{11}, respectively, as shown in Scheme 2-4.

The LUMO1 and LUMO2 have two nodes on the π plane, as well known, while the $\sigma^*(CA_2)$ has no node and the $\pi1^*(CA_2)$ and $\pi2^*(CA_2)$ have one node. Because of those symmetrical features, the $\sigma^*(CA_2)$ does not interact with HOMOs and LUMOs of benzene. We rename $\sigma^*(CA_2)$ as ϕ_5 in Scheme 2-4. Though the $\pi1^*(CA_2)$ and $\pi2^*(CA_2)$ little interact with the LUMO1 and LUMO2 of benzene due to the above-mentioned symmetrical features, the HOMO1 interacts with the $\pi1^*(CA_2)$ to form bonding ϕ_1 and anti-bonding ϕ_{10} orbitals and the HOMO2 interacts with the $\pi2^*(CA_2)$ to form bonding ϕ_2 and anti-bonding ϕ_{12} orbitals. The remaining two orbitals, $\delta1^*(CA_2)$ and $\delta2^*(CA_2)$, strongly interact with the LUMO1 and LUMO2 to form ϕ_3, ϕ_4, ϕ_{13}, and ϕ_{14} orbitals. The ϕ_3 and ϕ_4 orbitals are bonding, while the ϕ_{13} and ϕ_{14} are anti-bonding between Cr atoms and benzene.

Though the orbital interactions mentioned above are a little different between D_{2h} and D_2 symmetries, both the MO energies and MO features of the D_2 symmetry are essentially the same as those of the D_{2h} symmetry. Hence, we will present our discussion based on the MO diagram in the D_{2h} symmetry hereafter; see Scheme 2-4 for MO energy diagram in the

D_{2h} symmetry and Figure 2-2 for their MOs in the D_2 symmetry. See Supporting Information (Figure A2-4) for details about MO diagram in the D_2 symmetry.

Because Cr(I) has five d-electrons and benzene has four electrons in HOMOs, totally fourteen electrons occupy the above discussed MOs in **MB_{Cr}**. The two orbitals, ϕ_1 and ϕ_2, exist at very low energy because they mainly consist of HOMOs of benzene. The ϕ_3 and ϕ_4 orbitals exist also at low energy because of the large bonding overlaps of $\delta 1^*(CA_2)$ and $\delta 2^*(CA_2)$ with the LUMO1 and LUMO2 of benzene. Thus, these four orbitals are doubly occupied in **MB_{Cr}**. The ϕ_5, ϕ_6, ϕ_7, ϕ_8, ϕ_9, and ϕ_{10} orbitals are not very unstable in energy because they are essentially non-bonding between benzene and **CA_2**. Because they are above the ϕ_3 and ϕ_4 orbitals and nearly degenerate, they are singly occupied by remaining six electrons. On the other hand, the ϕ_{11} and ϕ_{12} orbitals, which mainly consist of the singly occupied $\pi 2(CA_2)$ and $\pi 2^*(CA_2)$ orbitals in **CA_2**, are unoccupied in **MB_{Cr}** because the ϕ_{11} and ϕ_{12} exist at higher energy than the ϕ_3 to ϕ_{10}. Actually, this electron configuration is presented

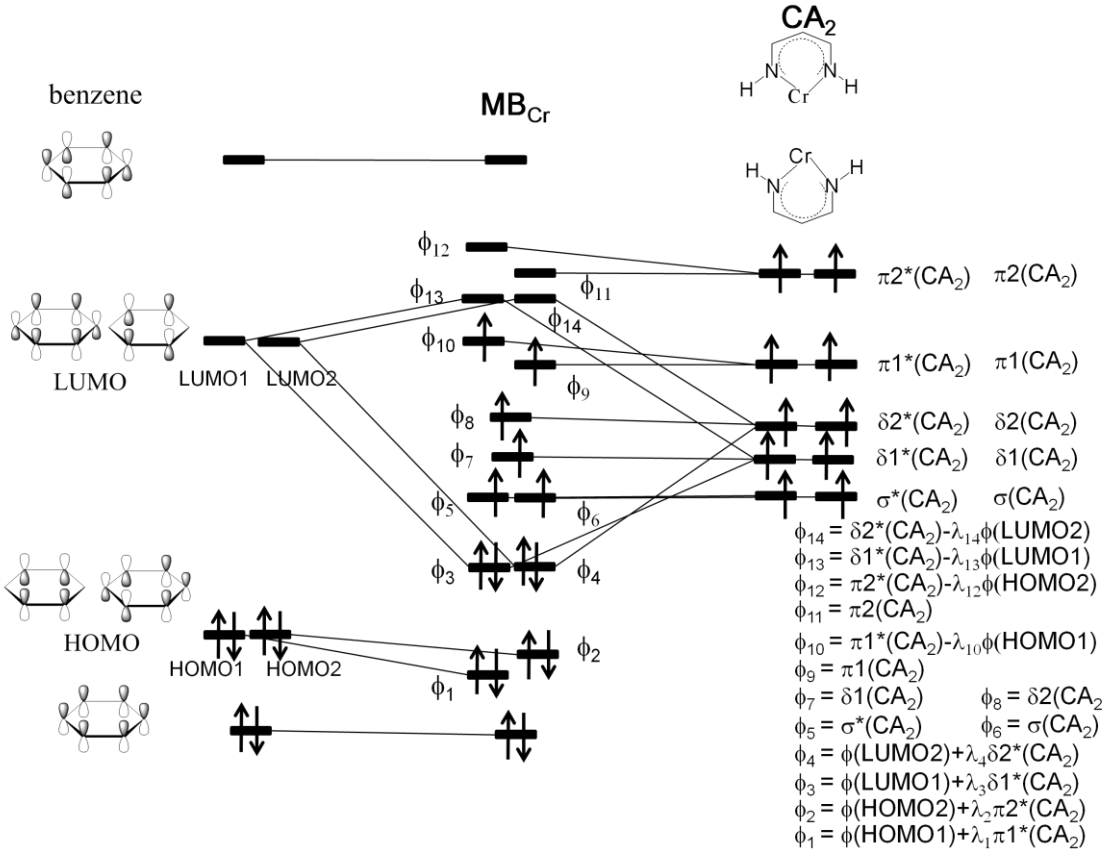

Scheme 2-4. MO diagram of $(\mu\text{-}\eta^6\text{:}\eta^6\text{-}C_6H_6)[Cr(AIP)]_2$ (**MB_{Cr}**)

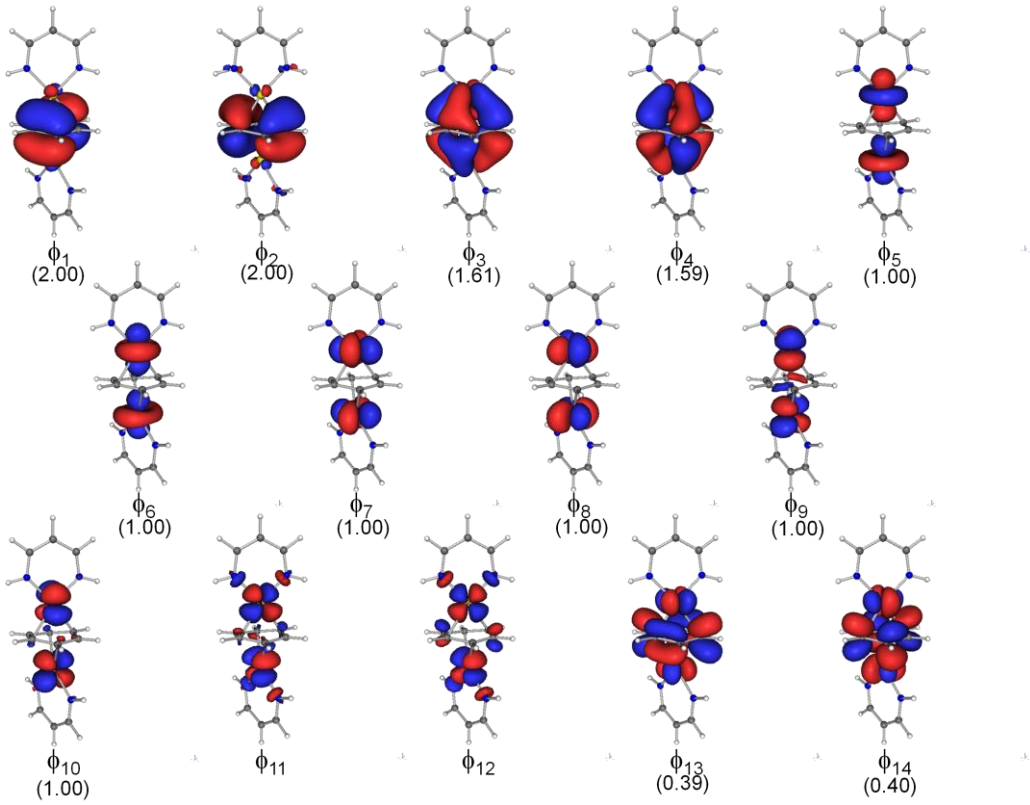

Figure 2-2. CASSCF(10,10)-optimized MOs of $\mathbf{MB_{Cr}}$ in D_2 symmetry. Numbers in parentheses represent CASSCF(10,10)–calculated occupation numbers of natural orbitals.[a]
a: We present the occupation numbers of the natural orbitals here, since the natural orbital resembles well the CASSCF-optimized MO.

by our DFT computation. Thus, the septet spin state of $\mathbf{B_{Cr}}$ is successfully understood by the orbital interactions shown in Scheme 2-4.

3-4 Electronic structure of $\mathbf{MB_{Cr}}$

Because non-dynamical correlation effect is very large in the dinuclear Cr complexes as well known,[24-26] we investigated $\mathbf{MB_{Cr}}$ in singlet to undectet spin states with the CASSCF and MRMP2 methods, where DFT-optimized geometry of the septet state was employed. Ten electrons in such ten orbitals as ϕ_3, ϕ_4, ϕ_5, ϕ_6, ϕ_7, ϕ_8, ϕ_9, ϕ_{10}, ϕ_{13}, and ϕ_{14} were involved in the active space of the CASSCF calculation. We also carried out the CASSCF calculation with ten electrons in such 12 orbitals as the ϕ_3 to ϕ_{14}, but the weights of the ϕ_{11} and ϕ_{12} were very small, being less than 0.01. This result indicates that the active space of ten electrons in ten orbitals is reasonable. The CASSCF wavefunction was used as the reference of the MRMP2 calculation. The CASSCF and MRMP2 calculations indicate that the septet state

is the most stable, as shown in Figure 2-3. The next stable spin state was quintet, which was calculated with the CASSCF and MRMP2 methods to be less stable than the septet state by 5.6 and 6.7 kcal/mol, respectively. The CASSCF-calculated relative energies of the quintet, triplet, and singlet spin states to the septet spin state are almost the same as those of MRMP2-calculated ones, as shown in Figure 2-3, indicating that the relative energies of these spin multiplicities are mainly determined by electron configurations of the ϕ_3 to ϕ_{14} and that the dynamical correlation effect on the total energy is similar in the septet, quintet, triplet, and singlet spins states.

The CASSCF wavefunction of the septet spin state mainly consists of $(\phi_3)^2(\phi_4)^2(\phi_5)^1(\phi_6)^1(\phi_7)^1(\phi_8)^1(\phi_9)^1(\phi_{10})^1$, $(\phi_3)^1(\phi_4)^2(\phi_5)^1(\phi_6)^1(\phi_7)^1(\phi_8)^1(\phi_9)^1(\phi_{10})^1(\phi_{13})^1$, and $(\phi_3)^2(\phi_4)^1(\phi_5)^1(\phi_6)^1(\phi_7)^1(\phi_8)^1(\phi_9)^1(\phi_{10})^1(\phi_{14})^1$ configurations, and their weights (square of the coefficient of each spin configuration) are 0.472, 0.143, and 0.136, respectively. The weights of the remaining electron configurations were very small (less than 0.06). The main configuration is the same as the DFT-computational configuration shown in Scheme 2-4. The second and third leading configurations correspond to one electron excitation from the bonding orbital ϕ_3 to the antibonding orbital ϕ_{13} and that from the ϕ_4 to the ϕ_{14}, respectively. The CASSCF-calculated occupation numbers of the natural orbitals are 1.61 and 1.59 for the bonding ϕ_3 and ϕ_4 orbitals, respectively, 0.39 and 0.40 for the anti-bonding ϕ_{13} and ϕ_{14}, respectively, and almost 1.00 for the other six orbitals, ϕ_5 to ϕ_{10} which mainly consist of d orbitals, as shown in Figure 2-2. Because the natural orbitals were essentially the same as the CASSCF-optimized MOs illustrated in Figure 2-2, we will present the occupation numbers of the CASSCF-optimized MOs below. All these results clearly indicate that the ground state of $\mathbf{MB_{Cr}}$ is the septet spin state. Also, above results indicate that three spins on one Cr atom are strongly coupling with three spins of the other Cr atom in ferromagnetic manner. This is of considerable interest, because such ferromagnetic coupling occurs despite of the absence of benzene orbital between the two spin centers in these MOs; see Figure 2-2.

The formal bond order between Cr atom and benzene is two, since there are two doubly-occupied bonding orbitals between them. However, the electron occupation of the anti-bonding orbitals decreases it to *ca.* 1.2 (= (1.61+1.59-0.39-0.40)/2).

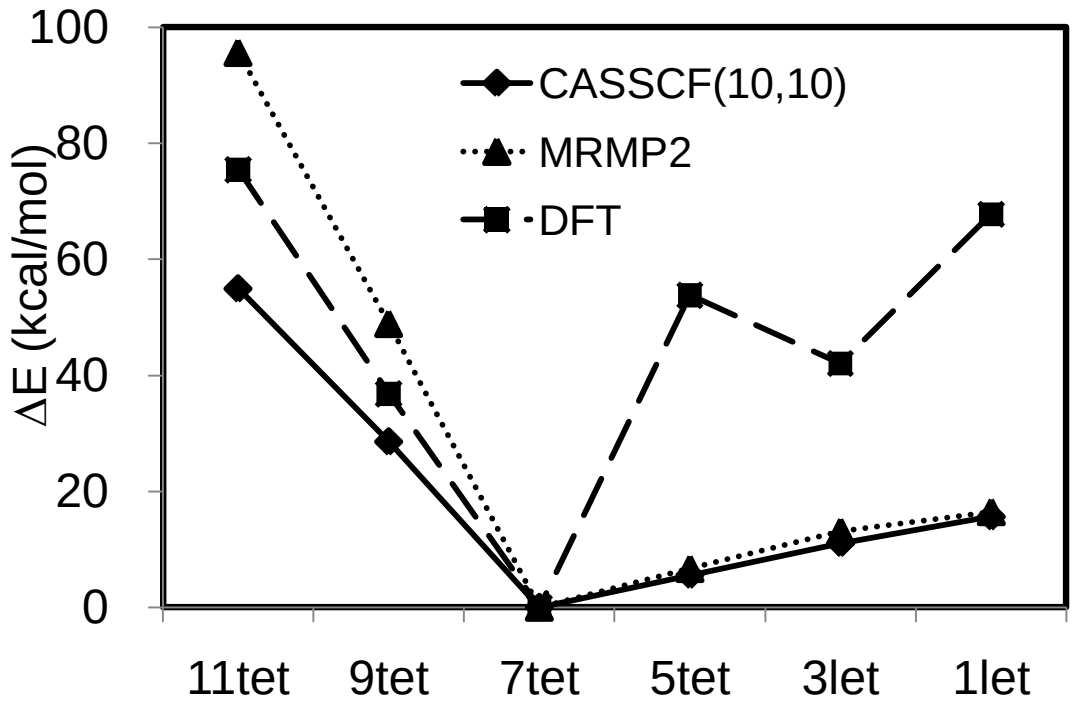

Figure 2-3. Energies (in kcal/mol) of various spin multiplicities of $\mathbf{MB_{Cr}}$ relative to the energy of the 7tet spin state[a]

[a] The DFT(B3LYP)-optimized geometry in the 7tet state was employed in the CASSCF and MRMP2 calculations.

We also calculated $\mathbf{MT_{Cr}}$ by the DFT(B3LYP), CASSCF, and MRMP2 methods. No significant difference was observed in the relative energies of various spin states between $\mathbf{MB_{Cr}}$ and $\mathbf{MT_{Cr}}$, as shown in Figure A2-5. This indicates that substitution of toluene of $\mathbf{MT_{Cr}}$ for benzene induces little influence in both geometry and electronic structure. From all these results, it should be concluded that $\mathbf{MB_{Cr}}$ is a good model for $\mathbf{MT_{Cr}}$.

We carried out the CASSCF(10,10) optimization of $\mathbf{MB_{Cr}}$ in each spin state with Cr-Cr distance fixed. The PES in each spin state smoothly decreases as the Cr-Cr distance increases, as shown in Figure A2-6, but the equilibrium structure is not presented in the range of R(Cr-Cr) = 3.2 Å to 3.8 Å. However the PES by the MRMP2 method presents the energy minimum at R(Cr-Cr) = 3.374 Å in the septet spin state, as shown in Figure 2-4; though this is somewhat shorter than the experimental result by 0.14 Å,[7] this error is not so large because two Cr atoms are separated by a benzene ring and the error in the Cr-X distance (X = the center of benzene) is 0.07 Å; see Figure A2-7 for the CASSCF-optimized geometry at R(Cr-Cr) = 3.40 Å. These results indicate that the dynamical correlation as well as non-dynamical correlation plays important roles in determining the Cr-Cr distance.

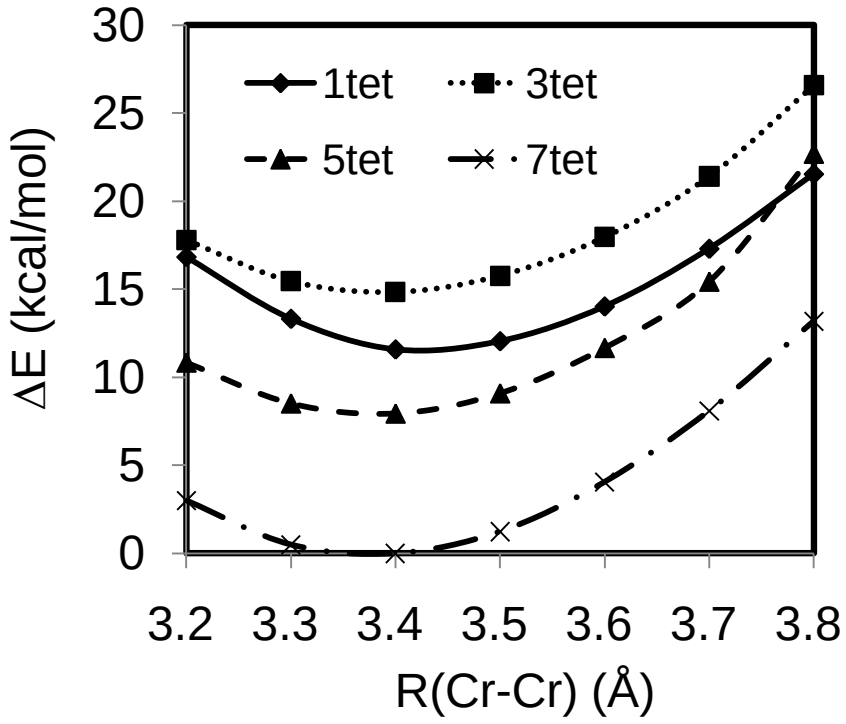

Figure 2-4. Potential energy surface of $\mathbf{MB_{Cr}}$ calculated by the MRMP2 method.[a]
a: The geometry was optimized with the CASSCF(10,10) method at various Cr-Cr distance in each spin state.

The relative stabilities of the septet, quintet, triplet, and singlet spin states are little different in the range of 3.2 Å < R(Cr-Cr) < 3.7 Å between CASSCF-optimized geometries and B3LYP-optimized ones. Since the dynamical correlation effect on the total energy is similar in each spin state as mentioned above, it is expected that the relative stability among these spin states is given correctly at the CASSCF-optimized geometry.

The bond order between the Cr and benzene was calculated to be 1.3 at the CASSCF-optimized geometry which is moderately larger than that at B3LYP-optimized geometry, as expected; see Table 2-2 for the occupation numbers of the natural orbitals at R(Cr-Cr) = 3.40 Å. This is because the Cr-Cr distance is shorter in the MRMP2-optimized geometry than in the B3LYP-optimized geometry.

To take the ligand effect into the calculation, we performed ONIOM(CASSCF:DFT) and ONIOM(MRMP2:DFT) calculations of the real complexes. First, we optimized $\mathbf{B_{Cr}}$ in the septet spin state and $\mathbf{B_V}$ in the quintet spin state using the DFT method with the B3LYP and BP86 functionals. The BP86-optimized structure agrees well with the experimental

Table 2-2. CASSCF-calculated metal-metal distance, spin multiplicity, and the occupation numbers of the model systems, $\mathbf{MB_M}$ (M = V – Fe)

	$\mathbf{MB_V}$	$\mathbf{MB_{Cr}}$	$\mathbf{MB_{Mn}}$	$\mathbf{MB_{Fe}}$
Optimized R(M-M) / Å	3.30	3.40	3.50	3.35
Most stable spin multiplicity (2S+1)				
CASSCF	5	7	9	7
MRMP2	5	7	9	1
Occupation Number				
ϕ_3	1.7968	1.6660	1.5312	1.8710
ϕ_4	1.8018	1.6639	1.5391	1.8633
ϕ_5	1.0000	1.0031	1.0001	1.0045
ϕ_6	0.9980	1.0020	1.0000	0.9956
ϕ_7	0.9946	0.9977	1.0010	1.6929
ϕ_8		0.9967	0.9996	1.5952
ϕ_9		1.0000	1.0000	1.0445
ϕ_{10}		1.0000	1.0000	0.9571
ϕ_{11}			1.0000	1.0450
ϕ_{12}			1.0000	0.9571
ϕ_{13}	0.2052	0.3344	0.4676	0.4336
ϕ_{14}	0.2029	0.3362	0.4615	0.5409

structure;[7,9] R(Cr-Cr) = 3.607 Å (3.515 Å) and R(V-V) = 3.510 Å (3.510 Å), where out of parentheses are optimized values and in parentheses are experimental values. However, B3LYP optimization overestimates metal-metal distance; R(Cr-Cr)=3.724 Å and R(V-V)=3.569 Å. Thus, we employed the BP86 functional in the geometry optimization of $\mathbf{B_{Cr}}$.

In $\mathbf{B_{Cr}}$, the septet spin state was calculated to be the most stable by the ONIOM(CASSCF:BP86) and ONIOM(MRMP2: BP86) methods, as shown in Figure 2-5. This result agrees well with the result of $\mathbf{MB_{Cr}}$. Relative stabilities of various spin states also agree well with the computational results of $\mathbf{MB_{Cr}}$. Even in $\mathbf{MB_{Cr}}$ of the quintet spin state the discrepancy is moderate.[27] The occupation numbers of the natural orbitals obtained by the ONIOM(CASSCF:BP86) method are essentially the same as those of $\mathbf{MB_{Cr}}$; see Table

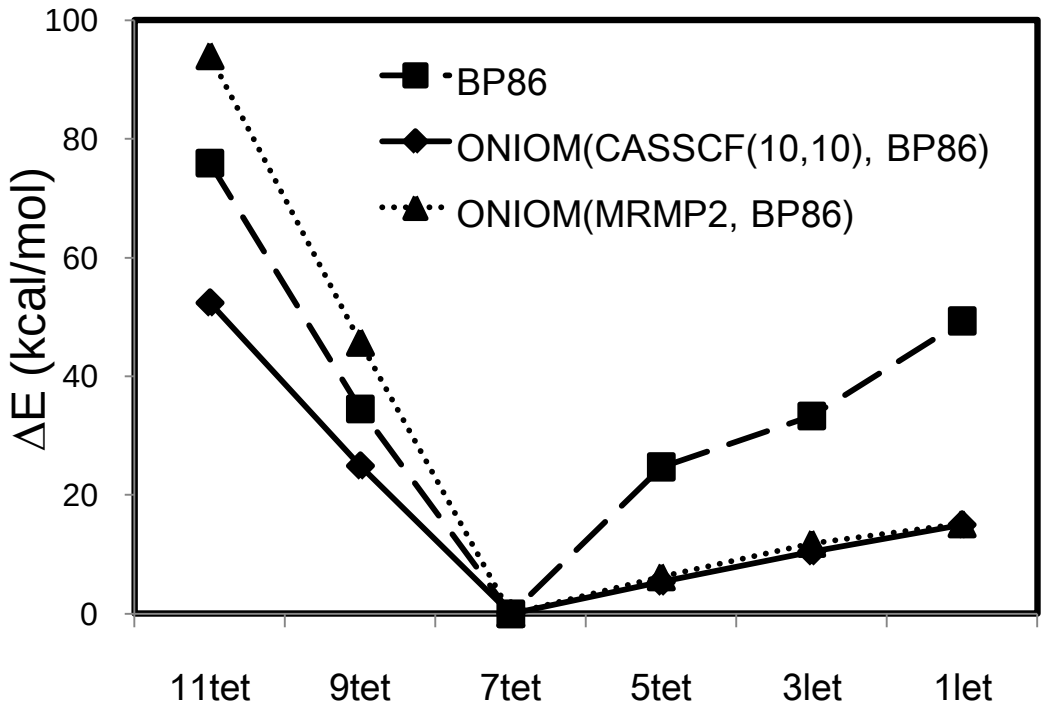

Figure 2-5. Energies of various spin multiplicities of $\mathbf{B_{Cr}}$ relative to that of the 7tet spin state.[a]

[a] The DFT(BP86)-optimized geometry in the 7tet state was employed in the CASSCF and MRMP2 calculations.

A2-2. These results indicate that the substituents of the DDP ligand little influence on the electronic structure of the Cr atom.

3-5 Geometries and Electronic Structure of $(\mu\text{-}\eta^6\text{:}\eta^6\text{-}C_6H_6)[V(AIP)]_2$ ($\mathbf{MB_V}$) and $(\mu\text{-}\eta^6\text{:}\eta^6\text{-}C_6H_6)[V(DDP)]_2$ ($\mathbf{B_V}$)

We optimized the geometry of $\mathbf{MB_V}$ with the DFT(B3LYP) method in singlet to nonet spin states. The quintet spin stet is the most stable at R(V-V) = 3.510 Å. This result agrees with the experimental results that $\mathbf{T_V}$ takes the quintet spin state at R(V-V) = 3.509 Å.[9] The reason why $\mathbf{MB_V}$ takes the quintet spin state is explained by the MO diagram, as follows: Since $\mathbf{MB_V}$ has eight d electrons, two electrons are removed from the ϕ_9 and ϕ_{10} orbitals of $\mathbf{MB_{Cr}}$ (see Scheme 2-4). Because four unpaired electrons remain, the electron configuration of the ground state is represented as $(\phi_3)^2(\phi_4)^2(\phi_5)^1(\phi_6)^1(\phi_7)^1(\phi_8)^1$, which leads to the quintet spin state.

We also optimized the geometry of $\mathbf{MB_V}$ with the CASSCF method, where eight electrons were involved in such eight active orbitals as the ϕ_3, ϕ_4, ϕ_5, ϕ_6, ϕ_7, ϕ_8, ϕ_{13}, and ϕ_{14}

orbitals. Using the CASSCF-optimized geometries, we obtained the PES in each spin state by the MRMP2 method, as shown in Figure A2-8. The quintet state was the most stable and its energy minimum was calculated at R(V-V) = 3.325 Å, which is shorter than the experimental value by 0.184 Å like the PES of $\mathbf{MB_{Cr}}$ by the MRMP2 method. This error is not very large, considering that two V atoms are separated by a benzene ring and the error in the V-X distance (0.092 Å) is less than 0.1 Å. Table 2-2 shows the occupation number of the natural orbitals at R(V-V) = 3.30 Å. We carried out the ONIOM calculations of $\mathbf{B_V}$ to include the ligand effect. The quintet spin state was calculated to be the most stable by both ONIOM(CASSCF:BP86) and ONIOM(MRMP2:BP86) methods, as shown in Figure A2-9. The occupation numbers of the bonding orbitals ϕ_3 and ϕ_4 are about 1.8, those of their anti-bonding counter parts are both 0.20, and those of three d-derived orbitals are all 1.0, as shown in Table A2-2, which are essentially the same as those of the model $\mathbf{MB_V}$.

The bond order between vanadium atom and the benzene ring is evaluated to be *ca.* 1.6, which is much larger than that (1.2) of the chromium analogue. The ϕ_9 and ϕ_{10} are singly occupied in $\mathbf{MB_{Cr}}$ but unoccupied in $\mathbf{MB_V}$. However, these are completely non-bonding, and hence, the occupation change in these orbitals little influences the bond order. The large bond order of $\mathbf{MB_V}$ arises from the energy difference of 3d orbitals between Cr and V, as follows: The bonding orbitals ϕ_3 and ϕ_4 mainly contribute to the bonding interaction between the V center and benzene, as shown in Scheme 2-4, because these orbitals mainly consist of LUMOs of benzene and 3d orbitals of the metal center. Since the 3d orbital energy is higher in V than in Cr, the charge transfer from the metal to benzene more easily occurs in V than in Cr, which leads to the larger bond order in $\mathbf{MB_V}$ than $\mathbf{MB_{Cr}}$. This is the reason why R(V-V) is shorter than R(Cr-Cr) in spite of the larger radius of 3d orbital in V than in Cr.[28]

3-6 Spin States of $(\mu\text{-}\eta^6\text{:}\eta^6\text{-}C_6H_6)[M(AIP)]_2$ ($\mathbf{MB_M}$, M = Early Transition Metals Such as Sc and Ti)

One of our purposes in this work is to present theoretical prediction how to design a compound taking desired spin state. We will first discuss early transition metal analogues such as ISTCs of Sc and Ti.

Though $\mathbf{B}_M$ and $\mathbf{T}_M$ with M = Sc, Ti, Mn, and Fe have not been synthesized yet to our knowledge, we investigated them to predict their spin multiplicities. Here, model system, $\mathbf{MB_M}$, was employed to save the CPU time. This is not unreasonable because the spin state was correctly calculated with the model system in the chromium and vanadium complexes.

We optimized the geometries of $\mathbf{MB_M}$ (M = Sc and Ti) by the DFT method with the B3LYP functional under D_2 symmetry in various spin states, because the DFT(B3LYP) calculations of $\mathbf{MB_{Cr}}$, $\mathbf{MT_{Cr}}$, $\mathbf{B_{Cr}}$, $\mathbf{MB_V}$, and $\mathbf{B_V}$ present similar results to those of MRMP2 calculations of chromium and vanadium complexes, as mentioned above.

To check the reliability of the functional, we re-optimize the geometry of $\mathbf{MB_M}$ (M = Sc and Ti) with different functionals. Little difference is observed among B3LYP, B3LYP*, BP86, and PW91PW91 functionals, as shown in Table A2-3.

The most stable spin state is singlet and triplet for $\mathbf{MB_{Sc}}$ and $\mathbf{MB_{Ti}}$, respectively, as shown in Table 2-3, where the relative energies to the most stable spin state are also shown. In other words, the spin multiplicity increases when going from Sc to Cr in the periodic table interestingly.

These results of $\mathbf{MB_M}$ (M = Sc and Ti) are easily understood by removing four electrons from the electron configuration of $\mathbf{MB_{Cr}}$ (Scheme 2-4) when M = Ti, and six electrons when M = Sc. Therefore, the electron configurations of $\mathbf{MB_{Sc}}$ and $\mathbf{MB_{Ti}}$ are represented as $(\phi_3)^2(\phi_4)^2(\phi_5)^1(\phi_6)^1$ and $(\phi_3)^2(\phi_4)^2$, respectively.

3-7 Electronic Structure of $(\mu\text{-}\eta^6\text{:}\eta^6\text{-}C_6H_6)[Mn(AIP)]_2$ ($\mathbf{MB_{Mn}}$)

However, it is not easy to predict the most stable spin state of $\mathbf{MB_M}$ (M = Mn or Fe)

Table 2-3. Relative energies[a] of various spin multiplicities calculated by the DFT (B3LYP) method

	Sc	Ti	V	Cr	Mn[b]	Fe[b]
9tet			53.8	24.7	106.4 (**0.0**)	
7tet		44.2	33.5	**0.0**	10.2 (5.9)	111.6 (18.1)
5tet	66.3	18.6	**0.0**	38.5	**0.0** (12.1)	2.7 (15.8)
3let	27.6	**0.0**	19.9	32.1	29.8 (17.5)	**0.0** (1.98)
1let	**0.0**	25.9	67.3	45.4	28.1 (15.1)	37.5 (**0.0**)

a: Relative energies to the most stable spin state are provided in kcal/mol.
b: The number in the parentheses represent MRMP2-calculated energy at R(Mn-Mn) = 3.5 Å for $\mathbf{MB_{Mn}}$ and R(Fe-Fe) = 3.4 Å for $\mathbf{MB_{Fe}}$.

from the MO diagram, because it cannot be easily understood which orbitals are occupied by additional two or four electrons in Mn or Fe, respectively, compared to **MB_{Cr}**: If the energy levels of the ϕ_{11} and ϕ_{12} are close to those of the ϕ_9 and ϕ_{10}, the additional electrons occupy the ϕ_{11} and ϕ_{12} orbitals according to the Hund's rule. If not, additional electrons occupy energetically lower orbitals.

First, we optimized the geometry of **MB_{Mn}** by the DFT method with the B3LYP, B3LYP*, BP86, and PW91PW91 functionals under D_2 symmetry in various spin states. In the B3LYP calculation, the most stable spin state of **MB_{Mn}** was quintet, as shown in Table 2-3. The electron configuration is $(\phi_3)^2(\phi_4)^2(\phi_5)^2(\phi_6)^2(\phi_7)^1(\phi_8)^1(\phi_9)^1(\phi_{10})^1$. In the other functionals, however, the nonet spin state is the most stable, as shown in Table A2-3. The electron configuration is represented by $(\phi_3)^2(\phi_4)^2(\phi_5)^1(\phi_6)^1(\phi_7)^1(\phi_8)^1(\phi_9)^1(\phi_{10})^1(\phi_{11})^1(\phi_{12})^1$.

We also optimized the geometry of **MB_{Mn}** with the CASSCF method under D_2 symmetry in various spin states, where 12 electrons were involved in such 12 active orbitals as the ϕ_3 to ϕ_{14}. Using the CASSCF-optimized geometry in each spin state, the PES was evaluated by the MRMP2 method. The PES of the nonet spin state was found to lie below that of the septet spin state in the region between 3.2 Å < R(Mn-Mn) < 3.8 Å, as shown in Figure 2-6. The energy minimum of the nonet spin state is found at R(Mn-Mn) = 3.516 Å, which is below the energy minimum of the septet spin state (R(Mn-Mn) = 3.542 Å) by about 6 kcal/mol. Thus, the MRMP2 calculation clearly indicates that **MB_{Mn}** takes nonet spin state in the ground state. It should be noted that this is the maximum spin state in the ISTCs of the first row metals. Because the most stable spin states of **MB_{Cr}** and **MB_V** are correctly reproduced by the MRMP2 method in wide range of the metal-metal distance, as mentioned in section 3-4 and 3-5, we believe that the spin state of **MB_{Mn}** is correctly evaluated with the MRMP2 method, too.

The occupation numbers of the bonding ϕ_3 and ϕ_4 orbitals were 1.53 and 1.54, those of the anti-bonding counterparts ϕ_{13} and ϕ_{14} orbitals are 0.47 and 0.46, and those of all eight d-derived orbitals are 1.00 at R(Mn-Mn) = 3.50 Å, as shown in Table 2-2 and Figure A2-10. The electron configuration of **MB_{Mn}** is therefore represented as $(\phi_3)^2(\phi_4)^2(\phi_5)^1(\phi_6)^1(\phi_7)^1(\phi_8)^1(\phi_9)^1(\phi_{10})^1(\phi_{11})^1(\phi_{12})^1$, indicating that six 3d electrons of one Mn interact with six 3d electrons of the other Mn separated by the benzene ring in paramagnetic

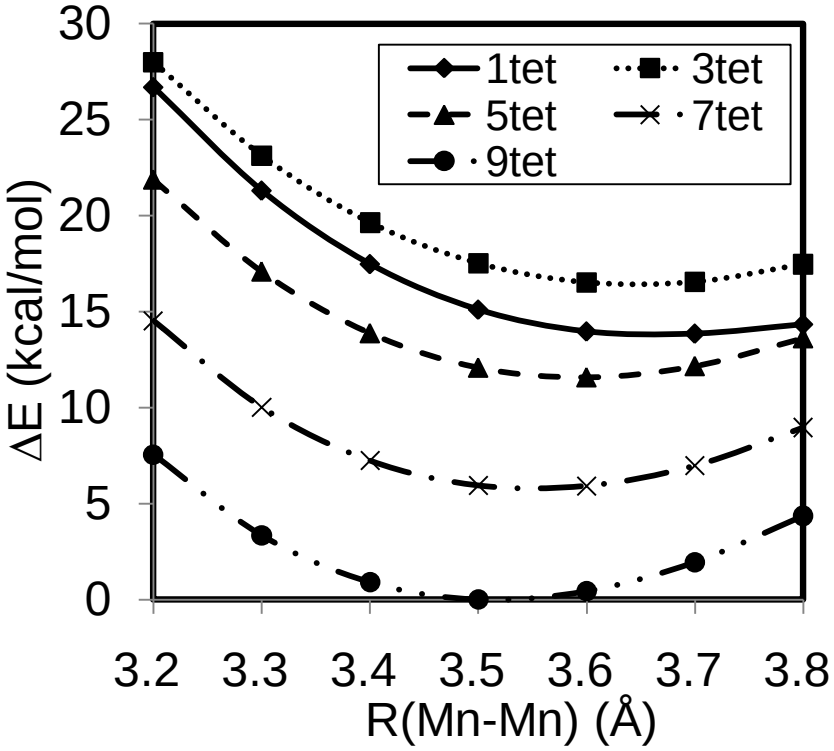

Figure 2-6. Potential energy surface of $\mathbf{MB_{Mn}}$ calculated by the MRMP2 method[a]
a: The geometry was optimized with the CASSCF(12,12) method at various Mn-Mn distances in each spin state.

manor. The bond order between the manganese atom and the benzene ring is evaluated to be *ca.* 1.1, which is moderately smaller than that (1.2) of the chromium complex. This decrease is interpreted in the same way as the increase of the bond order upon going from Cr to V, as discussed in section 3-6; the 3d orbital energy becomes lower in manganese than in chromium, which weakens the charge transfer from Mn to benzene.

To include the ligand effect, we examined the real complex, $\mathbf{B_{Mn}}$, by the ONIOM method in the same way as $\mathbf{B_{Cr}}$ and $\mathbf{B_V}$. The most stable spin state was nonet, like that of the model complex, as shown in Figure A2-11. Note that the optimized geometry of $\mathbf{B_{Mn}}$ under D_2 symmetry has a moderate but nonnegligible imaginary frequency (100.89 *i* cm^{-1}) with the BP86 functional. We further optimized it until imaginary frequency disappeared. The fully optimized geometry is C_2 symmetrical. In this geometry, $\mathbf{B_{Mn}}$ is not a complete ISTC but a distorted ISTC, because the benzene ring does not interact with the metal in an η^6-manner but coordinates with the metal in a η^3-manner. Even in this geometry, nonet spin state is the most stable like the D_2-optimized geometry; see Figures A2-11 and A2-12 for detail of the

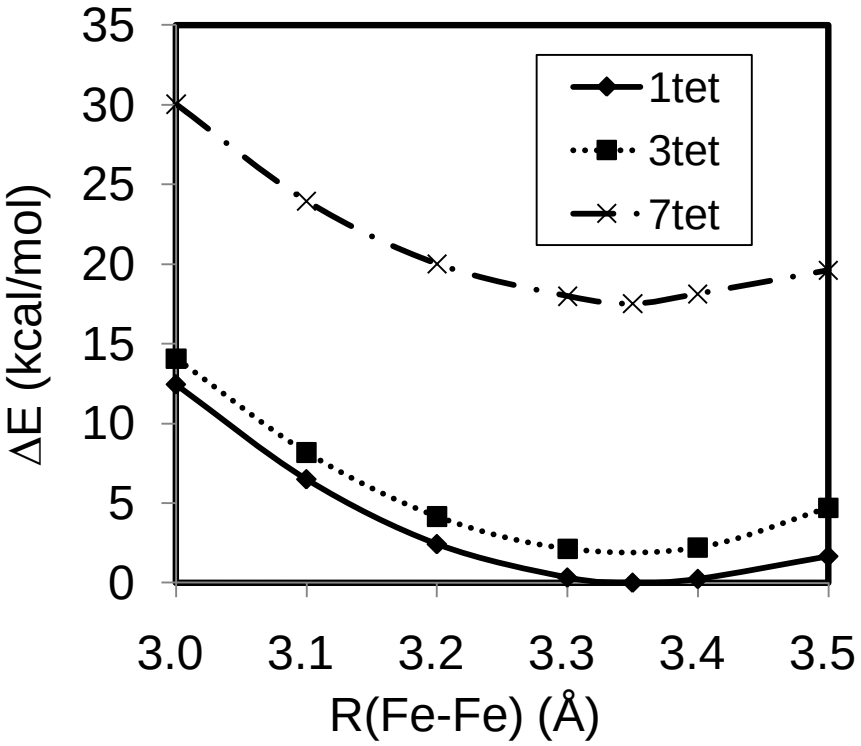

Figure 2-7. Potential energy surface of **MB_{Fe}** calculated by the MRMP2 method[a]
a: The geometry was optimized with the CASSCF(14e,12o) method at various Fe-Fe distances in each spin state.

calculations under the C_2 geometry. Although **B_{Mn}** has not been synthesized yet, the η^6-coordination geometry was reported for the similar ISTC of Mn, $(\mu\text{-}\eta^6\text{:}\eta^6\text{-}C_6H_5CH_3)[Mn(Ar^*\text{-}3,5\text{-}^iPr_2)]_2$ (Ar^* = C_6H_3-2,6-$Trip_2$, Trip = C_6H_2-2,4,6-$^iPr_3$), while the spin multiplicity has not been discussed.[10]

In conclusion, based on the MRMP2 and ONIOM computational results, we wish to present theoretical prediction that the most stable spin state of **B_{Mn}** is nonet. This is the highest spin multiplicity in the ISTCs of the first-row transition metals. Its synthesis is very attractive.

3-8 Electronic Structures of $(\mu\text{-}\eta^6\text{:}\eta^6\text{-}C_6H_6)[Fe(AIP)]_2$ (MB_{Fe}) and its cation MB_{Fe}^{2+}

First, we optimized the geometry by the DFT method with the B3LYP, B3LYP*, BP86, and PW91PW91 functionals. The most stable spin state by the B3LYP functional was triplet, as shown in Table 2-3, whereas it is calculated to be septet, triplet, and triplet by B3LYP*, BP86, and PW91PW91 functionals, respectively, as shown in Table A2-3. These results suggest that the DFT must be carefully applied to $\mathbf{MB_{Fe}}$ probably because of the complex electronic structure of $\mathbf{MB_{Fe}}$. Here, we applied the CASSCF method to the geometry optimization of $\mathbf{MB_{Fe}}$, where 14 electrons in such 12 active orbitals as the ϕ_3 through ϕ_{14} were included in the active space. Using the CASSCF-optimized geometries, the PESs of singlet, triplet, and septet spin states were evaluated by the MRMP2 method. However, the PESs of the quintet spin state is not smooth in both CASSCF and MRMP2 calculations, as shown in Figure A2-14. This is probably because two different states in the quintet spin state lie energetically near in the CASSCF level and their PESs cross with each other around R(Fe-Fe) = 3.2 - 3.3 Å. In the region between 3.0 Å < R(Fe-Fe) < 3.5 Å, the singlet spin state is always more stable than the other spin states by the MRMP2 method, as shown Figure 2-7 and Figure A2-14. The energy minimum in the singlet spin state by the MRMP2 method is at R(Fe-Fe) = 3.349 Å, which is below the energy minimum in the triplet spin state at R(Fe-Fe) = 3.351 Å by about 2 kcal/mol.

Table 2-4. Important electron configurations of the CASSCF wave function of $\mathbf{MB_{Fe}}$ in the singlet spin state[a]

Configuration												Weight
ϕ_3	ϕ_4	ϕ_5	ϕ_6	ϕ_7	ϕ_8	ϕ_9	ϕ_{10}	ϕ_{11}	ϕ_{12}	ϕ_{13}	ϕ_{14}	
2	2	0	2	2	2	0	2	2	0	0	0	0.021814
2	2	0	2	2	2	2	0	0	2	0	0	0.021748
2	2	2	0	2	2	0	2	2	0	0	0	0.020171
2	2	2	0	2	2	2	0	0	2	0	0	0.020136
2	2	1	1	2	2	1	1	2	0	0	0	0.019838
2	2	1	1	2	2	2	0	1	1	0	0	0.019820
2	2	1	1	2	2	0	2	1	1	0	0	0.017068
2	2	1	1	2	2	1	1	0	2	0	0	0.017045

a: R(Fe-Fe) =3.35 Å

The CASSCF-calculated occupation numbers of the natural orbitals (Figure 2-8) in the singlet spin state are shown in Table 2-2: six orbitals (from the ϕ_5 to ϕ_{12} except for the ϕ_7 and ϕ_8) are singly occupied and the other orbitals ϕ_3, ϕ_4, ϕ_7, and ϕ_8 are doubly occupied. This indicates that 14 electrons of two iron atoms form anti-ferromagnetic coupling (low-spin coupling) to form open-shell singlet electron configuration unlike **MB_V**, **MB_{Cr}**, and **MB_{Mn}**. The CASSCF wavefunction consists of various kinds of configurations with the similar weights, as shown in Table 2-4, where eight leading configurations are shown: The first to fourth leading configurations are closed shell type, while the fifth to eighth ones are two-electron excitation configurations. Generally, high spin state is more favorable than low spin state when orbital energies are similar. In the case of **MB_{Fe}**, however, the singlet spin state is more stable than the triplet and septet spin state. This is because contribution of closed shell type configurations from the first to fourth electron configurations (see Table 2-4) considerably lowers the total energy of the singlet spin state enough to overcome the energy

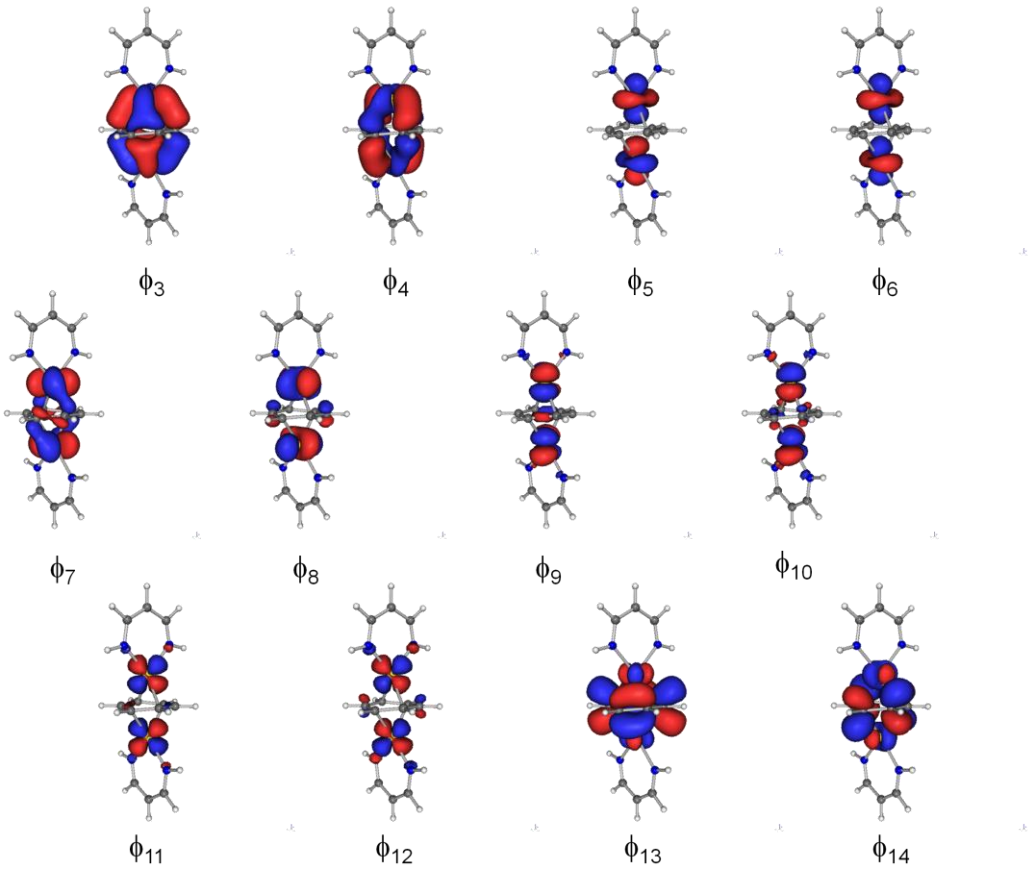

Figure 2-8. CASSCF-optimized MOs of **MB_{Fe}** in D_2 symmetry.

stabilization upon going from the low spin to the high spin state. To take singlet spin state, six electrons in the ϕ_5, ϕ_6, ϕ_9 to ϕ_{12} must induce low-spin coupling. As a result, $\mathbf{MB_{Fe}}$ takes singlet spin state including the low-spin coupling electron configurations.

To include the ligand effect, we also examined the real complex, $\mathbf{B_{Fe}}$, by the ONIOM method like those of $\mathbf{B_V}$, $\mathbf{B_{Cr}}$, and $\mathbf{B_{Mn}}$. Though the septet spin state was calculated to be the most stable by the CASSCF method but the singlet state was calculated to be the most stable by the MRMP2 method. The energy difference between two states is very small like that in $\mathbf{MB_{Fe}}$.

In conclusion, we wish to predict that the most stable spin state of $\mathbf{B_{Fe}}$ is open-shell singlet.

Our theoretical calculations revealed that the most stable spin multiplicity of ISTC increases upon going to Mn from Sc and reaches the maximum, the nonet spin states, at Mn, and then suddenly decreases to the singlet spin state at Fe, interestingly. Considering these results, we expected that $\mathbf{MB_{Fe}}^{2+}$ might take the nonet spin state if two electrons are removed from $\mathbf{MB_{Fe}}$ by two-electron oxidation because the number of electrons in $\mathbf{MB_{Fe}}^{2+}$ is the same as $\mathbf{MB_{Mn}}$. To ascertain this expectation, we calculated $\mathbf{MB_{Fe}}^{2+}$ in the singlet to nonet spin

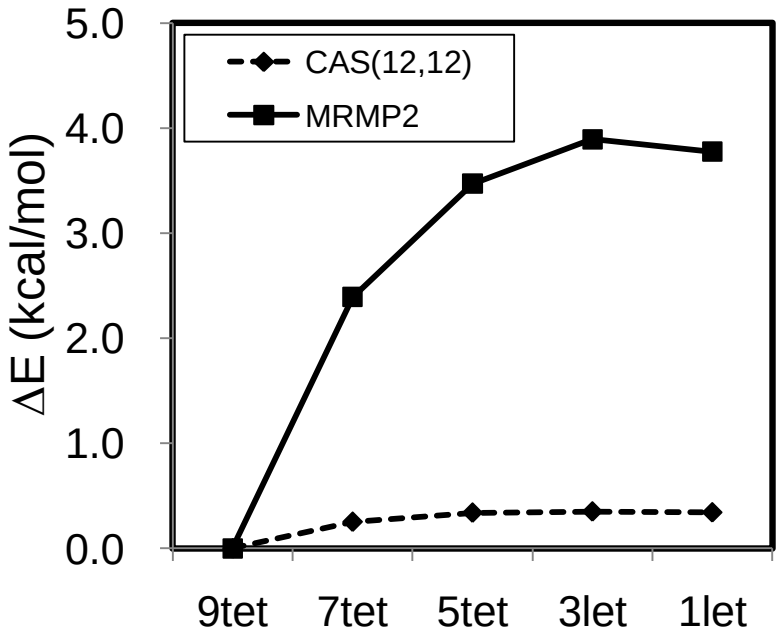

Figure 2-9. Total energies in singlet to septet spin states of $\mathbf{MB_{Fe}}^{2+}$ [a]

[a] Employed is the CASSCF-optimized geometry of $\mathbf{MB_{Fe}}$ at R(Fe-Fe)=3.35 Å.

states at R(Fe-Fe) = 3.35 Å, which is the CASSCF-optimized geometry of the open-shell singlet spin state. As expected, the nonet spin state was calculated to be the most stable by the MRMP2 method and its electronic structure was essentially the same as that of **MB_{Mn}**. However, the energy difference between the nonet spin state and the second stable spin state, which was septet, was small (~ 2.4 kcal/mol), as shown in Figure 2-9. It is of much interest that two electron oxidation induces spin flip from singlet to nonet.

4. Conclusion

We theoretically investigated the inverted sandwich type complex, **B_M** ($(\mu\text{-}\eta^6\text{:}\eta^6\text{-}C_6H_6)[M(DDP)]_2$, DDPH = 2-(4-{(2,6-diisopropyllhenyl)imino}pent-2-ene). First, its septet spin state was qualitatively discussed on the basis of MO diagram which was constructed by MOs of benzene and two Cr(AIP) moieties (AIPH = 1-amino-3-imono-prop-1-ene). Then, model system **MB_{Cr}** was theoretically investigated with the CASSCF and MRMP2 methods. We also investigated **MT_{Cr}** ($(\mu\text{-}\eta^6\text{:}\eta^6\text{-}C_6H_5CH_3)[Cr(AIP)]_2$), and found that the methyl group on toluene little influences both the geometries and the most stable spin state. The quintet spin state of **MB_V** was also interpreted well in terms of the MO diagram of **MB_{Cr}** by removing two electrons from two singly-occupied orbitals at high energy. Next, we optimized the geometries of **MB_M** (M = Sc and Ti) in singlet to nonet spin states with the DFT(B3LYP) method. The most stable spin state of **MB_M** was calculated to be singlet and triplet for Sc and Ti, respectively. These results are understood with the MO diagram, too. The most stable spin states for **MB_{Mn}** and **MB_{Fe}** were calculated to be different between the B3LYP and other functionals such as B3LYP*, BP86, and PW91PW91. In order to predict the most stable spin state for **MB_{Mn}**, **MB_{Fe}**, **MB_V**, and **MB_{Cr}**, we optimized the geometry with the CASSCF method as a function of the M-M distance and investigated spin multiplicities with the MRMP2 method. Though the MRMP2-calculated PES against the M-M distance underestimates the equilibrium distance between two metals in **MB_V** and **MB_{Cr}**, it is clearly shown that the most stable spin states of **MB_V**, **MB_{Cr}**, **MB_{Mn}**, and **MB_{Fe}** are quintet, septet, nonet, and open-shell singlet, respectively.

We also performed ONIOM(CASSCF:BP86) and ONIOM(MRMP2:BP86) calculations

to include the ligand effect, where the whole systems were optimized with the DFT(BP86) method in singlet to undectet spin states. The spin states of $\mathbf{B_V}$, $\mathbf{B_{Cr}}$, $\mathbf{B_{Mn}}$, and $\mathbf{B_{Fe}}$ were calculated with the ONIOM(MRMP2:DFT) method to be quintet, septet, nonet, and singlet spin states, respectively, which are the same as those of the model complexes. These results of $\mathbf{B_V}$ and $\mathbf{B_{Cr}}$ agree well with the experimental results.

In conclusion, we wish to present theoretical prediction that $\mathbf{B_{Mn}}$ takes nonet spin state, which is the highest spin state in inverted sandwich type complexes, but $\mathbf{B_{Fe}}$ takes singlet spin state.

Acknowledgements:

This research was supported in part by the Grant-in-Aids on Priority Area "Molecular Theory for Real Systems" (No. 461) and Global COE Program "International Center for Integrated Research and Advanced Education in Materials Science" (No. B-09) of the Ministry of Education, Culture, Sports, Science and Technology (MEXT) of Japan and the Japan Society for the Promotion of Science. Some of theoretical calculations were performed in Institute for Molecular Science (Okazaki, Japan).

Reference and Note:

(1) Miller, S. A.; Tebboth, J. A.; Tremaine, J. F. *J. Chem. Soc.* **1952**, 653.

(2) Kealy, T. J.; Paulson, P. L. *Nature (London)* **1951**, *168*, 1039.

(3) Sinn, H.; Kaminsky, W.; Vollmer, H.-J.; Rüiger Woldt. *Angew. Chem. Int. Ed. Eng.* **1980**, *19*, 390.

(4) Wilkinson, G.; Stone, F. G. A.; Abel, E. W. *Comprehensive Organometallic Chemistry*; Pergamon Press: New York, 1982; Vol. 1-8.

(5) Swart, M. *Inorg. Chim. Acta* **2007**, *360*, 179.

(6) Tsai, Y.-C.; Wang, P.-Y.; Chen, S.-A.; Chen, J.-M. *J. Am. Chem. Soc.* **2007**, *129*, 8066.

(7) Monillas, W. H.; Yap, G. P. A.; Theopold, K. H. *Angew. Chem. Int. Ed. Eng.* **2007**, *46*, 6692.

(8) Gibson, V. C.; Newton, C.; Redshaw, C.; Solan, G. A.; White, A. J. P.; Williams, D. J. *Eur. J. Inorg. Chem.* **2001**, 1895.

(9) Tsai, Y.-C.; Wang, P.-Y.; Lin, K.-M.; Chen, S.-A.; Chen, J.-M. *Chem. Comm.* **2008**, 205.

(10) Ni, C.; Ellis, B. D.; Fettinger, J. C.; Long, G. J.; Power, P. P. *Chem. Comm.* **2008**, 1014.

(11) Fernandez, I.; Cerpa, E.; Merino, G.; Frenking, G. *Organometallics* **2008**, *27*, 1106.

(12) Becke, A. D. *J. Chem. Phys.* **1993**, *98*, 5648.

(13) Lee, C.; Yang, W.; Parr, R. G. *Phys. Rev. B* **1988**, *37*, 785.

(14) Reiher, M.; Salomon, O.; Hess, B. A. *Theo. Chem. Acc.* **2001**, *107*, 45.

(15) Perdew, J. P. *Phy. Rev. B* **1986**, *33*, 8822.

(16) Perdew, J. P. *Electronic Structure of Solids*; Akademie: Berlin, 1991.

(17) Roos, B. O. *Adv. Chem. Phys.* **1987**, *69*, 399.

(18) Dapprich, S.; Komáromi, I.; Byun, K. S.; Morokuma, K.; Frisch, M. J. *J. Mol. Struct. (THEOCHEM)* **1999**, *461*, 1.

(19) Bergner, A.; Dolg, M.; Kuchle, W.; Stoll, H.; PreuB, H. *Mol. Phys.* **1993**, *80*, 1431.

(20) Dunning, T. H. J. *J. Chem. Phys.* **1989**, *90*, 1007.

(21) Frisch, M. J.; Trucks, G. W.; Schlegel, H. B.; Scuseria, G. E.; Robb, M. A.; Cheeseman, J. R.; Montgomery, J. A., Jr.; Vreven, T.; Kudin, K. N.; Burant, J. C.; Millam, J. M.; Iyengar, S. S.; Tomasi, J.; Barone, V.; Mennucci, B.; Cossi, M.; Scalmani, G.; Rega, N.; Petersson, G. A.; Nakatsuji, H.; Hada, M.; Ehara, M.; Toyota, K.; Fukuda, R.; Hasegawa, J.; Ishida, M.; Nakajima, T.; Honda, Y.; Kitao, O.; Nakai, H.; Klene, M.; Li, X. K., J. E.; Hratchian, H. P.; Cross, J. B.; Bakken, V.; Adamo, C.; Jaramillo, J.; Gomperts, R.; Stratmann, R. E.; Yazyev, O.; Austin, A. J.; Cammi, R.; Pomelli, C.; Ochterski, J. W.; Ayala, P. Y.; Morokuma, K.; Voth, G. A.; Salvador, P.; Dannenberg, J. J.; Zakrzewski, V. G.; Dapprich, S.; Daniels, A. D.; Strain, M. C.; Farkas, O.; Malick, D. K.; Rabuck, A. D.; Raghavachari, K.; Foresman, J. B.; Ortiz, J. V.; Cui, Q.; Baboul, A. G.; Clifford, S.; Cioslowski, J.; Stefanov, B. B.; Liu, G.; Liashenko, A.; Piskorz, P.; Komaromi, I.; Martin, R. L.; Fox, D. J.; Keith, T.; Al-Laham, M. A.; Peng, C. Y.; Nanayakkara, A.; Challacombe, M.; Gill, P. M. W.; Johnson, B.; Chen, W.; Wong, M. W.; Gonzalez, C.; Pople, J. A. *Gaussian 03*, D01 ed.; Gaussian Inc., 2004.

(22) M.W.Schmidt; K.K.Baldridge; J.A.Boatz; S.T.Elbert; M.S.Gordon; J.H.Jensen; S.Koseki; N.Matsunaga; K.A.Nguyen; S.J.Su; T.L.Windus; M.Dupuis; J.A.Montgomery. *J. Comput. Chem.* **1993**, *14*, 1347.

(23) *Molekel ver.5.4*; Swiss National Supercomputing Centre.: Manno, Switzerland, 2009.

(24) Andersson, K.; Roos, B. O.; Malmqvist, P. A.; Widmark, P. O. *Chem. Phys. Lett.* **1994**, *230*, 391.

(25) Roos, B. O.; Borin, A. C.; Gagliardi, L. *Angew. Chem. Int. Ed.* **2007**, *46*, 1469.

(26) Kurokawa, Y. I.; Nakao, Y.; Sakaki, S. *J. Phys. Chem. A* **2009**, *113*, 3202.

(27) The moderate discrepancy observed in the quintet spin state would arise from the difference between B3LYP and BP86 functionals.

(28) Frenking, G.; Frohlich, N. *Chem. Rev.* **2000**, *100*, 717.

Appendix

Optimized geometry of $\mathbf{MB_{Cr}}$ by the DFT method (Table A2-1). The metal-metal distance, the spin multiplicity, and the occupation numbers of $\mathbf{B_M}$ (M = V - Fe) (Table A2-2). Energies of $\mathbf{MB_M}$ (M = Sc - Ni) calculated by the DFT method with B3LYP*, BP86, and PW91PW91 functional (Table A2-3). The PES of $\mathbf{MB_{Cr}}$ in the septet spin with EDS=0.02, 0.01, and 0.005 (Figure A2-1). Optimized geometry of $\mathbf{TB_{Cr}}$ (Figure A2-2). Important MOs of $Cr(AIP)_2$ (Figure A2-3). Orbital energies of $\mathbf{M_{Cr}}$ under D_2 symmetry (Figure A2-4). The DFT, CASSCF(10,10), and MRMP2 energies of $\mathbf{MT_{Cr}}$ (Figure A2-5). PES of $\mathbf{MB_{Cr}}$ (Figure A2-6). Optimized geometry of $\mathbf{M_{Cr}}$ at R(Cr-Cr) = 3.4 Å by the CASSCF(10,10) method (Figure A2-7). PES of $\mathbf{MB_V}$ (Figure A2-8). Total energies in singlet to 9tet spin states of $\mathbf{B_V}$ (Figure A2-9). The natural orbitals of $\mathbf{MB_{Mn}}$ (Figure A2-10). Total energies of $\mathbf{B_{Mn}}$ (Figure A2-11). Total energies of $\mathbf{B_{Mn}}$ in the 1let to 11tet states on the 9tet optimized geometry under C2 symmetry (Figure A2-12). The natural orbitals of $\mathbf{B_{Mn}}$ at the optimized geometry in C_2 symmetry (Figure A2-13). Total energies of $\mathbf{MB_{Fe}}$ (Figure A2-14). Total energies of $\mathbf{B_{Fe}}$ (Figure A2-15).

Table A2-2. The metal-metal distance, the spin multiplicity, and the occupation numbers of the real system, $\mathbf{B_M}$ (M = V - Fe)

	$\mathbf{B_V}$	$\mathbf{B_{Cr}}$	$\mathbf{B_{Mn}}$	$\mathbf{B_{Fe}}$
R(M-M) / Å	3.510	3.607	3.828	3.727
Most stable spin state (2S+1)				
DFT(BP86)	5	7	9	7
ONIOM(CASSCF)	5	7	9	7
ONIOM(MRMP2)	5	7	9	1
Occupation Number				
ϕ_3	1.7955	1.6137	1.4563	1.5950
ϕ_4	1.8104	1.5994	1.4730	1.6320
ϕ_5	1.0010	1.0012	1.0000	1.4752
ϕ_6	1.0000	1.0021	1.0001	1.5237
ϕ_7	0.9993	0.9985	1.0013	1.3843
ϕ_8	0.9920	0.9978	0.9991	1.3633
ϕ_9		1.0000	1.0001	1.0022
ϕ_{10}		1.0000	0.9999	0.9988
ϕ_{11}			1.0001	1.0024
ϕ_{12}			0.9999	0.9984
ϕ_{13}	0.2041	0.4014	0.5377	0.4778
ϕ_{14}	0.1976	0.3860	0.5326	0.5469

Table A2-1. Optimized geometry of $\mathbf{MB_{Cr}}$ by the DFT method.[a]

	B3LYP		BP86		PW91PW91		B3LYP*	
	R(Cr-Cr)	D(CA-CA)[b]	R(Cr-Cr)	D(CA-CA)[b]	R(Cr-Cr)	D(CA-CA)[b]	R(Cr-Cr)	D(CA-CA)[b]
11tet	4.524	0.0	4.409	0.0	4.382	0.0	4.497	0.0
9tet	4.080	87.9	4.011	85.6	3.983	85.6	4.062	87.4
7tet	3.634	55.0	3.522	49.4	3.505	50.8	3.601	52.9
5tet	3.552	65.0	3.461	64.3	3.442	64.7	3.555	3.2
3let	3.387	85.3	3.349	80.1	3.328	80.5	3.376	69.9
1let	3.338	87.0	3.291	87.1	3.273	87.3	3.327	87.0
exp.(Tol)[c]	3.603	54.0	3.603	54.0	3.603	54.0	3.603	54.0
exp.(Bz)[d]	3.515		3.515		3.515		3.515	

a:Length in Å and angle in degree.

b: the dihedral angle between two Cr(AIP) lignds

c: Tsai, Y.-C.; Wang, P.-Y.; Chen, S.-A.; Chen, J.-M. *J. Am. Chem. Soc.* **2007**, *129*, 8066

d: Monillas, W. H.; Yap, G. P. A.; Theopold, K. H. *Angew. Chem. Int. Ed. Eng.* **2007**, *46*, 6692.

Table A2-3. Energies of $\mathbf{MB_M}$ (M = Sc - Ni) calculated by the DFT method with B3LYP*, BP86, and PW91PW91 functional. Relative energies from the most stable spin state are shown in kcal/mol.

		Sc	Ti	V	Cr	Mn	Fe	Co	Ni
B3LYP*	11tet					11.6			
	9tet				26.9	0.0	23.9		148.42
	7tet			33.1	0.0	40.8	0.0	20.2	71.32
	5tet		19.8	0.0	43.2	23.2	10.6	0.0	28.58
	3let	27.5	0.0	16.4	27.3	46.5	5.2	36.9	0.00
	1let	0.0	19.7	58.8	37.6	44.1	35.2	28.9	33.66
		Sc	Ti	V	Cr	Mn	Fe	Co	Ni
BP86	11tet					20.3			
	9tet				32.8	0.0	42.7		
	7tet			32.0	0.0	10.2	15.9	28.6	72.73
	5tet		21.6	0.0	12.5	0.2	10.9	0.0	24.45
	3let	27.0	0.00	8.8	15.9	6.1	0.0	9.1	0.00
	1let	0.0	6.4		19.0	3.6	11.5	10.3	8.90
		Sc	Ti	V	Cr	Mn	Fe	Co	Ni
PW91	9tet				33.0	0.0	41.1		
	7tet			32.4	0.0	11.6	15.2	28.9	72.51
	5tet		22.1	0.0	13.4	2.8	10.6	0.0	24.55
	3let	27.6	0.0	9.2	17.8	9.3	0.0	9.3	0.00
	1let	0.0	5.4		20.9	7.1	12.	10.5	8.85

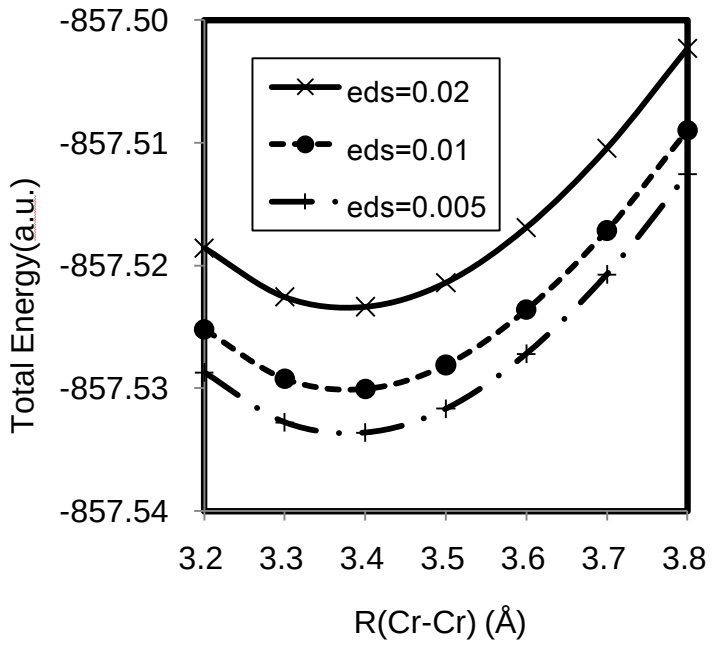

Figure A2-1. Effect of energy denominator shift (EDS) vales on the PES of $\mathbf{MB_{Cr}}$ in the septet spin state calculated by the MRMP2 method [a] The equilibrium distances are 3.3749, 3.3831, and 3.3850 Å at EDS=0.02, 0.01, and 0.005, respectively.

[a] The B3LYP-optimized geometry was employed

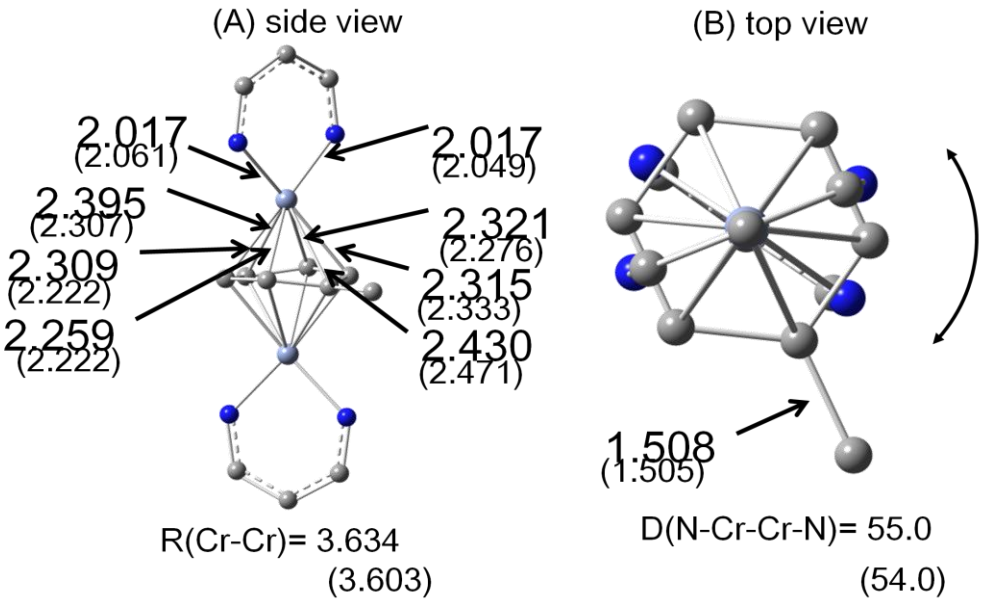

Figure A2-2. Optimized geometry of **TB_{Cr}** by the DFT(B3LYP) method in septet state under C_1 symmetry. Parentheses represent experimental values. Length in Å and angle in degree.

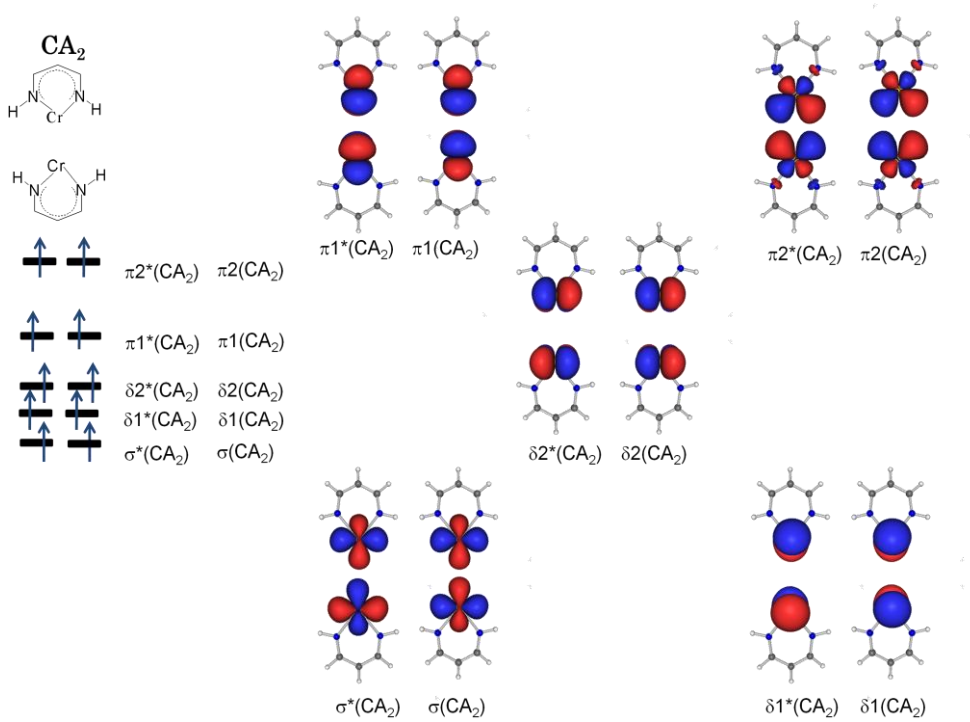

Figure A2-3. Important MOs of $Cr(AIP)_2$, **CA_2**

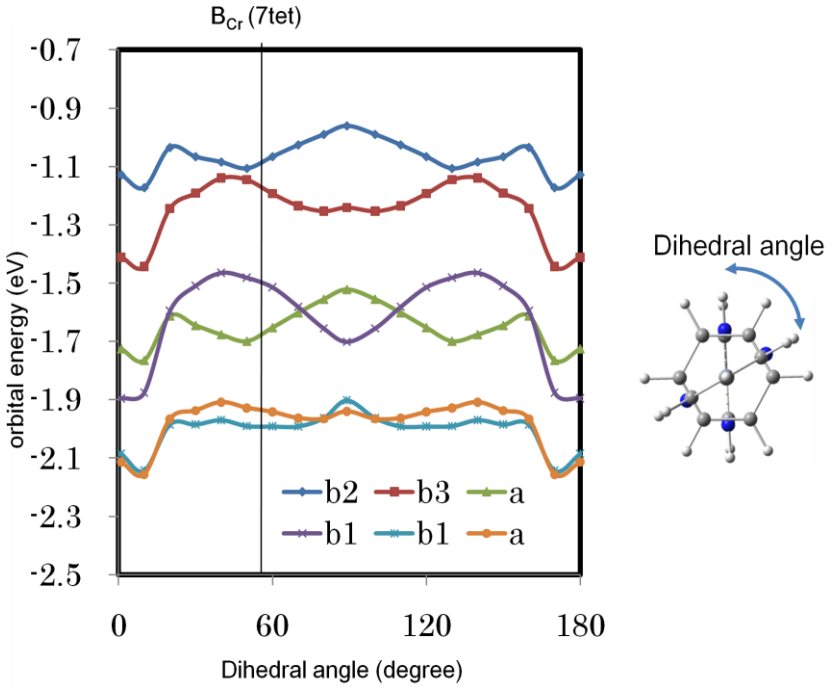

Figure A2-4. Orbital energies of $\mathbf{M_{Cr}}$ under D_2 symmetry by the RO-B3LYP method in the septet spin state. R(Cr-Cr) is fixed to be the experimental value (3.634Å).
When the dihedral angle changes, the orbital energies change a little, and the order of orbital energies interchange. However, the electron configuration does not change at all.

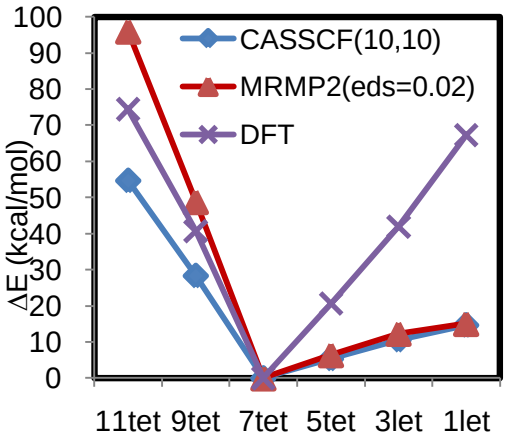

Figure A2-5. Energies of $\mathbf{MT_{Cr}}$ relative to the energy of the septet spin state.[a]
[a] The DFT(B3LYP)-optimized geometry in the septet spin state was employed in the CASSCF and MRMP2 calculations.

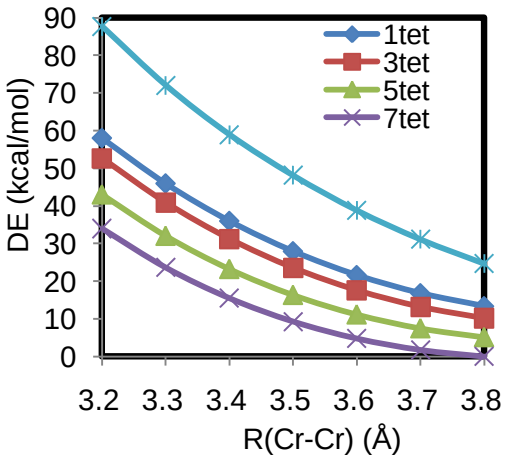

Figure A2-6. PES of $\mathbf{MB_{Cr}}$ by the CASSCF(10,10) method.

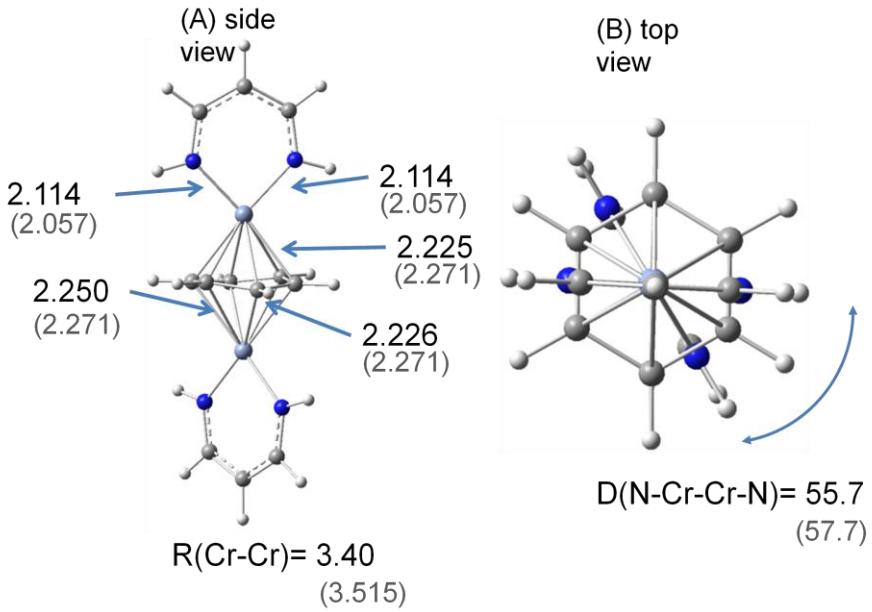

Figure A2-7. Optimized geometry of $\mathbf{MB_{Cr}}$ at R(Cr-Cr) = 3.4 Å by the CASSCF(10,10) method in septet state under D_2 symmetry. Parentheses represent experimental values. Length in Å and angle in degree.

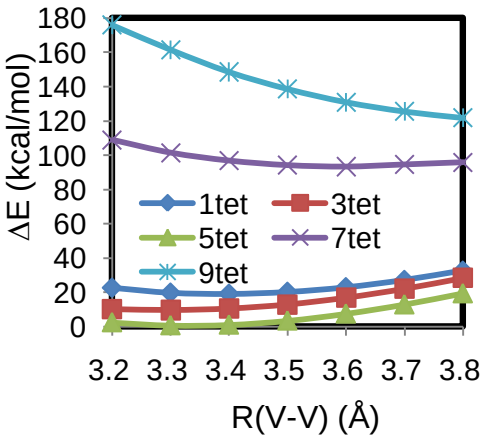

Figure A2-8. PES of $\mathbf{MB_V}$ by the MRMP2 method using the CASSCF(8,8)- optimized geometries in 1let to 9tet spin states ..

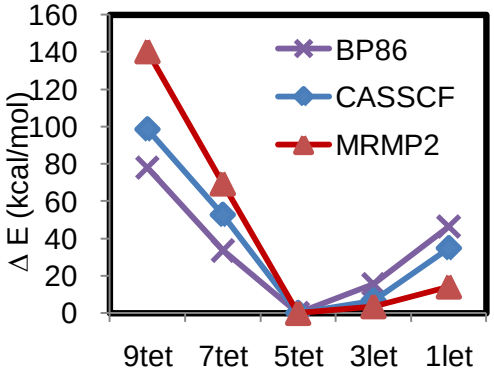

Figure A2-9. Energies (in kcal/mol) of $\mathbf{B_V}$ relative to the energy of the quintet spin state[a]

[a] The DFT(BP86)-optimized geometry in the quintet spin state was employed in the CASSCF and MRMP2 calculations.

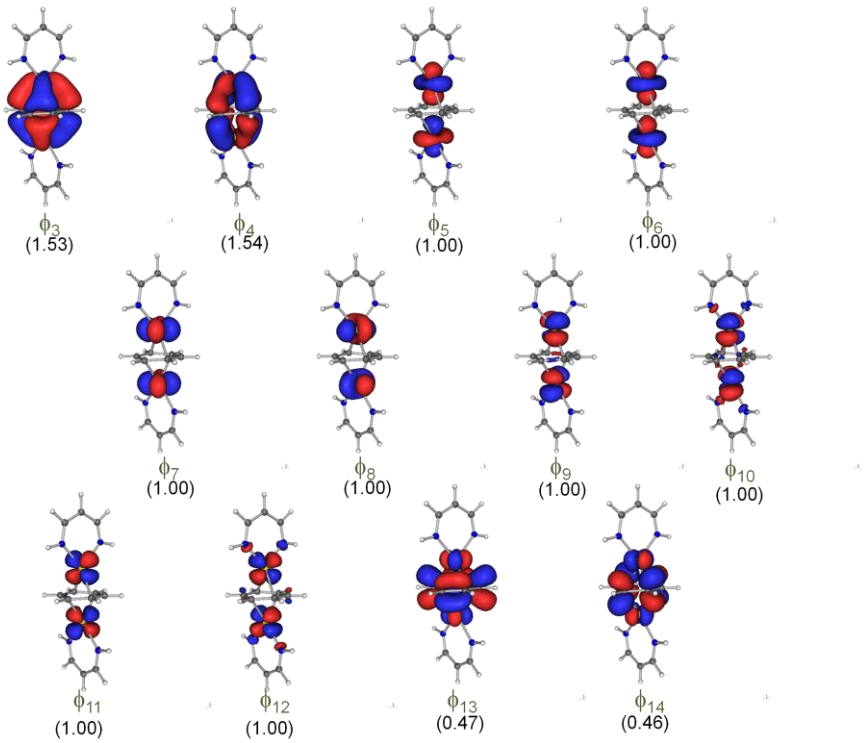

Figure A2-10. The natural orbitals of **MB$_{Mn}$** at R(Mn-Mn) = 3.50 Å optimized with the CASSCF(12,12) method in D_2 symmetry. Numbers in parentheses represents the occupation numbers.

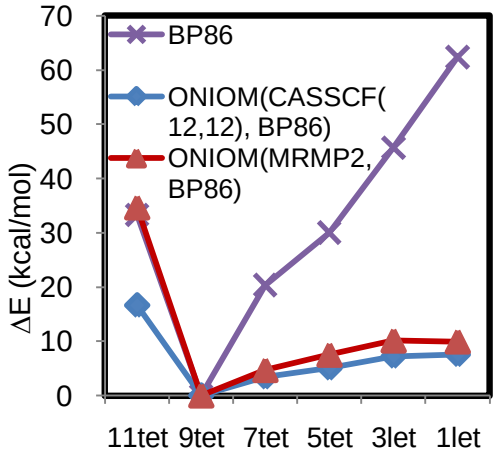

Figure A2-11. Energies (in kcal/mol) of **B$_{Mn}$** relative to the energy of the nonet spin state[a]

[a] The DFT(BP86)-optimized geometry in the nonet spin state under D_2 symmetry was employed in the CASSCF and MRMP2 calculations.

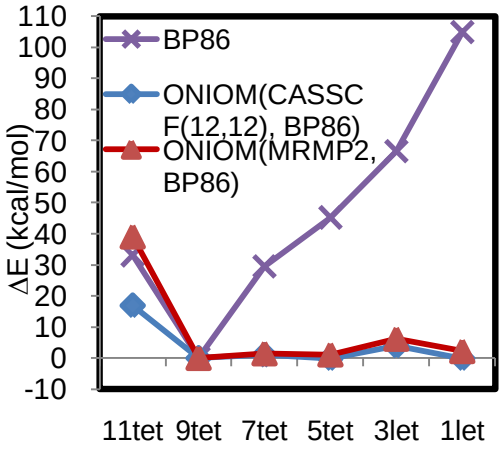

Figure A2-12. Energies (in kcal/mol) of **B$_{Mn}$** relative to the energy of the nonet spin state[a]

[a] The DFT(BP86)-optimized geometry in the nonet spin state under C_2 symmetry was employed in the CASSCF and MRMP2 calculations.

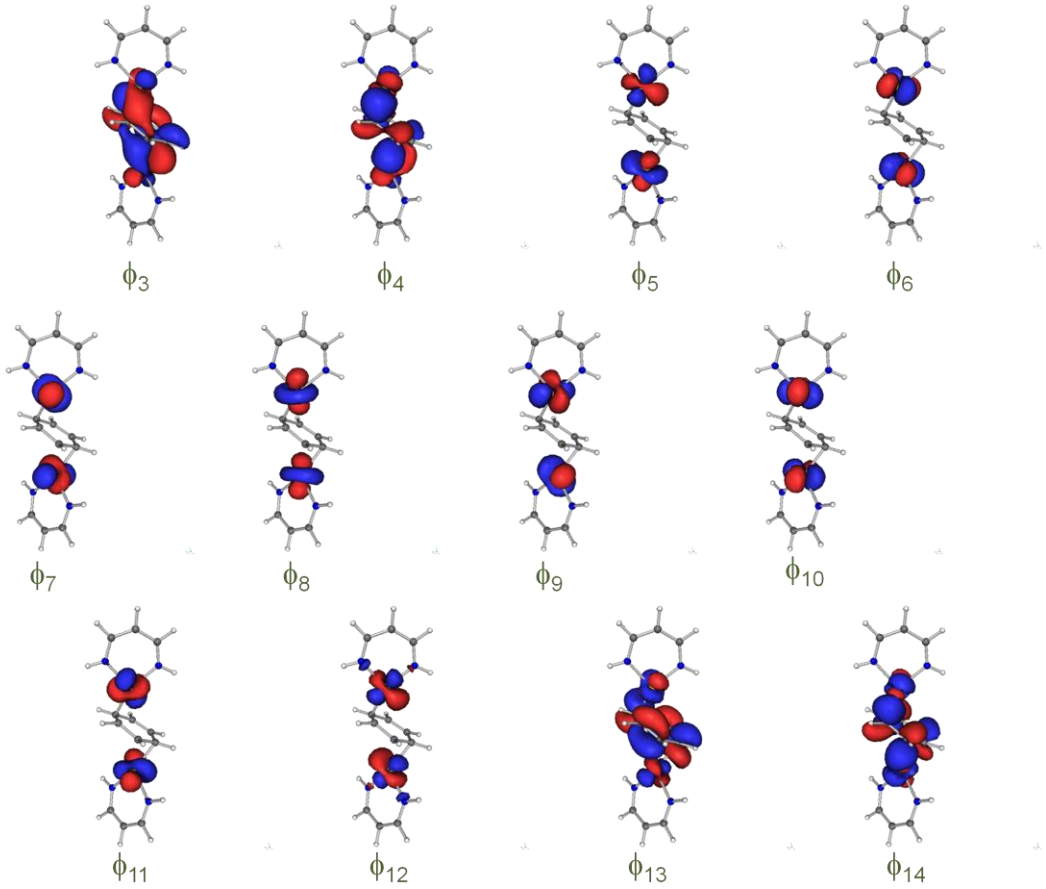

Figure A2-13. The natural orbitals of $\mathbf{B_{Mn}}$ in the DFT(BP86)-optimized geometry under C_2 symmetry. Only the model part is shown.

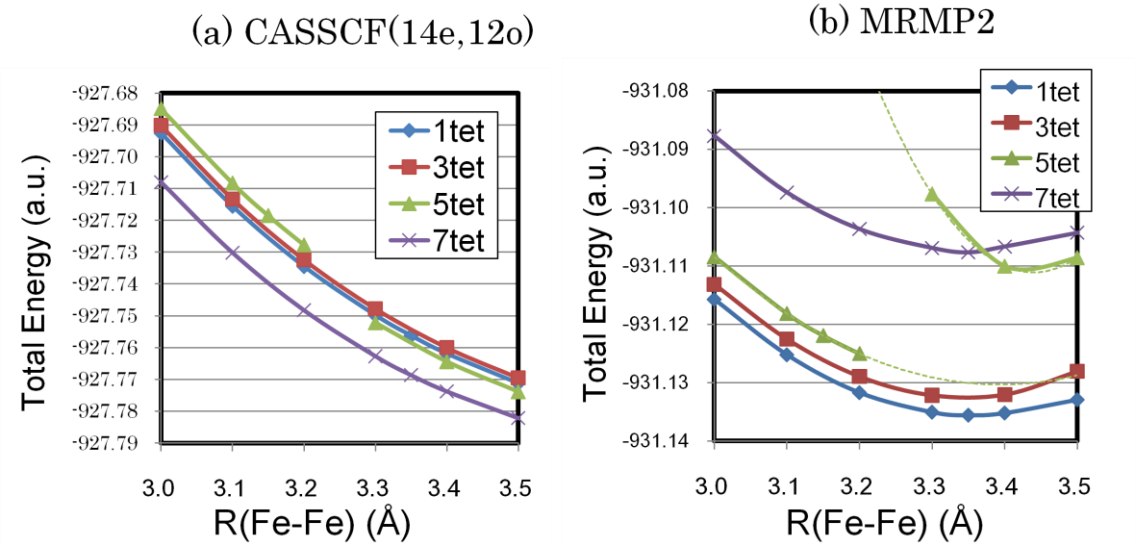

Figure A2-14. Total energies of $\mathbf{MB_{Fe}}$ by the (a) CASSCF(14e,12o) and (b) MRMP2[a] method on the CASSCF(14e,12o)-optimized geometries

[a] The broken lines in the PES by the MRMP2 method represent the extrapolated quadratic curves. Those two states do not cross each other in the MRMP2 level at least in this region.

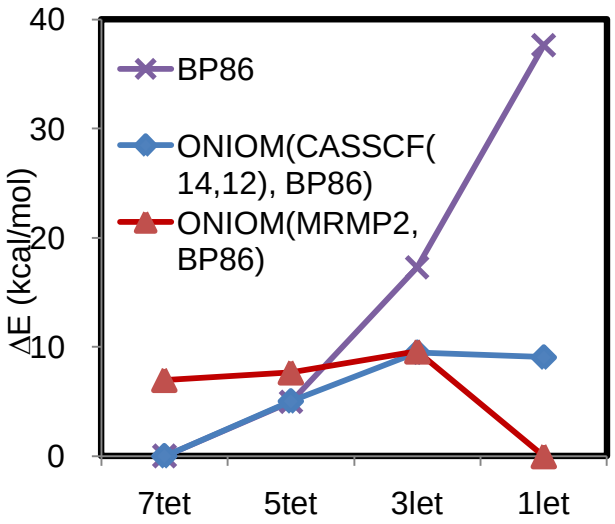

Figure A2-15. Energies (in kcal/mol) of $\mathbf{B_{Fe}}$ relative to the energy of the septet spin state for BP86 and the ONIOM(CASSCF(14e,12o),BP86) calculations and singlet spin state for the ONIOM(MRMP2,BP86) calculation[a]

[a] The DFT(BP86)-optimized geometry in the septet spin state was employed in the CASSCF and MRMP2 calculations..

Chapter 3
Inverted Sandwich Type Complexes of Second Row-Transition Metal Elements: Theoretical Prediction of Electronic Structure and Spin Multiplicities

1. Introduction:

Recently, Tsai *et al.*[1] and Monillas *et al.*[2] synthesized inverted sandwich type complex (ISTC) of chromium, $(\mu\text{-}\eta^6\text{:}\eta^6\text{-}C_6H_5CH_3)[Cr(DDP)]_2$ (DDPH = 2-{(2,6-diisopropylphenyl)amino}-4-{(2,6-diisopropylphenyl)imino}pent-2-ene, which is often referred to "nacnac") and $(\mu\text{-}\eta^6\text{:}\eta^6\text{-}C_6H_6)[Cr(DDP)]_2$ $\mathbf{R_{Cr}}$, respectively. Interestingly, they take very high spin state of septet. Also, Tsai *et al.* reported that ISTC of vanadium, $(\mu\text{-}\eta^6\text{:}\eta^6\text{-}C_6H_5CH_3)[V(DDP)]_2$, takes very high spin state of quintet.[3] These are surprisingly high spin state, considering that organometallic compounds tend to take in general low spin state.

Electronic structures of these ISTCs are of considerable interest from the point of view of physical chemistry, coordination chemistry, and material science. Previously, we theoretically studied ISTCs of the first-row transition metals (TMs) and clarified the reason why ISTCs of vanadium and chromium take such high spin states.[4] Also we calculated the

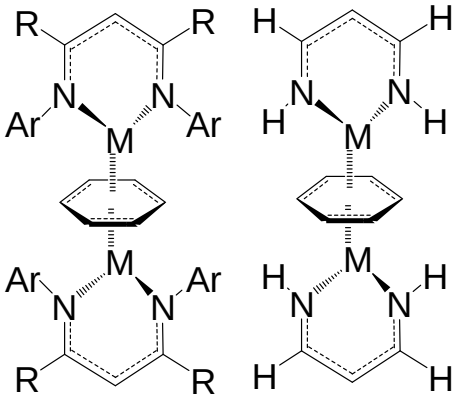

$\mathbf{R}_{M}$ $\mathbf{M}_{M}$

Ar = 2,6-$^{i}Pr_2C_6H_3$, R = Me

Scheme 3-1. $(\mu\text{-}\eta^6\text{:}\eta^6\text{-}C_6H_6)(MDDP)_2$ ($\mathbf{R}_{M}$) and $(\mu\text{-}\eta^6\text{:}\eta^6\text{-}C_6H_6)(MAIP)_2$ ($\mathbf{M}_{M}$), (M = Y - Tc, DDPH = 2-{4-{(2,6-diisopropyllhenyl)imino}pent-2-ene, AIPH = (*Z*)-1-amino-3-imino-prop-1-ene)

spin states of their analogues, $\mathbf{R}_{M}$ (*M* = Sc, Ti, Mn, and Fe), though they have not been synthesized yet, and reported that they take closed-shell singlet, triplet, nonet, and open-shell singlet spin states, respectively. Thus, the spin multiplicity of the $\mathbf{R}_{M}$ (*M* = the first-row TMs) increases from singlet to nonet when going to the right-hand side from the left-hand side in the periodic table, and then suddenly decreases to single at Fe.

In the present work, we theoretically investigated various ISTCs of the second-row transition metals, $\mathbf{R}_{M}$ (*M* = Y, Zr, Nb, Mo, and Tc). Our main purposes here are to clarify the electronic structures of the ISTCs of the second-row TMs, to present theoretical prediction of their spin multiplicities, and to clarify the reason why the spin multiplicity is different between the first and the second TM series.

2. Models and Computational Details

2-1 Model Complexes

In our previous study of the ISTC of the first-row TMs,[4] we employed AIP (AIPH = 1-amino-3-imono-prop-1-ene) ligand (see Scheme 3-1) as a model of the DDP. The theoretical calculations reproduced the spin multiplicities of model complexes $\mathbf{R}_{V}$ and $\mathbf{R}_{Cr}$, indicating that the AIP ligand is a good model of DDP. Actually, the substituents of the ligand induce little effect on the geometry and the relative stabilities of spin multiplicities. Though toluene was employed for real systems, substitution of toluene for benzene did not change the most stable spin multiplicity.[4] For these results, we mainly employed models, $(\mu\text{-}\eta^6\text{:}\eta^6\text{-}C_6H_6)[M(AIP)]_2$ $\mathbf{M}_{M}$, in the present study unless otherwise mentioned.

2-2 Computational Details

The geometries of $\mathbf{M}_{M}$ (*M* = Y, Zr, Nb, Mo, and Tc) were optimized in each spin state by the DFT method with B3LYP,[5,6] B3LYP*,[7] BP86,[5,8] and PW91PW91[9] functionals. The initial geometries of $\mathbf{M}_{M}$ were set to D_2 symmetry,[10] where *M*(AIP) moieties were fixed to be planar because the six-membered ring of the Cr(DDP) moiety in $(\mu\text{-}\eta^6\text{:}\eta^6\text{-}C_6H_5CH_3)[Cr(DDP)]_2$ was experimentally observed to be almost planar.[1-3]

The geometry of $\mathbf{M}_{Mo}$ was optimized by the CASSCF(10e, 8o) method,[11] too, where the Mo-Mo distance was taken as a coordinate and the geometry of the remaining moiety was

optimized under D_2 symmetry at various Mo-Mo distances. Using the CASSCF-optimized geometry at each Mo-Mo distance, the potential energy surface (PES) was evaluated by the MRMP2 method.[12-14] In the MRMP2 calculations, CASSCF(10e, 8o) wavefunction was taken to be the reference wavefunction. We introduced the energy denominator shift (EDS) in the MRMP2 calculations, where the EDS value of 0.02 a.u. was employed throughout the present study.

Core electrons (up to 3p) of the metals were replaced with Stuttgart-Dresden-Born effective core potentials (ECPs), and their valence electrons were represented with (311111/22111/411) basis sets.[15] For C, N, and H, cc-pVDZ basis sets were employed.[16] The augmented functions were added to N because it is anionic in the AIP.

Gaussian 03 package was used for DFT calculation[17] and GAMESS package was used for CASSCF and MRMP2 calculations.[18] Molecular orbitals were drawn with Molekel program ver. 5.3.[19]

3. Results and Discussion

3.1 DFT-Computed Spin Multiplicities and Geometries of $\mathbf{M}_M$ (M = Y, Zr, Nb, Mo, and Tc)

We optimized the geometry of $\mathbf{M}_M$ (M = Y, Zr, Nb, Mo, and Tc) in various spin states with the B3LYP functional. The most stable spin state is singlet, triplet, quintet, and singlet for M = Y, Zr, Nb, and Tc, respectively, as shown in Table 3-1. In $\mathbf{M_{Mo}}$, the most stable spin state is triplet, but it is only 0.9 kcal/mol higher in energy than the singlet spin state.

The Y-Y distance is 4.082 Å at the optimized geometry. When going to Tc from Y in the second-row TM series, the *M*-*M* distance gradually decreases by about 0.12 Å, as shown Figure 3-1. It is likely that this decrease arises from the decrease in d orbital size when

Table 3-1. Relative energies[a] of various spin multiplicities calculated by the DFT (B3LYP) method

	Y	Zr	Nb	Mo	Tc
7tet		44.1	51.5	21.0	
5tet	51.5	17.4	**0.0**	19.8	21.6
3let	26.9	**0.0**	13.4	**0.0**	1.2
1let	**0.0**	0.8	32.5	0.9	**0.0**

[a] Energy difference from the most stable spin state are shown in kcal/mol.

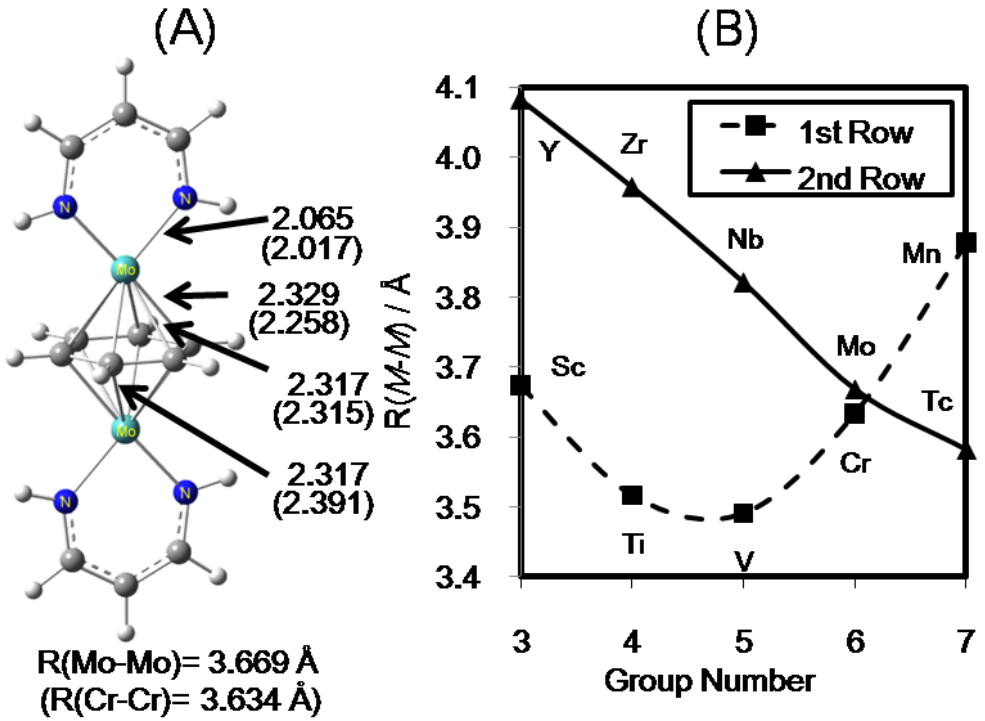

Figure. 3-1 DFT-optimized geometry of $\mathbf{M}_{M}$ in the most stable spin state.[a] (A) Important distances (Å) of $\mathbf{M}_{\mathbf{Mo}}$ and $\mathbf{M}_{\mathbf{Cr}}$ in parentheses (B) Metal-Metal distances of $\mathbf{M}_{M}$.
a: The most stable spin states are 1let, 3let, 5tet, 3tet, and 1let for *M* = Y, Zr, Nb, Mo, and Tc, and 1let, 3let, 5tet, 7tet, and 9net for *M* = Sc, Ti, V, Cr, and Mn, respectively.

going to right hand side in the periodic table.[20] In the first row TMs, the *M*-*M* distance decreases when going from Sc to V like the second row TMs, but increases when going from V to Mn. This increase is interrupted as follows: Electrons occupy the π1 and π1* orbitals when *M* = Cr and π1 to π2* orbitals when *M* = Mn. Because the lobes of these π orbitals are pointing to the benzene, the repulsion between the AIP ligand and benzene increases as these π orbitals are occupied, which leads to larger *M*-*M* distance. This is the reason why the *M*-*M* distance increases when going from V to Mn. The difference in *M*-*M* distance between the first (Sc to V) and second row (Y to Nb) TMs is also interpreted by the difference in d orbitals radius:[20] The 3d orbitals of the first row TMs always less expands than the 4d orbital of the second row TMs.

We also calculated these complexes with the B3LYP*, BP86, and PW91PW91 functionals. The most stable spin state of $\mathbf{M}_{M}$ (*M* = Y, Zr, Nb, and Tc) is the same as that calculated with the B3LYPfunctional. However, that of $\mathbf{M}_{\mathbf{Mo}}$ is calculated to be singlet by these functionals, as shown in Table A3-1, unlike the B3LYP computational result. Because

the B3LYP functional tends to overestimate the stability of higher spin multiplicity, as well known,[21] we will investigate the $\mathbf{M_{Mo}}$ with the CASSCF and MRMP2 methods in section 3.4 in more detail.

3.2 Orbital Diagrams of and Spin Multiplicities of $\mathbf{M}_M$ (*M* = Y, Zr, and Nb)

In this section, we wish to briefly discuss the molecular orbital (MO) interaction diagram to understand the electronic structure and spin state of $\mathbf{M}_M$.

In the *M*(AIP), degenerate five d orbitals of *M* are split into non-degenerate five orbitals by the interaction with the AIP moiety, as discussed previously.[4] We named them σ_d, δ_{d1}, δ_{d2}, π_{d1}, and π_{d2} orbitals, as shown in Scheme 3-2. The π_{d2} orbital mainly consists of the d_{xz} orbital of *M* with which the N lone pair of the AIP moiety interacts in an anti-bonding way. Because these two orbitals overlap well with each other in a σ manner with respect to the *M*-N bond, the π_{d2} orbital is much destabilized in energy. The π_{d1} orbital mainly consists of the d_{yz} orbital of *M* with which the π orbital of the AIP moiety interacts in an anti-bonding way. Because of the π-type overlap between these orbitals with respect to the *M*-N bond, the π_{d1} orbital is less destabilized than the π_{d2} orbital. However, this π_{d1} orbital is more destabilized in the second-row TM complexes than that of the first-row TM complexes because the d orbital more expands in the second-row TM element than in the first-row TM element.[20] The δ_{d2} and δ_{d1} orbitals mainly consist of the d_{xy} and d_{x2-y2} orbitals, respectively. The destabilization of the δ_{d2} orbital is somewhat larger than that of the δ_{d1} orbital because the d_{x2-y2} orbital stronger interacts with the π orbital of the AIP ligand than the d_{xy} orbital. Thus, the energy gap is large between π_{d1} and π_{d2} but small between δ_{d2} and δ_{d1} orbitals in the *M*(AIP) moiety. The σ_d orbital lies at the lowest energy because it little interacts with the AIP ligand.

[*M*(AIP)]$_2$ consists of two *M*(AIP) moieties, where d-derived orbitals of *M*(AIP), π_{d2}, π_{d1}, δ_{d1}, δ_{d2}, and σ_d, form bonding and anti-bonding pairs such as $\pi2$ and $\pi2^*$, $\pi1$ and $\pi1^*$, $\delta2$ and $\delta2^*$, $\delta1$ and $\delta1^*$, and σ and σ^* orbitals, respectively, as shown in Scheme 3-2. Because two *M*(AIP) moieties are considerably separated by benzene, the bonding orbital and its anti-bonding counterpart completely degenerate with each other.

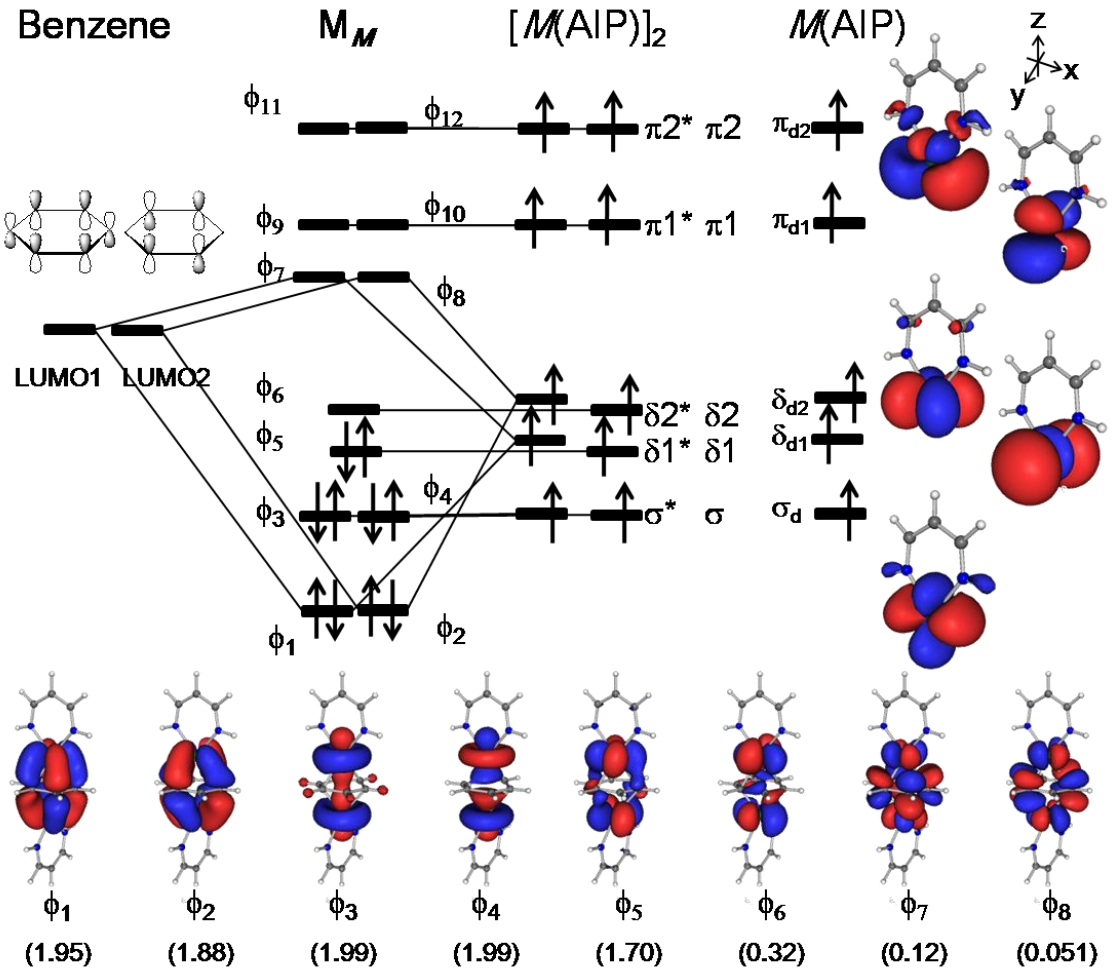

Scheme 3-2. MO diagram of (μ-η^6:η^6-C_6H_6)[*M*(AIP)]$_2$ (**M**$_M$), [*M*(AIP)]$_2$, and *M*(AIP), and the natural orbitals of **M**$_{Mo}$ calculated by the CASSCF(10e,8o) method at R(Mo-Mo) = 3.6 Å in the ^{1}A state. The numbers in parentheses represent the occupation numbers of the natural orbitals.[a]

a: We present the occupation numbers of the natural orbitals here, since the natural orbital resembles well the CASSCF-optimized MO.

In **M**$_M$, only δ1* and δ2* orbitals of [*M*(AIP)]$_2$ can strongly interact with the LUMOs of benzene to form bonding MOs, ϕ1 and ϕ2, and anti-bonding orbitals, ϕ7 and ϕ8, as discussed previously.[4] The other orbitals of [*M*(AIP)]$_2$ do not interact with the HOMOs of benzene because π2, π1, δ2, δ1, σ and σ* orbitals have different symmetry from those of the π orbitals of benzene and also the π2* and π1* orbitals are at much higher energy than the HOMOs of benzene. Thus, these MOs of **M**$_M$ exist at almost the same energy as those of the *M*(AIP) moiety. We named all these MOs ϕ1 to ϕ12 orbitals, as shown in Scheme 3-2.

Because Y(I) has two d electrons, totally four d electrons occupy these MOs. The

possible electron configuration of $\mathbf{M_Y}$ is $(\phi1)^2(\phi2)^2$, because the $\phi1$ and $\phi2$ MOs exist at considerably lower energy than the others. Thus, it is clearly concluded that $\mathbf{M_Y}$ takes the singlet spin state.

Two more d electrons are involved in $\mathbf{M_{Zr}}$. The $\phi3$ and $\phi4$ MOs are nearly degenerate, because they consist of the d_{z2} orbitals which little interact with benzene HOMOs and LUMOs. Thus, $\mathbf{M_{Zr}}$ takes $(\phi1)^2(\phi2)^2(\phi3)^1(\phi4)^1$ electron configuration, which is the triplet spin state.

Two more d electrons are added in $\mathbf{M_{Nb}}$. Similarly, the $\phi5$ and $\phi6$ MOs are nearly degenerate. Also, they exist at similar energy to the $\phi3$ and $\phi4$ MOs, because the d_δ orbitals of Nb little interact with HOMOs and LUMOs of benzene. As a result, $\mathbf{M_{Nb}}$ takes a $(\phi1)^2(\phi2)^2(\phi3)^1(\phi4)^1(\phi5)^1(\phi6)^1$ electron configuration, corresponding to the quintet spin state.

These spin multiplicities are the same as those of the ISTCs of the first-row TM complexes.

3.3 Spin Multiplicities of $\mathbf{M_{Mo}}$ and $\mathbf{M_{Tc}}$ by the MRMP2 Method

Though the spin multiplicity can be easily understood in terms of orbital diagrams for *M* = Y to Nb, the electronic state becomes complicated when *M* = Mo, as follows: There are 10 d electrons in $\mathbf{M_{Mo}}$. Thus, the possible electron configurations of $\mathbf{M_{Mo}}$ are $(\phi1)^2(\phi2)^2(\phi3)^2(\phi4)^2(\phi5)^2$ and $(\phi1)^2(\phi2)^2(\phi3)^2(\phi4)^2(\phi5)^1(\phi6)^1$, which provide singlet and triplet spin states, respectively. If the energy gap between δ_{d1} and δ_{d2} is small, the triplet state is more stable. If not, the singlet state is more stable. This means that we should make careful examination of $\mathbf{M_{Mo}}$.

Actually, the spin multiplicity of $\mathbf{M_{Mo}}$ depends on the functionals employed, as expected above; see Tables 3-1 and A3-1. We investigated $\mathbf{M_{Mo}}$ in more detail with the MRMP2 method. In the CASSCF calculations, we employed an active space consisting of 10 electrons in such 8 MOs as $\phi1$ to $\phi8$, because these MOs are in similar energies.[22] The energy minimum of $\mathbf{M_{Mo}}$ is presented at R(Mo-Mo) = 3.6 Å in the ^{1}A state, as shown in Figure 3-2. The main electron configuration and second leading one are $(\phi1)^2(\phi2)^2(\phi3)^2(\phi4)^2(\phi5)^2$ and $(\phi1)^2(\phi2)^2(\phi3)^2(\phi4)^2(\phi6)^2$, where weights are 0.766 and 0.095, respectively. The weights of the other electron configurations are less than 0.04. The

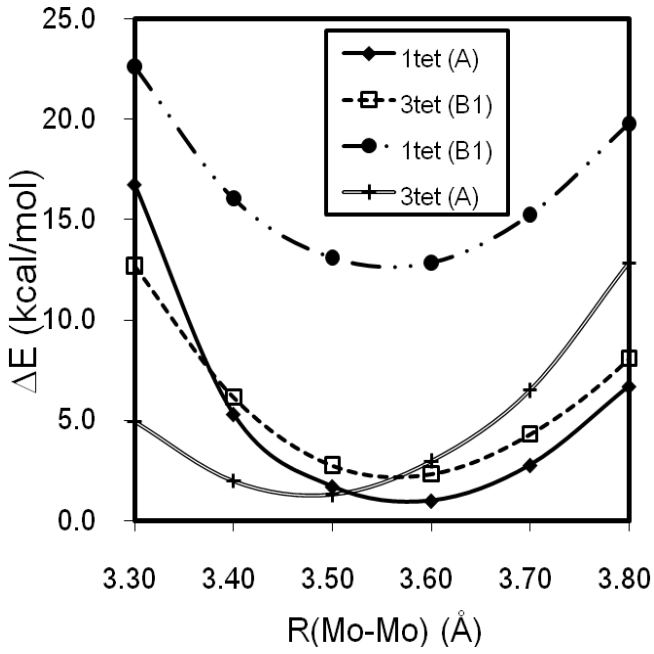

Figure 3-2. The PES of $\mathbf{M_{MO}}$ calculated by the MRMP2 method.

occupation numbers calculated by the CASSCF method are given in Scheme 3-2: Those of ϕ1 to ϕ5 are approximately two and those of the others are approximately zero. Thus, these results suggest that the ground state of $\mathbf{M_{Mo}}$ takes closed shell singlet electron configuration. However, the second and third lowest states of $\mathbf{M_{Mo}}$, which are $^3B_1$ electronic state at R(Mo-Mo) = 3.6 Å and ^3A state at R(Mo-Mo) = 3.5 Å, respectively, lie within 1.5 kcal/mol from the ^1A state. The main, second, and third leading configurations of the $^3B_1$ state are $(\phi1)^2(\phi2)^2(\phi3)^2(\phi4)^2(\phi5)^1(\phi6)^1$, $(\phi1)^2(\phi2)^2(\phi3)^1(\phi4)^2(\phi5)^1(\phi6)^1(\phi8)^1$, and $(\phi1)^2(\phi2)^2(\phi3)^2(\phi4)^1(\phi5)^1(\phi6)^1(\phi7)^1$ where weights are 0.815, 0.039, and 0.030, respectively, at R(Mo-Mo) = 3.6 Å. Those of the ^3A state are $(\phi1)^1(\phi2)^2(\phi3)^2(\phi4)^2(\phi5)^2(\phi6)^1$, $(\phi1)^2(\phi2)^1(\phi3)^2(\phi4)^1(\phi5)^2(\phi6)^1(\phi8)^1$, and $(\phi1)^2(\phi2)^2(\phi3)^2(\phi4)^2(\phi5)^1(\phi6)^1$, where weights are 0.744, 0.037, and 0.031, respectively, at R(Mo-Mo) = 3.5 Å The weights of the other configurations are less than 0.03 in both the $^3B_1$ and ^3A states.

Because the most stable spin state of $\mathbf{M_{Mo}}$ is closed-shell singlet but the triplet states lie energetically very near, it is likely that two states exist in thermal equilibrium according to the Boltzmann distribution. This suggests that the magnetic moment of $\mathbf{M_{Mo}}$ does not provide clear information about the spin multiplicity and depends on the temperature.

In $\mathbf{M_{Tc}}$, the closed-shell singlet is the most stable. Though the triplet spin state is

slightly (1.2 kcal/mol) above the singlet spin state in the B3LYP calculation, B3LYP*, BP86, and PW91PW91 calculations present that the triplet spin states is more than 10 kcal/mol above the singlet spin state. This difference between the B3LYP and the other functionals probably arises because that the B3LYP functional tends to overestimate the stability of highe r spin multiplicity.[21]

3.6 Why Do Mo and Tc Analogues Take Low Spin States?

It is worth investigating the reason why $\mathbf{M_{Mo}}$ takes low spin state unlike $\mathbf{M_{Cr}}$ which takes the septet spin state. Since the energy gap between the ϕ6 and ϕ9 orbitals are much larger in $\mathbf{M_{Mo}}$ than in $\mathbf{M_{Cr}}$, as shown in Scheme 3-2, the two electrons occupy ϕ3 and ϕ4 MOs in $\mathbf{M_{Mo}}$ unlike in $\mathbf{M_{Cr}}$ in which they occupy the ϕ9 and ϕ10 MOs . The energy gap between the ϕ6 and ϕ9 MOs of $\mathbf{M_{Mo}}$ arises from the energy gap between the π_{d1} and δ_{d2} orbitals in the Mo(AIP) moiety, as mentioned above. This energy gap in the Mo(AIP) moiety is considerably larger than in Cr(AIP) moiety, because the 4d orbital more expands than the 3d orbital, leading to larger energy gap between the ϕ6 and ϕ9 orbitals in the ISTCs of the second-row TMs than in those of the first-row TMs; see figure A3-2 for the orbital energies of ϕ3 to ϕ10. As a result, $\mathbf{M_{Mo}}$ does not take high spin state unlike $\mathbf{M_{Cr}}$.

The same discussion is applied to the ISTC of Tc. Because two more electrons are added to $\mathbf{M_{Mo}}$, the singlet electron configuration of $(\phi1)^2(\phi2)^2(\phi3)^2(\phi4)^2(\phi5)^2(\phi6)^2$ is the ground state of $\mathbf{M_{Tc}}$. Because the energy gap between π_{d1} and δ_{d2} orbitals is very large, as discussed above, the other electron configurations are expected to be very unstable. Thus, $\mathbf{M_{Tc}}$ takes closed-shell singlet spin state.

4. Conclusion

We theoretically investigated the ISTCs, (μ-η^6:η^6-C_6H_6) [*M*(AIP)]$_2$ $\mathbf{M_M}$ (AIPH = (Z)-1-amino-3-imino-prop-1-ene) (*M* = Y, Zr, Nb, Mo, and Tc). The DFT calculations with B3LYP, B3LYP*, BP86, and PW91PW91 functionals suggest that the most stable spin states of $\mathbf{M_M}$ are singlet, triplet, quintet, and singlet for *M* = Y, Zr, Nb, and Tc, respectively. These results are understood by the MO diagram. However, that of $\mathbf{M_{Mo}}$ is calculated to be triplet by the B3LYP functional but singlet by the other functionals. The MRMP2 method indicates

that the singlet and triplet spin states lie energetically very near (within 1.5 kcal/mol). The reason why $\mathbf{M_{Mo}}$ and $\mathbf{M_{Tc}}$ take low spin states can be explained by the MO diagram: The energy gap between the ϕ6 and ϕ9 orbitals is too large to overcome the exchange energy.

In conclusion, the ISTCs of the second-row TMs take the same spin multiplicity as those of the first-row TMs for *M* = Y to Nb. However, the ISTCs of the second-row TMs take lower spin state than those of the first-row TMs for *M* = Mo and Tc; the maximum spin multiplicity of ISTCs of the second-rwo TMs is quintet, which is presented by the group 5 metal complex (Nb) unlike that of the first-row TMs. The larger d orbital expansion is the reason why the ISTCs of MO and Tc take low spin state.

Acknowledgements:

This research was supported in part by the Grant-in-Aids on Priority Area "Molecular Theory for Real Systems" (No. 461) and Global COE Program "International Center for Integrated Research and Advanced Education in Materials Science" (No. B-09) of the Ministry of Education, Culture, Sports, Science and Technology (MEXT) of Japan and the Japan Society for the Promotion of Science. Some of theoretical calculations were performed in Institute for Molecular Science (Okazaki, Japan).

Reference and Notes:

(1) Tsai, Y.-C.; Wang, P.-Y.; Chen, S.-A.; Chen, J.-M. *J. Am. Chem. Soc.* **2007**, *129*, 8066.

(2) Monillas, W. H.; Yap, G. P. A.; Theopold, K. H. *Angew. Chem. Int. Ed. Eng.* **2007**, *46*, 6692.

(3) Tsai, Y.-C.; Wang, P.-Y.; Lin, K.-M.; Chen, S.-A.; Chen, J.-M. *Chem. Comm.* **2008**, 205.

(4) Kurokawa, Y. I.; Nakao, Y.; Sakaki, S. *J. Phys. Chem. A* **2009**, in Press.

(5) Becke, A. D. *J. Chem. Phys.* **1993**, *98*, 5648.

(6) Lee, C.; Yang, W.; Parr, R. G. *Phys. Rev. B* **1988**, *37*, 785.

(7) Reiher, M.; Salomon, O.; Hess, B. A. *Theo. Chem. Acc.* **2001**, *107*, 45.

(8) Perdew, J. P. *Phy. Rev. B* **1986**, *33*, 8822.

(9) Perdew, J. P. *Electronic Structure of Solids*; Akademie: Berlin, 1991.

(10) When large imaginary frequency was observed at the D2–optimized geometry, we dropped the symmetry to C2 and further optimized until imaginary frequency became negligibly small (less than 100cm-1).

(11) Roos, B. O. *Adv. Chem. Phys.* **1987**, *69*, 399.

(12) Hirao, K. *Chem. Phys. Lett.* **1992**, *190*, 374.

(13) Hirao, K. *Chem. Phys. Lett.* **1992**, *196*, 397.

(14) Nakano, H. *J. Chem. Phys.* **1993**, *99*, 7983.

(15) Bergner, A.; Dolg, M.; Kuchle, W.; Stoll, H.; PreuB, H. *Mol. Phys.* **1993**, *80*, 1431.

(16) Dunning, T. H. J. *J. Chem. Phys.* **1989**, *90*, 1007.

(17) Frisch, M. J.; Trucks, G. W.; Schlegel, H. B.; Scuseria, G. E.; Robb, M. A.; Cheeseman, J. R.; Montgomery, J. A., Jr.; Vreven, T.; Kudin, K. N.; Burant, J. C.; Millam, J. M.; Iyengar, S. S.; Tomasi, J.; Barone, V.; Mennucci, B.; Cossi, M.; Scalmani, G.; Rega, N.; Petersson, G. A.; Nakatsuji, H.; Hada, M.; Ehara, M.; Toyota, K.; Fukuda, R.; Hasegawa, J.; Ishida, M.; Nakajima, T.; Honda, Y.; Kitao, O.; Nakai, H.; Klene, M.; Li, X. K., J. E.; Hratchian, H. P.; Cross, J. B.; Bakken, V.; Adamo, C.; Jaramillo, J.; Gomperts, R.; Stratmann, R. E.; Yazyev, O.; Austin, A. J.; Cammi, R.; Pomelli, C.; Ochterski, J. W.; Ayala, P. Y.; Morokuma, K.; Voth, G. A.; Salvador, P.; Dannenberg, J. J.; Zakrzewski, V. G.; Dapprich, S.; Daniels, A. D.; Strain, M. C.; Farkas, O.; Malick, D. K.; Rabuck, A. D.; Raghavachari, K.; Foresman, J. B.; Ortiz, J. V.; Cui, Q.; Baboul, A. G.; Clifford, S.; Cioslowski, J.; Stefanov, B. B.; Liu, G.; Liashenko, A.; Piskorz, P.; Komaromi, I.; Martin, R. L.; Fox, D. J.; Keith, T.; Al-Laham, M. A.; Peng, C. Y.; Nanayakkara, A.; Challacombe, M.; Gill, P. M. W.; Johnson, B.; Chen, W.; Wong, M. W.; Gonzalez, C.; Pople, J. A. *Gaussian 03*, D01 ed.; Gaussian Inc., 2004.

(18) M.W.Schmidt; K.K.Baldridge; J.A.Boatz; S.T.Elbert; M.S.Gordon; J.H.Jensen; S.Koseki; N.Matsunaga; K.A.Nguyen; S.J.Su; T.L.Windus; M.Dupuis; J.A.Montgomery. *J. Comput. Chem.* **1993**, *14*, 1347.

(19) *Molekel ver.5.4*; Swiss National Supercomputing Centre.: Manno, Switzerland, 2009.

(20) Frenking, G.; Frohlich, N. *Chemical Reviews* **2000**, *100*, 717.

(21) Koch, W.; Holthausen, M. C. *A Chemist's Guide to Density Functional Theory*, 2nd

ed.; Wiley-VCH, 2001.

(22) We also calculated the CASSCF energy with 10 orbitals of f1 to f10 at the DFT(B3LYP)-optimized geometry, but the quintet and higher spin states were more unstable than the singlet and triplet spin states.

Appendix:

Orbital energies of $\mathbf{M_{Cr}}$ and $\mathbf{M_{Mo}}$ (Figure A3-1) . The DFT calculations with B3LYP*, BP86, and PW91PW91 functionals of $\mathbf{M}_{M}$ (Table A3-1).

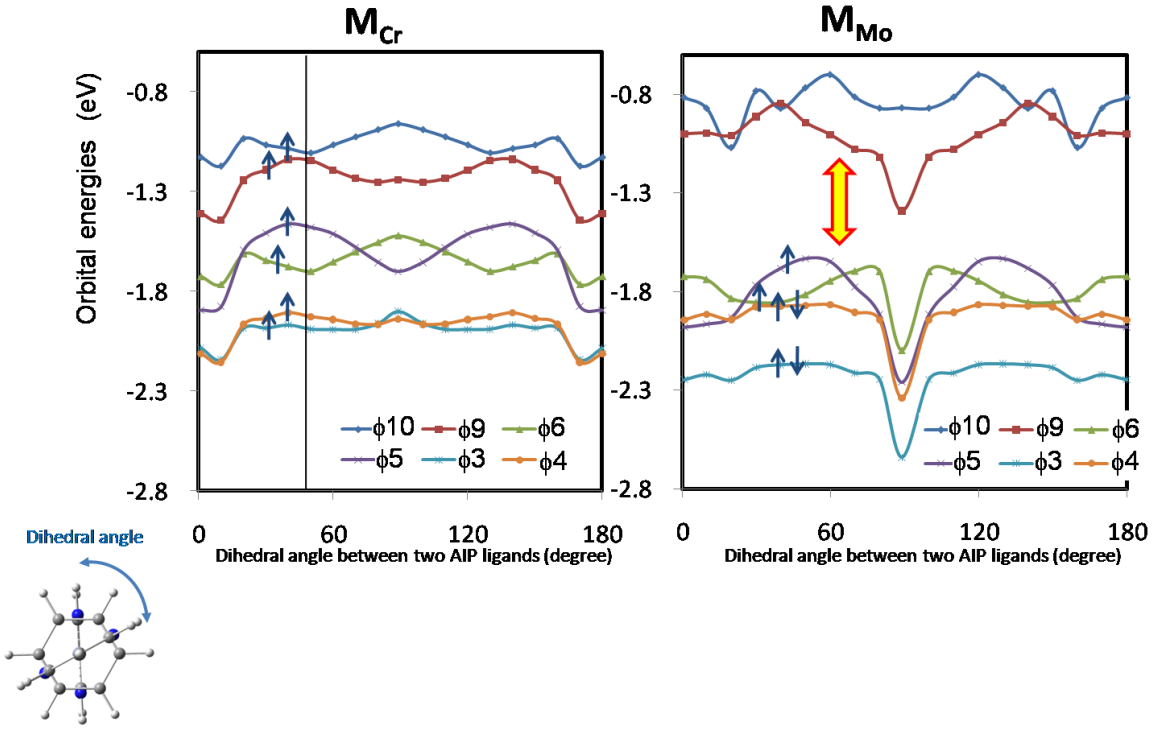

Figure A3-1. Orbital energies of $\mathbf{M_{Cr}}$ and $\mathbf{M_{Mo}}$, calculated by RO-B3LYP method in septet spin state.[a]

a: There appears a large gap between the ϕ9 and ϕ10 orbitals and the other orbitals in $\mathbf{M_{Mo}}$, while there is not such a large gap in $\mathbf{M_{Cr}}$.

Table A3-1. Relative energies[a] of various spin multiplicities of (μ-η^6:η^6-C_6H_6)[M(AIP)]$_2$ (AIPH = (Z)-1-amino-3-imino-prop-1-ene) $\mathbf{M}_{M}$, (*M* = Y, Zr, Nb, Mo, and Tc) calculated by the DFT method

	Y			Zr			Nb			Mo			Tc		
	B3LYP*	BP86	PW91	B3LYP*	BP86	PW91	B3LYP*	BP86	PW91	B3LYP*	BP86	PW91	B3LYP*	BP86	PW91
7tet							51.85	51.86	52.45	24.63	32.37	32.27			
5tet				20.06	408.53	26.21	**0.00**	**0.00**	**0.00**	19.09	17.42	17.85	32.02	31.78	32.08
3let	26.59	25.67	26.26	**0.00**	**0.00**	**0.00**	12.64	8.52	8.62	6.91	2.35	2.56	11.72	10.58	10.83
1let	**0.00**	**0.00**	**0.00**	0.94	3.30	3.70	27.55	102.77	103.45	**0.00**	**0.00**	**0.00**	**0.00**	**0.00**	**0.00**

[a]: Energy difference from the most stable spin state are shown in kcal/mol.

Part II

The Exact Solution of the Schrödinger Equation

Chapter 4
Free ICI (Iterative Complements Interaction) Calculations of Hydrogen Molecule

1. Introduction

When new quantum chemical methodology came out, the first molecular application was done to hydrogen molecule. In 1925, Heitler and London[1] applied newly born quantum mechanics to this molecule, which was a birth of quantum chemistry. After a pioneering study of helium atom by Hylleraas,[2] James and Coolidge[3] applied their explicitly correlated functions to hydrogen molecule and obtained very accurate results. Since then, Kolos,[4,5] Roothaan,[4] Wolniewitz,[6,7] Cencek,[8-10] Kutzelnigg[9] and others[9,12,13] have reported very accurate wave functions of this molecule. We have recently developed a new methodology for exactly solving the Schrödinger equation in an analytically expanded form.[10,11] So, in this paper, we apply our new methodology to the hydrogen molecule in order to examine the efficiency of the proposed method and the quality of the calculated energy and wave functions.

The new methodology is based on the study on the structure of the exact wave function.[16] When the structure of the exact wave is clarified, we construct the functions having such structure and make the variables included to be optimal by using the variational principle. However, when we formulate such theory based on the regular Schrödinger equation for atoms and molecules, we encounter a difficulty called singularity problem.[14] The formulation includes the integrals of the higher powers of the Hamiltonian, but such integrals diverge owing to the singularity of the Coulomb potentials included in the Hamiltonian. We showed that this difficulty could be avoided by introducing the scaled Schrödinger equation: [14] When we reformulate our theory so as to be based on the scaled Schrödinger equation, our theory for constructing the exact wave function becomes not to cause the singularity problem. Further, the free ICI method provides a very flexible way of constructing the exact wave function in both of the choices of the starting function ψ_0 and of the scaling g-function.

We explain in the next section our new methodology applied to the calculations of the exact wave function of the hydrogen molecule. Detailed computational aspects are then described and the results are summarized. We compare the present free ICI wave functions with the existing accurate wave functions in the field of explicitly correlated wave functions and examine the importance of the terms newly generated by the present free ICI method. The quality of the present wave function is examined by calculating the nuclear and electron cusp values.[17] The conclusion of this study is given in the last section. The appendix summarizes briefly the mathematics necessary for the present study.

2. Free ICI Method Applies to Hydrogen Molecule

We want to solve the Schrödinger equation of the hydrogen molecule

$$(H-E)\psi = 0 \tag{1}$$

with the Hamiltonian given by

$$H = -\tfrac{1}{2}\nabla_1^2 - \tfrac{1}{2}\nabla_2^2 - 1/r_{1a} - 1/r_{1b} - 1/r_{2a} - 1/r_{2b} + 1/r_{12} + 1/R \quad , \tag{2}$$

where 1 and 2 denote electrons, *a* and *b* two protons and *R* the internuclear distance. When we introduce elliptic coordinate,

$$\lambda_i = \left(r_{ia} + r_{ib}\right)/R, \quad \mu_i = \left(r_{ia} - r_{ib}\right)/R, \quad \rho = 2r_{12}/R \tag{3}$$

with *i* being 1 or 2, the kinetic operator and the potential operator are written as

$$\nabla_i^2 = \frac{4}{R^2\left(\lambda_i^2 - \mu_i^2\right)}\left[\frac{\partial}{\partial\lambda_i}\left(\lambda_i^2 - 1\right)\frac{\partial}{\partial\lambda_i} + \frac{\partial}{\partial\mu_i}\left(1-\mu_i^2\right)\frac{\partial}{\partial\mu_i} + \left\{\frac{1}{\lambda_i^2 - 1} + \frac{1}{1-\mu_i^2}\right\}\frac{\partial^2}{\partial\phi_i^2}\right], \tag{4}$$

and

$$V_{ne} + V_{ee} = \frac{2}{R}\left(-\frac{\lambda_1}{\lambda_1^2 - \mu_1^2} - \frac{\lambda_2}{\lambda_2^2 - \mu_2^2} + \frac{1}{\rho}\right), \tag{5}$$

respectively, where V_{ne} and V_{ee} represent the nuclear attraction and electron repulsion operators, respectively.

You see that the Hamiltonian includes the Coulombic potential that becomes plus or

minus infinity when two particles meet together. Higher powers of such potential become strongly diverging like a well potential so that the integrals of ψ^2 over such higher powers of the potential diverge. Therefore, the ICI calculations based on the ordinary Hamiltonian become impossible since it involves such diverging integrals. However, this singularity problem can be avoided by introducing the scaled Schrödinger equation

$$g(H-E)\psi = 0, \tag{6}$$

where g is a scaling function that is positive and non-zero everywhere except at the singular points r_0 and even there it satisfies

$$\lim_{r \to r_0} gV \neq 0. \tag{7}$$

The condition given by Eq.(7) is necessary for not to eliminate the information of the Hamiltonian at the singular points: the singularity is also an important physics of the system.

Based on the scaled Schrödinger equation, we can formulate the ICI method that is free from the singularity problem. The simplest ICI (SICI) wave function is defined by the recursion formula as

$$\psi_{n+1} = [1 + C_n\, g(H - E_n)]\psi_n, \tag{8}$$

which is guaranteed to become exact at convergence and we do not have the singularity difficulty in the course of the iteration process starting from the initial function ψ_0 because of the existence of the scaling function g. In the present calculation of the hydrogen molecule, we use actually the free ICI method that is formulated from the
SICI wave function as follows. We examine the rhs of Eq.(8), extract all the independent functions and arrange them as $\{\phi_i\}^{(n)}$, i = 1, . . , M_n. M_n is the number of the independent functions included in $\{\phi_k\}^{(n)}$.With this set of functions $\{\phi_k\}^{(n)}$, we expand our ψ_{n+1} as

$$\psi_{n+1} = \sum_{k=1}^{M_n} c_{k,n}\phi_k \ . \tag{9}$$

The coefficients $\{c_{k,n}\}$, k = 1, . . , M_n, are calculated with the variational principle (the ordinary Ritz variational principle is easier to use than the variational principle for the scaled Schrödinger equation).

In the free ICI method summarized above, we have two freedoms: one is the choice of the g function and the other is the choice of the starting function ψ_0. First, we explain the choice of the g function. Referring to the potential of the hydrogen molecule given by Eq.(5), we examined two different g functions

$$g_1 = \frac{\lambda_1^{\,2} - \mu_1^{\,2}}{\lambda_1} \frac{\lambda_2^{\,2} - \mu_2^{\,2}}{\lambda_2} \rho \tag{10}$$

and

$$g_2 = 1 - \frac{\lambda_1^{\,2} - \mu_1^{\,2}}{\lambda_1} - \frac{\lambda_2^{\,2} - \mu_2^{\,2}}{\lambda_2} + \rho \, . \tag{11}$$

The function g_1 satisfies the condition given by Eq.(7) but it may be too restrictive to freely produce the complement functions of the free ICI. Since g_1 is a *product* of the three inverses of the potentials, $V_{ne}(1)$, $V_{ne}(2)$ and V_{ee}, it makes the scaled wave function very complex. Further, when one of the three terms becomes zero, the other terms can be arbitrary. On the other hand, the function g_2 is a *sum* of the three inverse of the potentials and therefore the produced scaled wave function is simpler than that produced with the scaling function g_1. It produces more flexible complements functions than the function g_1, but it also produces the functions that are singular, so that we have to eliminate such functions from our expansion bases of the exact wave function: the wave function must be integrably finite by its definition.

The initial functions ψ_0 that were adopted in the present calculations are of two kinds. One is the simplest possible valence-bond type function given by

$$\psi_0^{(1)} = \exp[-\alpha(r_{1a} + r_{2a} + r_{1b} + r_{2b})] = \exp[-\alpha(\lambda_1 + \lambda_2)]. \tag{12}$$

The spin part is singlet and anti-symmetric, so that the spatial part is symmetric. This is a

product of the 1s orbitals centered on the two protons. The other initial function we used in this study is given by

$$\psi_0^{(L)} = \sum_{l=1}^{L} \exp[-\alpha(\lambda_1 + \lambda_2)]\rho^{l-1} . \qquad (13)$$

When L = 1, the initial function given by Eq.(13) is identical with that given by Eq.(12). This choice was based on the suggestion due to Kolos[5] that an inclusion of the functions of higher power in ρ accelerates the convergence of the expansion of the wave function. Kolos[5] also noted that the inclusion of the functions higher power in λ and μ did not accelerate the convergence. The orbital exponent α in Eqs.(12) and (13) is a non-linear parameter and may be optimized variationally at each iteration n, but the ICI theory claims that we can get the exact wave function with only linear expansions and so we fixed α to 1.1. The internuclear distance R was also fixed to the experimental value R = 1.4011 au, which is also used in other calculations to be compared with the present one.

The initial functions ψ_0 given above are analytical functions and by inserting these initial functions into Eq.(8), you get analytical functions that are necessary for constructing the first iteration function ψ_1: the kinetic operator in the Hamiltonian is essentially a differentiation operator and the potential function and the g function are multiplicative functions. These operations are automatically done by using symbolic operation programs like Maple.[14] Then, you get ψ_1 of the SICI in an analytical form. In the free ICI, you extract from this ψ_1 all the independent analytical functions, select only such functions that do not give divergence in the calculations of Hamiltonian and overlap integrals, and collect them as $\{\phi_k\}^{(1)}$, k = 1 . . . M_1. Then, you give an independent variable $c_{k,1}$ to each ϕ_k and expand your ψ_1 of free ICI as $\psi_1 = \sum_{k=1}^{M_1} c_{k,1}\phi_k$. The variables $\{ c_{k,1}\}$ are determined by the variational principle by solving the secular equation including overlap integrals. The Hamiltonian and overlap matrices are calculated without singularity problem for the existence of the g function. After the diagonalization you get the free ICI functions of the first iteration, ψ_1. The lowest solution is an approximation to the ground state and the second lowest solution is an approximation to the first excited state, etc. Putting this ψ_1 into Eq.(8) and

Table 4-1. Ground state energy of hydrogen molecule calculated with the g function given by Eq.(10)

Initial function (L)[a]	Number of iteration (n)	Number of basis function (M_n)	Total energy (au)
1	0	1	-0.999 780 120 198 08
	1	11	-1.169 313 411 900 71
	2	186	-1.174 470 133 104 04
	3	1156	-1.174 475 901 628 54
Best value			-1.174 475 931 397 74

[a] L is define in Eq.(13).

doing the same procedure as above, you obtain ψ_2. You repeat this iteration cycle until you get the convergence in your desired accuracy. Since the secular equation at each iteration cycle is due to the variational principle, the energy approaches from above the true energies, for both ground and excited states. Note that in the free ICI method, the next iteration cycle does not require the variables $\{ c_{k,n}\}$ of the former cycles, so that you can get the nth iteration free ICI functions $\{ \phi_k \}^{(n)}$ directly from ψ_0 by applying n times the operator part of Eq.(8) to ψ_0. This means that the accumulation of errors during the iteration process does not occur in the free ICI calculations.

The Hamiltonian and overlap integrals over the basis functions $\{ \phi_k \}^{(n)}$ were calculated analytically by applying and extending the method reported by James and Coolidge.[3] We reduced the basic integrals into the forms that can be handled with Maple. The details were summarized briefly in the Appendix for convenience. As we proceed iterations, the number of the independent functions $\{ \phi_k \}^{(n)}$ increases and they may involve the functions whose overlap integrals are rather close to unity. This means that the calculations must be performed in high accuracy and we kept 60 decimal-figure accuracy throughout the calculations. The secular equation was also solved in high precision using the GMP (GNU multiple precision arithmetic) library.[18]

3. Results

3.1. Energies

We first performed the free ICI calculations of the hydrogen molecule using the scaling

Table 4-2. Ground state energy of hydrogen molecule calculated with the. g function given by Eq.(11)

L[a]	n[b]	M_n[c]	Energy (au)	L[a]	n[b]	M_n[c]	Energy (au)
1	0	1	-0.999 780 120 198 080	2	0	2	-1.138 078 114 832 792
1	1	5	-1.164 409 776 802 471	2	1	9	-1.169 819 224 009 141
1	2	30	-1.172 712 604 472 602	2	2	57	-1.174 397 294 989 745
1	3	114	-1.174 434 056 534 598	2	3	215	-1.174 474 888 511 114
1	4	343	-1.174 475 391 331 891	2	4	624	-1.174 475 918 013 359
1	5	832	-1.174 475 917 716 333	2	5	1459	-1.174 475 930 608 043
1	6	1788	-1.174 475 930 732 940				
3	0	3	-1.142 973 092 050 475	4	0	4	-1.143 082 324 090 173
3	1	17	-1.173 036 862 957 403	4	1	25	-1.173 448 296 529 433
3	2	114	-1.174 471 341 851 610	4	2	174	-1.174 475 069 845 826
3	3	414	-1.174 475 901 329 452	4	3	630	-1.174 475 928 234 319
3	4	1119	-1.174 475 930 609 382	4	4	1667	-1.174 475 931 331 490
5	0	5	-1.143 084 264 123 815	6	0	6	-1.143 084 849 985 530
5	1	33	-1.173 489 787 488 802	6	1	41	-1.173 497 602 544 993
5	2	260	-1.174 475 797 933 379	6	2	346	-1.174 475 872 960 003
5	3	951	-1.174 475 931 085 682	6	3	1276	-1.174 475 931 318 436
5	4	2441	-1.174 475 931 391 155	6	4	3246	-1.174 475 931 397 736

[a] L of Eq.(13).
[b] Iteration number.
[c] M_n of Eq.(9): number of the basis functions at nth iteration.

function g_1 given by Eq.(10) and the simple initial function $\psi_0^{(1)}$ given by Eq.(12). We summarize in Table 4-1 the calculated energies at different iteration cycles. At the bottom of the table, we gave the best value obtained in the present free ICI calculations. You see that as the iteration proceeds, the energy approach the best value from above. Already at 2nd iteration with dimension 186, the energy is correct to five decimal figures, which is by far beyond the chemical accuracy. At third iteration, we obtain the energy correct to seven decimal figures. We will show later that our wave function is different from those existing in the literature.

We next performed the free ICI calculations using the scaling function g_2 given by Eq.(11) and a set of initial functions $\psi_0^{(L)}$ (L = 1 - 6) given by Eq.(13). The results are given in Table 4-2. When L of the initial function is unity, the initial function is the same as that used in Table 4-1, so that the difference is due only to the difference in the g function. In Table 4-2 the number of the complements functions at fifth iteration is 832 and the energy is

-1.174 475 917 au, which is lower than the energy of Table 4-1 at third iteration -1.174 475 901 au with 1156 independent functions. This means that the g_2 function given by Eq.(11) is more efficient than the g_1 function given by Eq.(10). Actually, a multiplication of the g_1 function increases the orders of all variables λ_1, λ_2 and ρ by unity or minus unity, but the g_2 function increases the order of only one of the variables, λ_1, λ_2 or ρ by unity, so that the g_2 function can produce more flexible basis functions than the g_1 function, leading to more-efficient basis functions.

Table 4-2 gives a comparison of the usage of different initial functions, all with the same g_2 function. As L increases, the initial function already includes explicitly the inter-electron distance, ρ. If ρ is essential, it is better to include it from the beginning of the calculations and this is the case as seen from the table: the energy with L = 1 and n = 6 is -1.174 475 930 732 au with 1788 functions, which is higher in energy than the case of L = 4 and n = 4 with only 1667 functions, -1.174 475 931 331 au. By using better-quality initial function, we can get better energy with smaller number of basis functions. However, probably, more important implication of Table 4-2 is that we can always get very accurate results as we perform iterations, independent of the quality of the initial functions. When the number of the basis functions is similar, the calculated energy is more-or-less similar.

Between the differences in the g function and in the initial function, the difference in the g function causes a larger difference of the calculated results. We see from the comparison of Tables I and II that the energy calculated with 1156 functions produced with the g_1 function, -1.174 475 907 au is higher than the one calculated with only 624 functions (about half) produced with the g_2 function, -1.174 475 918 au. This example emphasizes again the

Table 4-3 . Ground state energy of hydrogen molecule calculated with the g function given by Eq.(10)., R=1.4 a.u.

Initial function (L)[a]	Number of iteration (n)	Number of basis function (M_n)	Energy (au)
6	0	6	-1.143 006 074 717
6	1	41	-1.173 494 068 035
6	2	346	-1.174 475 655 534
6	3	1276	-1.174 475 714 138

importance of the choice of the *g* function.

In the literature, most earlier calculations were done for the bond length of 1.4 au. So, we also performed the free ICI calculations for R = 1.4 au and the results are given in Table 4-3. The *g* functions is due to Eq.(11) and the initial function is due to Eq.(13) with L = 6. Comparing the energies for R = 1.4 and 1.4011, the latter is lower showing the minimum-energy bond length should be closer to the latter. The experimental bond length is 1.40112 au.

Many important studies have been reported on the accurate analytical calculations of the wave function of the hydrogen molecule.[13] We summarize in Table 4-4 some of the representative studies. As the present result, we gave our best result shown in Table 4-2. First, we notice that our best result is certainly the best worldwide in the literature. The second best is the result due to Cencek and Rychlewski[10] who used Gaussian functions. Our free ICI wave functions are composed of the Slater-type functions and are written as

$$\psi = \sum_i c_i (1 + p_{12}) \exp[-\alpha(\lambda_1 + \lambda_2)] \lambda_1^{m_i} \lambda_2^{n_i} \mu_1^{j_i} \mu_2^{k_i} \rho^{l_i}, \qquad (14)$$

where p_{12} is an exchange operator of the electron coordinates. This wave function is very simple and similar to the original wave function due to James and Coolidge.[3] Our wave function and James-Coolidge wave function have a simple exponential form but differ in the

Table 4-4. History of hydrogen molecule wave function.

Type of wave function	Reference	H-H distance (au)	Total energy (au)
Hartree-Fock	Sundholm[a]	1.4	-1.133 629 573
Full CI ($33\sigma 27\pi 18\delta 16\phi$)	Liu-Hagstrom[b]	1.4	-1.174 304 3
Hylleraas type	James-Coolidge[c]	1.4	-1.173 539[c]
Gaussian functions	Cencek-Kutzelnigg[d]	1.4	-1.174 475 714 037
Free ICI (extended Hylleraas type)	Present	1.4	-1.174 475 714 138
Hylleraas type	Wolniewicz[e]	1.4011	-1.174 475 930 742
Gaussian functions	Cencek-Rychlewski[f]	1.4011	-1.174 475 931 39
Free ICI (extended Hylleraas type)	Present	1.4011	-1.174 475 931 397 74

[a] Ref. 20. [b] Ref. 11. [c] Ref. 3. [d] Ref. 9. [e] Ref. 7. [f] Ref. 10.

powers *m*, *n* of the variables λ_1 and λ_2 : *m*, *n* are always non-negative in the James-Coolidge wave functions but they can be even negative in the present free ICI wave functions. In other words, our ICI theory starting from the initial functions given by Eqs.(12) and (13) generates not only non-negative power terms of λ_1 and λ_2, but also negative power terms of them. Such functions are theoretically more relevant for describing the exact wave function of the hydrogen molecule than the original James-Coolidge functions. We show later in this paper some of the important roles of these negative-power functions in our wave function. The high quality of the present free ICI wave function would be attributed to the existence of these negative *m*, *n* terms.

Kolos and Wolniewicz[5-7] extended later the James-Coolidge wave function into more general forms like

$$\psi = \sum C\,(1+p_{12})\,\exp[-\alpha\lambda_1 - \bar{\alpha}\lambda_2]\;\lambda_1^{\,m}\;\lambda_2^{\,n}\;\mu_1^{\,j}\;\mu_2^{\,k}\;\rho^{l} \times [\exp(\beta\mu_1 + \bar{\beta}\mu_2) + (-1)^{j+k}\exp(-\beta\mu_1 - \bar{\beta}\mu_2)\;] \tag{15}$$

but they always used non-negative *m*, *n* in their wave functions. A reason of extending the James-Coolidge wave function was that the James-Coolidge-type wave function does not have proper asymmetric form as the inter-proton distance increases up to infinity. On the other hand, Komasa, Cencek, Rychlewski, Kutzelnigg, et al[7,8] obtained very accurate wave functions using the Gaussian-type functions as

$$\Psi = \sum C\,(1+p_{12})\,\exp[-\alpha r_{1C}^2 - \bar{\alpha} r_{2C'}^2 - \beta r_{12}^2]\,. \tag{16}$$

Primitive questions about this type of wave function are that how well the nuclear and electron cusps[17] are described and how important these properties are in the actual wave functions.

Table 4-4 shows also the full CI energy[11] and the Hartree-Fock energy.[20] These calculations were performed at *R* = 1.40 au, like the original James-Coolidge calculations, while the other calculations were done at *R* = 1.4011 au. The difference between the present result and the Hartree-Fock energy gives the best value of the correlation energy and it is -0.011 129 741 au. The full CI energy is the 'exact' energy within a given space of the basis

Table 4-5. First iteration eleven-term wave function of the free ICI calculation shown in Table 4-2 (L = 2, n = 1).[a] The energy is −1.169 819 224 a.u.

No	[m, n, j, k, p]	Coefficient	No	[m, n, j, k, p]	Coefficient
1	[0, 0, 0, 0, 0]	1.000000000	7	[-1, 1, 2, 0, 0]	1.321269627
2	[0, 1, 0, 0, 1]	0.3669590863	8	[-1, 1, 2, 0, 1]	-0.008229630145
3	[1, 1, 0, 0, 0]	0.7048962113	9	[-1, -1, 0, 2, 1]	0.2792523585
4	[1, 1, 0, 0, 1]	-0.1126197289	10	[-1, -1, 2, 2, 0]	0.5959010778
5	[-1, 0, 2, 0, 1]	0.8697244891	11	[-1, -1, 2, 2, 1]	0.05876570834
6	[-1, 1, 0, 0, 1]	0.3670940863			

[a] Each basis function is normalized to unity.

set. For the [30s29p12d9f] Gaussian-type basis, the energy is -1.174 285 au with 22578 variables. Referring to Table 4-2, this energy is worse than that of the calculation, L=2 and n=2, −1.174 397 a.u., so that we estimate that this energy would be obtained with the function s less than 57, if we use the present free ICI method.

3.2. Importance of the terms with negative powers of λ_i

The free ICI method produces automatically the analytical basis functions that are necessary to expand the exact wave function under a choice of the initial function ψ_0 and the g function. In the present choice of the initial function, the ICI method always produced the terms of λ_i that have not only non-negative powers but also negative powers. Since these terms were produced theoretically by the ICI method, they are considered to be necessary for constructing the exact wave function. However, such terms were not included in the previous calculations by James and Coolidge, Kolos and Wolniewitz. So, we examine here the importance of such terms in constructing the accurate wave functions of the hydrogen molecule. Note that for helium atom the importance of similar terms with negative powers has been pointed out by Kinoshita[21] for describing the accurate wave functions.

First, the importance of the terms with negative powers of λ_i is understood from the high performance of the present free ICI calculations as presented in the preceding section. We show here other two more direct evidences. In Table 4-5, we show the expansion coefficients of the eleven basis functions obtained at the first iteration of the calculation shown in Table 4-2. This calculation is based on the g_1 function given by Eq.(10) and the

Table 4-7. Best five-term James-Coolidge-type wave function of hydrogen molecule within the positive range of $0 \le m_i, n_i \le 1$, $0 \le j_i, k_i \le 2$, $0 \le l_i \le 1$. R=1.4 au and α=0.95. The calculated energy was -1.171 998 568a.u.

No	[m, n, j, k, l]	Coefficient	No	[m, n, j, k, l]	Coefficient
1	[0, 0, 0, 0, 0]	1.000 000 000	4	[0, 0, 1, 1, 0]	-0.067 134 733
2	[0, 0, 0, 0, 1]	0.802 238 155	5	[1, 1, 0, 0, 0]	-0.087 098 459
3	[0, 0, 0, 2, 0]	0.282 362 668			

[a]Each basis function is normalized to unity.

initial function $\psi_0^{(1)}$ given by Eq.(13). The coefficients given in Table 4-5 are those for the terms of Eq.(14) designated by [*m*,*n*,*j*,*k*,*l*] that are normalized to unity, and the first-iteration free ICI wave function $\psi_1^{(1)}$ was normalized such that the coefficient of the initial function, [0,0,0,0,0] is unity. One can see from Table 4-5 that the first four terms, 1 – 4, are conventional ones and the others are the terms whose *m* and/or *n* are negative. You see that the terms 5, 6, 7, and 10 have very large coefficients, showing the importance of the negative power terms of λ_i.

Kolos and Roothaan[4] calculated the five term James-Coolidge wave function using only positive powers and obtained the energy of -1.171 619 au. We have examined the best possible five-term extended James-Coolidge-type wave function allowing the powers in Eq.(14) to change within $-1 \le m_i, n_i \le 1$, $|m_i - n_i| \le 1$, $0 \le j_i, k_i \le 2$, $0 \le l_i \le 1$. The bond length *R* and the orbital exponent α are the same as those used by Kolos and Roothaan,[4] *R* = 1.4 au and $\alpha = 0.95$. Table 4-6 shows the calculated best wave function. It includes one term that has negative *n* and its coefficient is second smallest. The calculated energy was -1.172 276 534 au. We also performed a similar calculation within the positive range of $0 \le m_i, n_i \le 1$, $0 \le j_i, k_i \le 2$, $0 \le l_i \le 1$ and obtained the best wave function as shown in Table 4-7. The calculated energy was -1.171 998 568 au. The last term [1,1,0,0,0] was not included

Table 4-6. Best five-term extended James-Coolidge-type wave function of hydrogen molecule within $-1 \le m_i, n_i \le 1$, $|m_i - n_i| \le 1$, $0 \le j_i, k_i \le 2$, $0 \le l_i \le 1$. *R* = 1.4 au and $\alpha = 0.95$. The calculated energy was –1.172 276 534 a.u.

No	[m, n, j, k, l]	Coefficient	No	[m, n, j, k, l]	Coefficient
1	[0, 0, 0, 0, 0]	1.000 000 000	4	[0, 0, 1, 1, 0]	-0.055 207 501
2	[0, 0, 0, 0, 1]	0.718 124 997	5	[0, -1, 0, 2, 1]	0.081 476 902
3	[0, 0, 0, 2, 0]	0.198 062 046			

[a]Each basis function is normalized to unity.

Table 4-8. Recalculated 13 term[a] wave function of James and Coolidge with R=1.4 au and α=3/4. The calculated energy was -1.173 539 685 a.u.

No.	[m, n, j, k, l]	Coefficient	No.	[m, n, j, k, l]	Coefficient
1	[0, 0, 0, 0, 0]	1.000 000 000	8	[1, 0, 0, 0, 0]	-0.933 408 702
2	[0, 0, 0, 0, 1]	0.553 586 789	9	[1, 0, 0, 2, 0]	-0.052 106 263
3	[0, 0, 0, 0, 2]	-0.099 140 955	10	[1, 0, 1, 1, 0]	0.044 627 723
4	[0, 0, 0, 2, 0]	0.195 335 087	11	[1, 0, 2, 0, 0]	-0.074 756 346
5	[0, 0, 0, 2, 1]	0.044 417 387	12	[2, 0, 0, 0, 0]	0.315 198 529
6	[0, 0, 1, 1, 0]	-0.062 129 657	13	[1, 0, 0, 0, 1]	-0.188 359 478
7	[0, 0, 1, 1, 1]	-0.006 994 087			

[a] Basis functions are normalized to unity.

in the original 5-term Kolos-Roothaan wave function, though it iwas included in their 12-term wave function. They included instead the term [0,1,0,0,0]. Other four terms were common in all of these three wave functions. It is concluded that within 5-term James-Coolidge wave functions of hydrogen molecule, a better result is obtained by allowing negative power terms of λ_i.

Another piece of evidence was obtained by performing the calculations similar to the original James-Coolidge one. We recalculated the James-Coolidge 13 term wave function and showed the result in Table 4-8. The calculated energy was -1.173 539 685 au, which was slightly different from the original one E=-1.173 501 au reported by James and Coolidge later.[3] (For the 5 and 11 term wave functions, the present recalculations gave the same energy as those given in the original paper.[3]) We replaced the smallest two terms, terms Nos. 7 and 13 of the original 13 terms with the terms having negative *m*, *n* terms and the result was shown in Table 4-9. The calculated energy was – 1.173 962 233 au which was substantially lower than the energy of the original 13 term wave function. Actually, the replaced terms Nos. 12 and 13 of Table 4-9 have large coefficients. Though the present replacement of the two terms is rather arbitrary, this result also supports the importance of the negative power terms of λ_i in the expansion of Eq.(14).

We also have some intuitive explanations about the importance of the negative-power terms of λ_i. Figure 4-1 shows the illustrations of the functions $\phi = \exp(-\lambda)\lambda^m \mu^2$ with positive and negative *m*. Figure 4-1(a) is for *m* = 1,2,3 and Figure 4-1(b) for *m* = 0,-1,-2 and

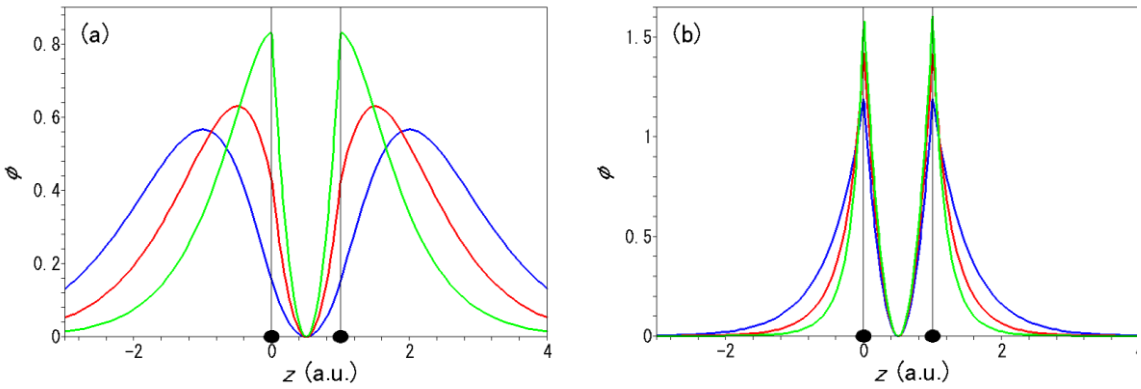

Figure 4-1. (a) Plot of the function $\phi = \exp(-\lambda)\lambda^m\mu^2$ with m = 1 (green), m = 2 (red), and m = 3 (blue). The two protons are at z = 0 and z = 1. (b) Plot of the function $\phi = \exp(-\lambda)\lambda^m\mu^2$ with m = -2 (green), m = -1 (red), and m = 0 (blue). The two protons are at z = 0 and z = 1.

the two protons were assumed to be at z = 0 and 1. Note that the variables λ_i and μ_i describe the wave function outside and inside, respectively, of the two nuclei. We see that the functions with positive m do not show a nice cusp-like behavior near the positions of the nuclei but those with negative m shows a reasonable cusp-like behavior at the nuclear positions. This also explains the importance of the functions with negative powers of λ_i.

3.3 Cusp Properties

The exact wave function must satisfy some necessary conditions like variational condition, virial theorem, cusp condition, etc. In the free ICI wave function given by Eq.(14), the coefficients $\{c_i\}$ were calculated with the variational principle. We did not optimize the exponent α, but the energy gradient $\partial E/\partial\alpha$ of the wave function composed of the 1747 functions (L = 6, n = 3) was only 1.84 × 10^{-19} at $\alpha = 1.1$. Similarly, the energy gradient (force) $\partial E/\partial R$ acting on the proton of the H_2 molecule at R = 1.4011 au was 6.30 × 10^{-6} au, so that the optimal length R should be smaller than 1.4011 au: it would be 1.40081 – 1.40083 au.[4] Below, we examine how the present ICI wave function satisfies the cusp condition.

Kato[17] presented two cusp conditions for the exact many-electron wave functions: nuclear cusp condition and electron cusp condition. The nuclear cusp condition is expressed for the hydrogen molecule as[4]

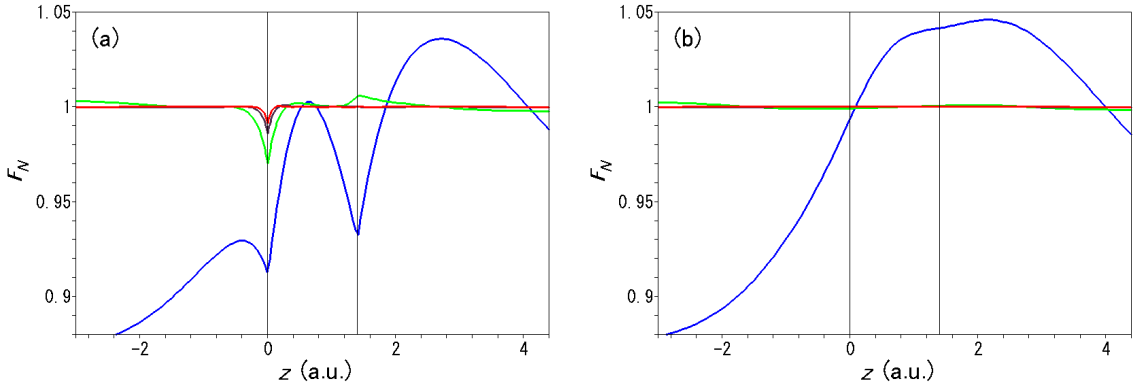

Figure 4-2. (a) Plots of the nuclear-electron cusp function F_N along the z coordinate that connects two protons lying at z = 0 and z = 1.4011 au at different iteration process of the free ICI calculations using the g_2 function and the initial function $\psi_0^{(6)}$: Iteration number n = 1 (blue), n = 2 (green), n = 3 (violet) and n = 4 (red). The wave function at n = 4 is our best wave function reported in this paper. (b) Plots of the nuclear-electron cusp function F_N along the axis lying parallel to the z coordinate that connects two protons lying at z = 0 and z = 1.4011 au at different iteration process of the free ICI calculations using the g_2 function and the initial function $\psi_0^{(6)}$: Iteration number n = 1 (blue), n = 2 (green), n = 3 (violet) and n = 4 (red). The wave function at n = 4 is our best wave function reported in this paper.

$$F_N(\lambda_2,\mu_2)=\left[\frac{-1}{R\lambda_1\Psi}\left(\lambda_1\frac{\partial\Psi}{\partial\lambda_1}-\mu_1\frac{\partial\Psi}{\partial\mu_1}\right)\right]_{\lambda_1=1,\mu_1=-1}=Z_A=1, \tag{17}$$

which is the condition when electron 1 is at the proton a. The lhs of Eq.(17) is a function of the electron coordinate 2, so that equation (17) must be satisfied at any coordinate of electron 2, except at the additional singular point, $\lambda_2=1$ and $\mu_2=-1$ where electron 2 also collides with the proton a. The electron cusp condition is given by

$$F_e(\lambda_i,\mu_i)=\left[\frac{1}{\Psi}\frac{\partial\Psi}{\partial r_{12}}\right]_{r_{12}=0}=\frac{1}{2} \tag{18}$$

which is the condition when two electrons meet together. The lhs is also the function of the variables other than. $\rho=r_{12}$ and so it must be 1/2 everywhere except for the additional singular points.

Figure 4-2 shows the plots of the function F_N along the iteration process of the free ICI calculations using the g_2 function and the initial function $\psi_0^{(6)}$: at fourth iteration of this calculation we have obtained the world best value of the energy of the hydrogen molecule shown in Tables 4-2 and 4-1 . Figure 4-2(a) is along the z coordinate that connects two

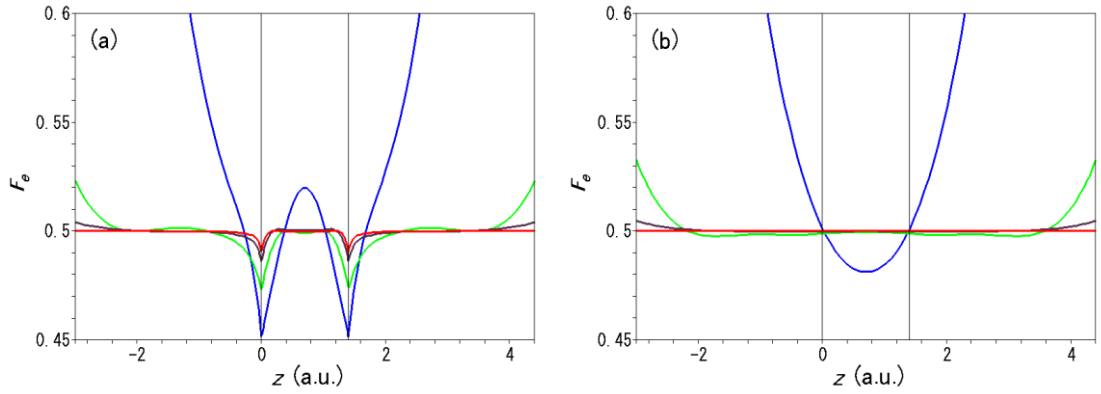

Figure 4-3. (a) Plots of the electron-electron cusp function F_e along the z coordinate that connects two protons lying at z = 0 and z = 1.4011 au at different iteration process of the free ICI calculations using the g_2 function and the initial function $\psi_0^{(6)}$: Iteration number n = 1 (blue), n = 2 (green), n = 3 (violet) and n = 4 (red). The wave function at n = 4 is our best wave function reported in this paper. (b) Plots of the electron-electron cusp function F_e along the axis lying parallel to the z coordinate that connects two protons lying at z = 0 and z = 1.4011 au at different iteration process of the free ICI calculations using the g_2 function and the initial function $\psi_0^{(6)}$: Iteration number n = 1 (blue), n = 2 (green), n = 3 (violet) and n = 4 (red). The wave function at n = 4 is our best wave

protons lying at z = 0 and z = 1.4011 au and Figure 4-2(b) is along an axis lying parallel to the z coordinate and distant from it by 1 au. The figures show the local values of the cusp function F_N when electron 2 moves along these axes. Though the cusp value of the free ICI wave function is very different from unity at first iteration (n = 1), it becomes closer and closer to unity as the iteration proceeds. At n = 4, the cusp values are unity everywhere except at the position of the nucleus a (the origin of Figure 4-2(a)), where an additional singularity occurs. There, not only the nucleus a collides with the two electrons, but also the two electrons collide with each other: this is a new singularity point not expressed by Eq.(15). It is remarkable that at z = 1.4011 au of Figure 4-1(a), the value of F_N becomes unity at n = 4: there, the two cusp conditions for the two pairs, electron 1 - nucleus a and electron 2 - nucleus b, are satisfied independently.

Figure 4-3 shows the plots of the function F_e along the iteration process of the same free ICI wave functions given in Figure 4-2 above. Figure 4-3(a) shows the value of the cusp function F_e when the colliding two electrons move along the z axis and Figure 4-3(b) along the axis separated by 1 au from the z-axis. Again, the cusp value is improved as the iteration proceeds: the cusp value of the wave function at n = 1 is far from one half but it becomes

closer and closer to one half as n increases. At the nuclear positions a and b along the z-axis, the cusp value is different from one half even for the best wave function since there an additional singularity occurs,: there two colliding electrons collide further with the nucleus. Except at these two points, the cusp function F_e of our best free ICI wave function (n = 4) is flat and takes one half everywhere along the z axis and along the axis apart 1 au from the z-axis.

4 Conclusion

The free ICI method developed in earlier papers has been applied to hydrogen molecule to calculate its very accurate wave function. We could obtain the world best variational wave function within a rather simple Hylleraas-James-Coolidge form. The difference of the present free ICI wave function from the previous ones was the existence of the negative-power terms of λ_i. These terms were generated automatically by the free ICI formalism, so that we believe they are essential for effective description of the exact wave function.

We have examined two different g functions and several initial functions. Clever choice of g function was more important than the different choices of the initial function. However, it was also true in the present calculations that any initial functions have given the converging series of energies to the same best value. We have also shown that the cusp value, a rather sensitive property of the wave function, was substantially improved as the iteration proceeds.

Acknowledgment:

This research was supported by the Grant for Creative Scientific Research from the Ministry of Education, Science, Culture, and Sports of Japan.

References:

(1) W. Heitler and F. London, *Z. Phys.* **1927** *44*, 455.

(2) E. A. Hylleraas, *Z. Phys.* **1929** *54*, 347.

(3) H. M. James and A.S. Coolidge, *J. Chem. Phys.* **1933,** *1***,** 825 ; ibid., **1935**, *3*, 129 .

(4) W. Kolos and C. C. Roothaan, *Rev. Mod. Phys.* **1960** *32*, 205 ; ibid., **1960** *32*, 219 .

(5) W. Kolos and L. Wolniewicz, *J. Chem. Phys.* **1964** *41*, 3663 ; ibid., **1965** *43*, 2429; W. Kolos and L. Wolniewicz, *Chem, Phys, Lett.*, **1974** *24*, 457;W. Kolos, J. Chem. Phys. **1994** *101*, 1330.

(6) L. Wolniewicz, *J. Chem. Phys.*, **1993** *99*, 1851

(7) L. Wolniewicz, *J. Chem. Phys.* **1995** *103*, 1792.

(8) J. Komasa, W. Cencek, and J. Rychlewski, *Phys. Rev. A*, **1992** *46*, 2351; J. Rychlewski, W. Cencek, and J. Komasa, *Chem. Phys. Lett.*, **1994** *229*, 657

(9) W. Cencek and W. Kutzelnigg, *J. Chem. Phys.* **1996** *105*, 5878

(10) W. Cencek and J. Rychlewski, cited in Ref. 13.

(11) J. W. Liu and S. Hagstrom, *Phys. Rev. A*, **1993** *48*, 166

(12) S. A. Alexander and R. L. Coldwell, *J. Chem. Phys.*, **2004** *121*, 11557

(13) J. Rychlewski and J. Komasa in "*Explicitly Correlated Wave Functions in Chemistry and Physics – Theory and Applications*", Ed. by J. Rychlewski, Kluwer Academic Pub., Dordrecht, **2003**, pp. 91 - 147.

(14) H. Nakatsuji, *Phys. Rev. Lett.* **2004** *93*, 030403-1 .

(15) H. Nakatsuji, *Phys. Rev. A.* **2005** *72*, 062110 .

(16) H. Nakatsuji, *J. Chem. Phys.* **2000** *113*, 2949; H. Nakatsuji and E. R. Davidson, ibid., **2001** *115*, 2000; H. Nakatsuji, ibid., **2001** *115*, 2465; **2002** *116*, 1811; H. Nakatsuji and M. Ehara, ibid., **2002** *117*, 9.

(17) T. Kato, Commun. Pure Appl. Math., **1957** *10*, 151.

(18) About the GPM library, see http://swox.com/gmp/ and http://www.cs.nyu.edu/exact/core/gmp/.

(19) Maple: A product of Waterloo Maple Inc., Waterloo, Ontario, Canada, see http://www.maplesoft.com

(20) D. Sundholm, *Chem. Phys. Lett.*, **1988** *149*, 251

(21) T. Kinoshita, *Phys. Rev.* **1957** *105***,** 1490.

(22) K. Ruedenberg, *J. Chem. Phys.* **1951** *19*, 1459.

Appendix

We briefly explain the method of analytical calculations of the integrals that appear in the variational calculations of the free ICI wave function given in the form of Eq.(14). The formulation is a small generalization of the one presented by James and Cooligde in their original paper.[3] Ruedenberg[22] also gave the formulas related to the present case.

The integrals we have to calculate are the Hamiltonian and overlap integrals,

$$\begin{aligned} H_{ij} &= \iint \phi_i \, H \, \phi_j \, d\tau_1 \, d\tau_2 \\ S_{ij} &= \iint \phi_i \, \phi_j \, d\tau_1 \, d\tau_2 \end{aligned} \tag{a1}$$

where the functions ϕ_i have the form.

$$\phi_i = (1 + p_{12}) \exp[-\alpha(\lambda_1 + \lambda_2)] \lambda_1^{m_i} \lambda_2^{n_i} \mu_1^{j_i} \mu_2^{k_i} \rho^{l_i} \, . \tag{a2}$$

where *m* and *n* are positive and negative integers and zero and *j*, *k*, and *l* are non-negative integers. Applying the Hamiltonian on ϕ_i, we obtain

$$H\phi_i = \sum_j d_j \, (1 + p_{12}) \, \exp[-\alpha \, (\lambda_1 + \lambda_2) \,] \lambda_1^{\,m_j} \;\; \lambda_2^{\,n_j} \;\; \mu_1^{\,j_j} \;\; \mu_2^{\,k_j} \;\; \rho^{\,l_j} \, , \tag{a3}$$

which are similar in form to Eq.(14) and this process can be easily done with the use of Maple or other similar program. The Jacobian for the elliptic coordinate is given by

$$d\tau_1 \, d\tau_2 = \frac{R^6}{64} \left(\lambda_1^{\,2} - \mu_1^{\,2} \right) \left(\lambda_2^{\,2} - \mu_2^{\,2} \right) d\lambda_1 \, d\lambda_2 \, d\mu_1 \, d\mu_2 \, d\varphi_1 \, d\varphi_2 \, . \tag{a4}$$

Then, all the integrals reduce to the sums of the following integrals

$$I = \int \exp[-2\alpha \, (\lambda_1 + \lambda_2) \,] \;\; \lambda_1^{\,m} \;\; \lambda_2^{\,n} \;\; \mu_1^{\,j} \;\; \mu_2^{\,k} \;\; \rho^{\,l} \, d\lambda_1 \, d\lambda_2 \, d\mu_1 \, d\mu_2 \, d\varphi_1 \, d\varphi_2 \tag{a5}$$

Now, we summarize the necessary formulas to calculate these integrals. First, the variables of ρ are transformed by using the relation

$$\begin{aligned} \rho^2 = {} & \lambda_1^{\,2} + \lambda_2^{\,2} + \mu_1^{\,2} + \mu_2^{\,2} - 2 - 2 \, \lambda_1 \, \lambda_2 \, \mu_1 \, \mu_2 \\ & - 2 \left[\left(\lambda_1^{\,2} - 1 \right) \left(\lambda_2^{\,2} - 1 \right) \left(1 - \mu_1^{\,2} \right) \left(1 - \mu_2^{\,2} \right) \right]^{1/2} \cos\left(\varphi_1 - \varphi_2 \right) \end{aligned} \tag{a6}$$

that is obtained from the second cosine formula and the expansion

$$\rho^{-1} = \sum_{\tau=0}^{\infty} \sum_{N=0}^{\infty} D_\tau{}^N P_\tau{}^N \begin{pmatrix} \lambda_1 \\ \lambda_2 \end{pmatrix} Q_\tau{}^N \begin{pmatrix} \lambda_2 \\ \lambda_1 \end{pmatrix} P_\tau{}^N (\mu_1) P_\tau{}^N (\mu_2) \cos N(\varphi_1 - \varphi_2) \qquad \text{(a7)}$$

that is the Von Neuman's expansion, where

$$\begin{aligned} D_\tau{}^0 &= 2\tau + 1, \\ D_\tau{}^N &= 2(2\tau+1)\left[\frac{(\tau - N)!}{(\tau + N)!}\right]^2 \quad (N > 0). \end{aligned} \qquad \text{(a8)}$$

P and Q are the unnormalized complex associated Legendre functions of the first and second kinds and we take upper variable when $\lambda_2 \geq \lambda_1$ and lower variable otherwise.

We introduce the function *Z* defined by

$$Z(\nu, m, n, j, k, l) = \int \exp[-2\alpha(\lambda_1 + \lambda_2)]\, \lambda_1{}^m\, \lambda_2{}^n\, \mu_1{}^j\, \mu_2{}^k\, \rho^l M^\nu d\lambda_1\, d\lambda_2\, d\mu_1\, d\mu_2\, d\varphi_1\, d\varphi_2 \qquad \text{(a9)}$$

where

$$M = \left[(\lambda_1{}^2 - 1)(\lambda_2{}^2 - 1)(1 - \mu_1{}^2)(1 - \mu_2{}^2)\right]^{1/2} \cos(\varphi_1 - \varphi_2) \qquad \text{(a10)}$$

then, the integral *I* defined by Eq.(a5) is written with this *Z* function as

$$I = Z(0, m, n, j, k, l)\,. \qquad \text{(a11)}$$

From Eq.(a6), we obtain the recursion formula

$$\begin{aligned} Z(\nu, m, n, j, k, l) = {} & Z(\nu, m+2, n, j, k, l-2) + Z(\nu, m, n+2, j, k, l-2) \\ & + Z(\nu, m, n, j+2, k, l-2) + Z(\nu, m, n, j, k+2, l-2) \\ & - 2Z(\nu, m, n, j, k, l-2) - 2Z(\nu, m+1, n+1, j+1, k+1, l-2) \\ & - 2Z(\nu+1, m, n, j, k, l-2) \end{aligned} \qquad \text{(a12)}$$

which implies that the value of the function *Z* reduces finally to the sum of the following terms, depending on the parity of the integer *l*.

$$\begin{aligned} &\text{case a,} \quad Z(\nu, m, n, j, k, 0)\,, \quad (l, \text{ even}) \\ &\text{case b,} \quad Z(\nu, m, n, j, k, -1)\,, \quad (l, \text{ odd}) \end{aligned} \qquad \text{(a13)}$$

For case a, the *Z* value is written as

$$Z(\nu, m, n, j, k, 0) = L(\nu, m, \alpha)\, L(\nu, n, \alpha) U(\nu, j) U(\nu, k)\, f_0(\nu) \qquad \text{(a14)}$$

where

$$L(\nu,m,\alpha)=\int_1^\infty \exp(-2\alpha\lambda)\,(\lambda^2-1)^{\frac{\nu}{2}}\,\lambda^m\,d\lambda$$

$$U(\nu,j)=\int_{-1}^{1}(1-\mu^2)^{\frac{\nu}{2}}\,\mu^j\,d\mu \qquad \text{(a15)}$$

$$f_0(\nu)=\int_{-\pi}^{\pi}\int_{-\pi}^{\pi}\cos^\nu(\varphi_1-\varphi_2)\;d\varphi_1\,d\varphi_2$$

When ν is odd, $f_0(\nu)$ is zero, so that $Z(\nu,m,n,j,k,0)=0$.

For case b, we substitute Eq.(a7) into Eq.(a9) and obtain the *Z* value written in the form

$$Z(\nu,m,n,j,k,-1)=\sum_{\tau=0}^{\infty}\sum_{N=0}^{\infty}D(\tau,N)\,R(\tau,\nu,N,j)\,R(\tau,\nu,N,k)\,H(\tau,\nu,N,m,n,\alpha)\,f(\nu,N) \qquad \text{(a16)}$$

where

$$D(\tau,N)=D_\tau^{\,N}$$

$$R(\tau,\nu,N,j)=\int_{-1}^{1}(1-\mu^2)^{\frac{\nu}{2}}\,P_\tau^{\,N}(\mu)\,\mu^j\,d\mu$$

$$H(\tau,\nu,N,m,n,\alpha)$$

$$=\int_1^\infty\int_1^\infty \exp[-2\alpha(\lambda_1+\lambda_2)]\,\lambda_1^{\,m}\,\lambda_2^{\,n}\left[\left(\lambda_1^{\,2}-1\right)\left(\lambda_2^{\,2}-1\right)\right]^{\frac{\nu}{2}}P_\tau^{\,N}\begin{pmatrix}\lambda_1\\ \lambda_2\end{pmatrix}Q_\tau^{\,N}\begin{pmatrix}\lambda_2\\ \lambda_1\end{pmatrix}d\lambda_1\,d\lambda_2$$

$$=\int_1^\infty d\lambda_1\int_1^{\lambda_1}d\lambda_2\,\exp[-2\alpha(\lambda_1+\lambda_2)]\left(\lambda_1^{\,m}\,\lambda_2^{\,n}+\lambda_1^{\,n}\,\lambda_2^{\,m}\right)\left[\left(\lambda_1^{\,2}-1\right)\left(\lambda_2^{\,2}-1\right)\right]^{\frac{\nu}{2}}P_\tau^{\,N}\left(\lambda_2\right)Q_\tau^{\,N}\left(\lambda_1\right)$$

$$f(\nu,N)=\int_{-\pi}^{\pi}\int_{-\pi}^{\pi}\cos^\nu\left(\varphi_1-\varphi_2\right)\cos N\left(\varphi_1-\varphi_2\right)d\varphi_1\,d\varphi_2$$

(a17)

and $D_\tau^{\,N}$ is given by Eq.(a8). In Eq.(a16), we have two infinite summations, but they actually reduce to finite sums because of the following reasons. It is non-zero only when (1) $\tau\ge N$, from the properties of the Legendre *P* functions, (2) $N\le\nu$ from the property of the function $f(\nu,N)$ and (3) $\tau\le j+\nu$ from the property of $R(\tau,\nu,N,j)$. Further since these variables are all non-negative integers, Eq.(a16) is rewritten as

$$Z(\nu,m,n,j,k,-1)=\sum_{N=0}^{\nu}\sum_{\tau=N}^{\min(j,k)+\nu}D(\tau,N)\,R(\tau,\nu,N,j)\,R(\tau,\nu,N,k)\,H(\tau,\nu,N,m,n,\alpha)\,f(\nu,N)$$

(a18)

where min(*j*,*k*) means the smaller value of *j* and *k*.

The functions appearing in Eqs.(a14) and (a18) are all calculated with Maple program,[19] for example, so that the Hamiltonian integral H_{ij} and the overlap integral S_{ij} are

expressed by a linear combination of $Z(0,m,n,j,k,l)$. Thus, after the diagonalization of the secular equation, $\mathbf{HC} = E\mathbf{SC}$, you obtain the energy E and the coefficient vector $\mathbf{C}$.

Chapter 5
Solving the Schrödinger equation of helium and its isoelectronic ions with the exponential integral (Ei) function in the free iterative complement interaction method

1. Introduction:

As Dirac noted in 1929,[1] the Schrödinger equation (SE),

$$H\psi = E\psi \,, \tag{2}$$

provides a governing principle of chemistry. Therefore, if a general solution of the SE were possible, very accurate prediction of chemical phenomena would have become possible. However, it was simply a dream for over 80 years.

Helium atom was the simplest realistic unsolved system and many studies have been done to obtain essentially exact solutions of the SE. The first important achievement was done by Hylleraas[2] as early as 1929. He employed the function of the form,

$$\psi_{Hylleraas} = \sum_{(abc)}^{6terms} C_{abc} \exp(-\alpha s) s^a t^b u^c \,, \tag{3}$$

where $s \equiv r_1 + r_2$, $t \equiv r_1 - r_2$ and $u \equiv r_{12}$. The indices, *a*, *b*, and *c* are all nonnegative integers and α is a nonlinear parameter. The coefficients C_{abc} were determined by the variational principle and the calculated energy was E = **-2.903** 329 354 a.u., which was different less than 1 kcal/mol from the essentially exact solution now available. Kinoshita[3] improved the Hylleraas wave function by introducing negative powers of *s* in eq.(3). Thakkar and Koga[4] even introduced real numbers for *a*, *b*, and *c* and obtained the energy of E = **-2.903 724 377 034** 03 a.u. with only 100 basis functions.

Several studies pointed out the importance of the logarithmic functions for describing the boundary condition at the three particles coalescence region.[5-7] Frankowski and Pekeris performed the variational calculations using the logarithmic functions and showed a good convergence of the energies of the two-electron atoms as a support to the existence of the logarithmic terms in the exact wave function.[8] Freund *et al.* applied the logarithm basis to the helium isoelectronic ions and obtained quite accurate energies.[9] They concluded the importance of using the basis functions that have the same analytic structure as the exact wave function. More recently, Schwartz[10] performed quite extensive variational calculations based on the wave functions written as

$$\psi_{Schwarts} = \sum_{(abcd)}^{10259terms} C_{abcd} \exp(-\alpha s) \left[\ln(s)\right]^d s^a t^b u^c \,, \tag{4}$$

where *d* is 0 or 1, and obtained very accurate energy correct up to 36 digits. There are many other important studies on the helium and isoelectronic ions[11-17] and one may refer to our recent paper.[16]

In our laboratory, we have studied since 2000 the structure of the exact wave function and investigated the general method of solving the SE.[18] Overcoming the singularity problem caused by the Coulomb potentials of atomic and molecular Hamiltonians, we could have established the general method of solving the SE and proposed the free ICI (iterative complement interaction) method.[19] It was proved that the ICI wave function becomes exact at convergence.[18-20] Several applications have been reported since then.[21-23] In particular, we have applied the free ICI method to helium and its isoelectronic ions.[16] We have shown that the free ICI method generates the wave function of the form,

$$\psi = \sum_{(abcd)}^{22709 terms} C_{abcd} \exp(-\alpha s)\left[\ln(s+u)\right]^d s^a t^b u^c , \qquad (5)$$

when we start from the initial wave function of the logarithmic form, $\exp(-\alpha s)\ln(s+u)$. We have shown that the use of the logarithmic function as the initial function of the free ICI formalism gives fast convergence, and obtained the energy, E = **−2.903 724 377 034 119 598 311 159 245 194 404 446 696 9**05 37 a.u. that is correct over 40 digits, which was the world

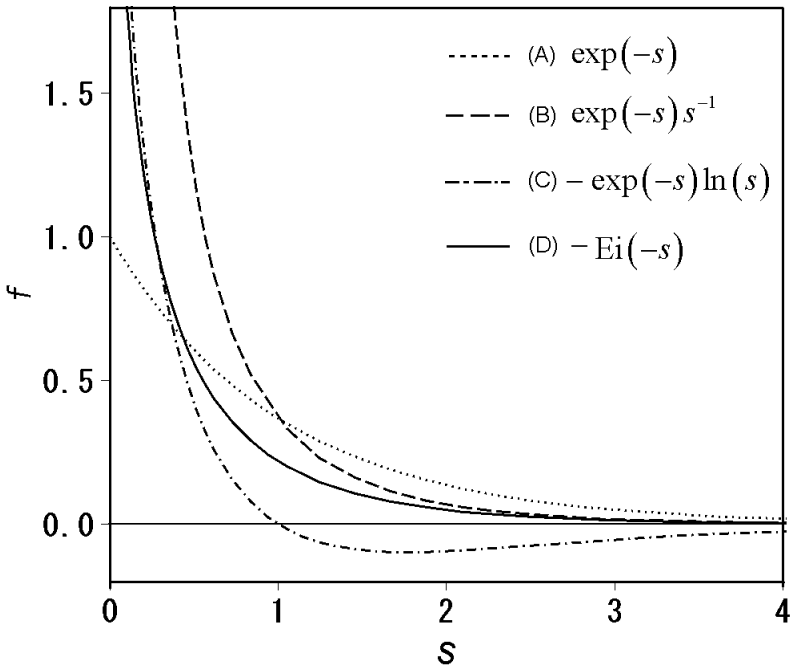

Figure 5-1. Graphs of (A) Slater type (dot line), (B) Kinoshita type (dashed line), (C) logarithm type (dash and dot line), and (D) Ei type (solid line) functions. The logarithm type function has a node at *s* = 1 and a maximum (minimum with minus sign) at *s* = 1.763….

best within the published literatures. Similar accuracy was also obtained with the calculations that include the effect of nuclear motion as well as the electronic ones.[24] Excited states of the two-electron atoms were also calculated quite accurately with the free ICI formalism.[25] These data may be regarded as a numerical proof of the fact that one can obtain the energy and the wave function to any desired accuracy by using the free ICI methodology.

Let us examine several functions that were used to describe the wave function. Fig. 5-1 shows the plots of the Slater type function, $\exp(-s)$, Kinoshita function, $\exp(-s)s^{-1}$, and the logarithmic function, $-\exp(-s)\ln(s)$. At the limit of s = 0, the Slater type function has a finite cusp value but the Kinoshita function and the logarithmic function become infinite. These divergences are the essential behaviors from the three-particle coalescence boundary conditions.[5-7] However, the logarithmic function has the following two strange behaviors: a node at s = 1 and a maximum (minimum with minus sign) around s = 1.763, as shown in Fig. 5-1. These properties look unphysical for the ground state of the helium atom because the 1s orbital smoothly decreases to zero as $s \to \infty$ with neither a node nor a maximum. Therefore, the logarithmic functions must be improved, at least, for these unphysical behaviors.

In the present paper, we introduce exponential integral (Ei) function as a new type of function that improves these behaviors of the logarithmic function. In the next section, we summarize the properties of the Ei function and in Section 3, the free ICI method is briefly explained. In Section 4, the applications of the free ICI method starting from the Ei function are described for helium and its isoelectronic ions and the concluding remarks are given in the last section.

2. The Eexponential Integral Function, Ei

In this section, the mathematical definition and some formulas about the Ei function are summarized very briefly. For more details, one may refer to the mathematical books.[26-28]

The Ei function is defined for real x by an integral form as

$$\mathrm{Ei}(-x) \equiv \int_{-\infty}^{-x} \frac{\exp(t)}{t}\, dt \,. \qquad (6)$$

We treat only positive x in the present study, and so the evaluation of the Ei function is straightforward. In the region of x being negative, which does not occur in our case, eq.(6) must be evaluated in terms of the Cauchy principal value. The plot of the Ei function is shown in Fig. 5-1. It is similar to the logarithmic function, but does not have the strange behaviors of the logarithmic function as described in the introduction. The Ei function can be generalized and extended to an entire complex plane as

$$\mathrm{Ei}(m,z) \equiv \int_1^\infty \frac{\exp(-zt)}{t^m}\,dt\,, \tag{7}$$

where m is an integer and z is a complex number. This function is named m-argument Ei function. In the case of $x > 0$ and $m = 1$, eq.(7) is related to eq.(6) as

$$\mathrm{Ei}(-x) = -\mathrm{Ei}(1,x)\,. \tag{8}$$

The Ei functions with $m = 2, 3, \ldots$ have finite values at $x = 0$. Since their behaviors are very similar to the exponential function, we do not treat them in the present study. Hereafter we deal with the Ei function given by eq.(6) alone.

The Ei function is expandable in power series as

$$\mathrm{Ei}(-x) = \gamma + \ln(x) - \exp(-x)\sum_{n=1}^{\infty} C_n x^n \tag{9}$$

with

$$C_n = \frac{1}{n!}\left(\sum_{r=1}^{n}\frac{1}{r}\right), \tag{10}$$

where $\gamma = 0.5772\cdots$ is the Gamma constant.[28] Eq.(9) is called Bessel's expansion formula. According to eq.(9), Ei(-x) contains ln(x), which becomes dominant at the region of x being very small. Ei(-x) diverges at $x = 0$ to minus infinity,

$$\lim_{x\to+0}\mathrm{Ei}(-x) = -\infty\,, \tag{11}$$

but the following integrals exist:

$$\int_0^\infty \mathrm{Ei}(-x)\,dx = -1\,, \tag{12}$$

$$\int_0^\infty \mathrm{Ei}(-x)^2\,dx = 2\ln(2)\,. \tag{13}$$

Further, the difference between the two Ei functions at $x = 0$ is finite as

$$\lim_{x\to+0}\left[\mathrm{Ei}(-\alpha x) - \mathrm{Ei}(-\beta x)\right] = \ln(\alpha) - \ln(\beta)\,, \tag{14}$$

where $\alpha > 0$ and $\beta > 0$. Similarly, the difference between the Ei function and the logarithmic function at $x = 0$ is finite as

$$\lim_{x\to+0}\left[\mathrm{Ei}(-\alpha x) - \exp(-\alpha x)\ln(\beta x)\right] = \gamma + \ln\left(\frac{\alpha}{\beta}\right). \tag{15}$$

The differentiations of both sides of eq.(15) lead to

$$\lim_{x\to+0}\left[\frac{d}{dx}\mathrm{Ei}(-\alpha x)\right]=\lim_{x\to+0}\left[\frac{d}{dx}\exp(-\alpha x)\ln(\beta x)\right], \tag{16}$$

which indicates that the derivatives of the Ei and the logarithmic functions at $x=0$ are identical. On the other hand, the limit of Ei(-x) at $x=\infty$ is zero,

$$\lim_{x\to\infty}\mathrm{Ei}(-x)=0. \tag{17}$$

The differentials of the Ei function are possible as follows:

$$\frac{d}{dx}\mathrm{Ei}(-x)=\frac{\exp(-x)}{x} \tag{18}$$

and

$$\frac{d^2}{dx^2}\mathrm{Ei}(-x)=-\frac{\exp(-x)}{x}-\frac{\exp(-x)}{x^2}. \tag{19}$$

Eq.(18) is confirmed from eq.(6). Since the first derivative of Ei(-x) is always positive and becomes zero at $x=\infty$, it has no maximum and no nodes. These are the differences from the logarithmic function, $\ln(x)\exp(-x)$, as seen from Fig. 5-1. The indefinite integral of Ei(-x) is derived from eq.(6) by the integration by parts as:

$$\int \mathrm{Ei}(-x)\,dx=x\,\mathrm{Ei}(-x)+\exp(-x). \tag{20}$$

3. Free ICI (iterative complement interaction) Method

In this section, we briefly explain the free ICI method[19,20] to be pertinent to the present study. The simplest form of the ICI wave function is defined by the recursion formula given by

$$\psi_{n+1}=\left[1+C_n g\left(H-E_n\right)\right]\psi_n, \tag{21}$$

where n is an iteration number, $C^{(n)}$ the variational parameter, and E_n the energy defined by

$$E_n\equiv\frac{\langle\psi_n|H|\psi_n\rangle}{\langle\psi_n|\psi_n\rangle}. \tag{22}$$

The g function is the scaling function that was introduced to eliminate the singularity problem caused by the integrals of the higher-powers of the Hamiltonian including Coulomb singularities.[19,20] The initial function ψ_0 can be chosen freely if it satisfies the given conditions such as the spatial symmetry, spin multiplicity, *etc*. Once g and ψ_0 are given, the ICI calculations proceed automatically and the wave function is improved systematically

toward the exact wave function.

The free ICI method was proposed[19, 20] to accelerate the convergence to the exact solution and to increase the freedom of the ICI calculations. The r.h.s. of eq.(20) consists of a sum of the analytical functions. We gather from them all the independent functions as $\left\{\phi_i^{(n)}\right\}$, $\left(i=1,2,\cdots M_n\right)$ and make up our wave function by a linear combination of them as

$$\psi_{n+1}=\sum_{i=1}^{M_n} c_i^{(n)}\phi_i^{(n)}\,, \tag{23}$$

where $c_i^{(n)}$ is the variational parameter assigned to $\phi_i^{(n)}$. This is the free ICI wave function. Because of the increased freedom, the free ICI wave function converges faster than the original ICI wave function to the exact one. The variational parameters, $c_i^{(n)}$, are determined by solving the generalized eigenvalue problem,

$$\mathbf{H}^{(n)}\mathbf{C}^{(n)}=E_n\mathbf{S}^{(n)}\mathbf{C}^{(n)}\,, \tag{24}$$

where $\mathbf{H}^{(n)}$ and $\mathbf{S}^{(n)}$ are the Hamiltonian and the overlap matrices, respectively, given by $\mathbf{H}_{ij}^{(n)}\equiv\left\langle\phi_i^{(n)}\middle|H\middle|\phi_j^{(n)}\right\rangle$ and $\mathbf{S}_{ij}^{(n)}\equiv\left\langle\phi_i^{(n)}\middle|\phi_j^{(n)}\right\rangle$. In the free ICI method, we call *n* as "order" instead of "iteration number", since ψ_n does not depend on the former coefficients $\left\{c_i^{(n-1)}\right\}$, etc. The key point of the ICI formalism is that the exact wave function of a system is constructed by the Hamiltonian itself of the system, i.e., $\psi=f(H)\psi_0$, and eq.(20) or (22) gives an expression of this equation in an analytical expansion form.

4. Applications to Helium and Its Isoelectronic Ions

4.1. Free ICI Formalism

Our goal is to solve the SE of the ground state of the helium atom and its isoelectronic ions with the free ICI method. The Hamiltonian is represented in the Hylleraas coordinate as

$$\begin{aligned}\hat{H}=&-\left(\frac{\partial^2}{\partial s^2}+\frac{\partial^2}{\partial t^2}+\frac{\partial^2}{\partial u^2}\right)-2\frac{s(u^2-t^2)}{u(s^2-t^2)}\frac{\partial^2}{\partial s\partial u}-2\frac{t(s^2-u^2)}{u(s^2-t^2)}\frac{\partial^2}{\partial u\partial t}\\&-\frac{4s}{s^2-t^2}\frac{\partial}{\partial s}-\frac{2}{u}\frac{\partial}{\partial u}+\frac{4t}{s^2-t^2}\frac{\partial}{\partial t}-\frac{4sZ}{s^2-t^2}+\frac{1}{u}\end{aligned}\,, \tag{25}$$

where *Z* is the nuclear charge. As the *g* function, we used

$$g=1+\frac{s^2-t^2}{s}+u\,, \tag{26}$$

which showed the best performance in our previous study.[16] The choice of the initial function ψ_0 is important since it determines the functional form of the free ICI wave function and this

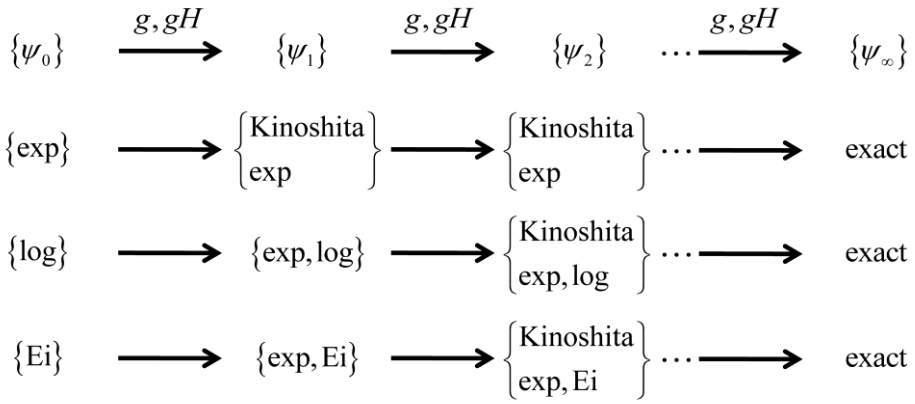

Figure 5-2. Schemes of the basis function generations in the ICI method starting from different types of $\{\psi_0\}$. {exp} type basis function represents $\exp(-\alpha s)s^a t^b u^c$ with *a* being positive or zero, {Kinoshita} type basis function represents $\exp(-\alpha s)s^a t^b u^c$ with *a* being negative, {log} type basis function represents $\exp(-\alpha s)\ln(s)s^a t^b u^c$, and {Ei} type basis function represents $\mathrm{Ei}(-\alpha s)s^a t^b u^c$.

is our major concern of the present paper. First, we propose here to choose the Ei function, i.e.,

$$\psi_0 = \mathrm{Ei}(-\alpha s), \tag{27}$$

where α is a kind of screening parameter. Our second choice is

$$\psi_0 = \mathrm{Ei}(-\alpha s)\left[1+\ln(u)\right], \tag{28}$$

which includes the $\ln(u)$ function as an explicitly correlated factor that was introduced to accelerate the convergence. The $\ln(u)$ function was first introduced in our previous paper[16] and showed very good performance in spite of its simplicity. To compare the performance of the Ei function, we referred to the four different types of calculations that were taken from the previous paper:[16] First, starting from the standard Slater type function given by

$$\psi_0 = \exp(-\alpha s), \tag{29}$$

second starting from the logarithmic function of the *s* coordinate with exponential function,

$$\psi_0 = \exp(-\alpha s)\left[1+\ln(s)\right], \tag{30}$$

third starting from the logarithmic function of *s* and correlated *u* coordinates with exponential function,

$$\psi_0 = \exp(-\alpha s)\left[1+\ln(s)+\ln(u)\right], \tag{31}$$

and finally, starting from the function that includes *s* and *u* coordinates in the same logarithm function as

$$\psi_0 = \exp(-\alpha s)\left[1+\ln(s+u)\right]. \tag{31}$$

The last one produced the best energy in our previous study. [16]

The wave functions that are generated by the free ICI formalism using the above g and the Ei type initial functions ψ_0 (eqs.(27) and (28)) are represented by

$$\psi = \sum_{(\mu\nu lmn)} C_{\mu\nu lmn}\left[\nu\exp(-\alpha s)+(1-\nu)\mathrm{Ei}(-\alpha s)\right]\left[\ln(u)\right]^{\mu} s^a t^b u^c , \qquad (32)$$

where ν, μ, a, b and c are integers, ν and μ take either 0 or 1. For the ψ_0 of eq.(26), μ is always zero. As seen from eq.(18), the exponential type function is automatically generated from the differentiation of the Ei function. On the other hand, when one performs the free ICI calculations with the usual exponential and logarithmic ψ_0 given by eqs.(29), (30), and (31), one obtains the wave functions that are represented by

$$\psi = \sum_{(\mu\nu lmn)} C_{\mu\nu lmn}\exp(-\alpha s)\left[\ln(u)\right]^{\mu}\left[\ln(s)\right]^{\nu} s^a t^b u^c , \qquad (33)$$

where ν, μ, a, b, and c are integers and the quantity $\nu+\mu$ takes 0 or 1. The wave function generated with ψ_0 of eq.(31) was already given in eq.(4). The Ei part of eq.(32) can be expanded using the Bessel's expansion formula given by eq.(9), and then the wave function given by eq.(33) can be reformulated into the same forms as eq.(32), though the details are different at finite order of the free ICI. When the order reaches infinity, the quantities ν, μ, a, b, and c take all the patterns in both cases of eqs.(32) and(33), and therefore, these two wave

Table 5-1. Energy of helium atom calculated by the free ICI method with the initial function $\psi_0 = \mathrm{Ei}(-\alpha s)$ (eq.(27)), the first and second derivatives of the energy with respect to the parameter α and the best estimated value of α.

n[a]	M_n[b]	α	Energy E (a.u.)	E-E_{best}	$\partial E/\partial a$[d]	$\partial^2 E/\partial a^2$[e]	Best α[f]
0	1	1.6	**-2.**425 758 617 410 142 390	4.78×10^{-1}	1.74×10^{0}	$2.04\mathrm{E}\times10^{0}$	1.172
1	7	1.6	**-2.90**0 008 689 031 112 995	3.72×10^{-3}	1.01×10^{-3}	8.55×10^{-2}	1.594
2	22	1.6	**-2.903** 376 336 198 933 179	3.48×10^{-4}	2.05×10^{-3}	4.24×10^{-3}	1.359
3	61	1.6	**-2.903 72**3 729 740 132 823	6.47×10^{-7}	1.06×10^{-6}	1.20×10^{-5}	1.556
4	111	1.6	**-2.903 724 3**58 079 515 735	1.90×10^{-8}	1.34×10^{-8}	1.33×10^{-7}	1.550
5	188	1.6	**-2.903 724 37**6 475 282 897	5.59×10^{-10}	1.23×10^{-10}	1.48×10^{-9}	1.559
6	310	1.6	**-2.903 724 377 0**17 385 340	1.67×10^{-11}	7.49×10^{-13}	1.03×10^{-11}	1.564
7	505	1.6	**-2.903 724 377 03**3 617 731	5.02×10^{-13}	7.52×10^{-15}	7.80×10^{-14}	1.552
8	697	1.6	**-2.903 724 377 034 1**04 549	1.50×10^{-14}	6.54×10^{-17}	6.35×10^{-16}	1.548
9	919	1.6	**-2.903 724 377 034 119** 147	4.51×10^{-16}	5.37×10^{-19}	5.53×10^{-18}	1.551
	E_{best}[c]		**-2.903 724 377 034 119 598**				

a: Order of the free ICI.
b: Number of the complement functions.
c: Ref. 16
d: The approximate first derivative at α= 1.6 calculated from the quadratic interpolation of the energies at α=1.5, 1.6 and 1.7.
e: The approximate second derivative at α= 1.6 calculated from quadratic interpolation of the energies at α=1.5, 1.6 and 1.7.
f: Variationally best α estimated from the interpolated quadratic curve.

functions will become identical. The Kinoshita type terms (including negative powers of *s*) are also automatically generated in both types of the wave functions.[19,20] In Fig. 5-2, we summarized the function generation schemes of the free ICI method starting from different initial functions ψ_0.

4.2. Computational Details

The generations of the free ICI functions and the evaluations of the matrix elements for eq.(24) were performed with an algebraic mathematical package, *Maple 10*.[29] The diagonalization of the secular equation represented by eq.(24) was performed by our original solver using the *GMP* library.[30] Both enabled us to perform the calculations to any precisions. In most calculations, we set the precision of the calculations to be 60 digits. However, in Sec.4.6, we will perform extensive calculations to very large order *n* of the free ICI and there, we set the precision to be 160 digits to avoid numerical instability.

4.3. Lower Order Calculations of Helium Atom Starting From the Ei Function

The energy of the initial function of eq.(27) with α = 1.6 is E_0 = -**2**.425 758 617 410 142 390 a.u. This value was improved toward the exact one in the subsequent increased order *n*, as shown in Table 5-1. We performed the same calculations with α=1.5 and 1.7, and estimated the optimal α value as shown in Table. 5-1. We also calculated approximately the derivatives

Table 5-2. Energy of helium atom calculated by the free ICI method with the initial function $\psi_0 = \exp(-\alpha s)$ (eq. (29)) and $\psi_0 = \exp(-\alpha)\left[1+\ln(s)\right]$ (eq. (30)). This table is taken from ref. 16.

	$\psi_0 = \exp(-\alpha s)$			$\psi_0 = \exp(-\alpha)\left[1+\ln(s)\right]$		
n[a]	M_n[b]	α	Energy E (a.u.)	M_n[b]	α	Energy E (a.u.)
0	1	1.688	−**2**.847 656 250 00	2	1.687	−**2**.847 656 242 128 24
1	4	1.689	−**2.90**1 337 956 94	10	1.550	−**2.90**2 964 172 868 10
2	16	1.736	−**2.903** 642 984 26	34	1.561	−**2.903** 702 734 675 68
3	37	1.779	−**2.903 72**0 264 20	77	1.619	−**2.903 72**3 749 601 90
4	71	1.837	−**2.903 724** 018 70	146	1.638	−**2.903 724 3**58 395 41
5	121	1.92	−**2.903 724 3**23 45	247	1.641	−**2.903 724 37**6 476 31
6	190	1.995	−**2.903 724 3**64 00	386	1.651	−**2.903 724 377** 01 739
7	281	2.083	−**2.903 724 37**3 59	569	1.670	−**2.903 724 377 03**3 61
8	397	2.161	−**2.903 724 37**5 90	802	1.683	−**2.903 724 377 034 1**04 549
9	541	2.251	−**2.903 724 37**6 66	1091	1.696	−**2.903 724 377 034 119** 147
		E_{best}[c]	**-2.903 724 377 034**			

a: Order of the free ICI.
b: Number of the complement functions.
c: Ref. 16

Table 5-3. The free ICI wave function at first order starting from the initial function, $\psi_0 = \mathrm{Ei}(-\alpha s)$ (eq. (27)) , (n=1, M_1=7 and α =1.6).

Coefficient	Complement function	Coefficient	Complement function
1.000000000	$\exp(-\alpha s)$	-0.5860458840	$\mathrm{Ei}(-\alpha s)s$
-0.1312519886	$\exp(-\alpha s)s^{-1}u$	0.0992782326	$\mathrm{Ei}(-\alpha s)s^{-1}t^2$
-0.0697537604	$\exp(-\alpha s)s^{-2}t^2$	0.2737850022	$\mathrm{Ei}(-\alpha s)u$
-0.0368809315	$\mathrm{Ei}(-\alpha s)$		

a: Each complement function is normalized to unity but the total wave function is not normalized. The coefficients are the relative values to the one of $\exp(-\alpha s)$.

$\partial E/\partial\alpha$ and $\partial^2 E/\partial\alpha^2$, which indicate the sensitivity of the energy with respect to the parameter α. From these quantities, we calculated the estimated best values of α, though all the calculations were done with the fixed value of $\alpha = 1.6$. For comparison, Table 5-2 shows the energies of the free ICI calculations starting from the ordinary Slater type function of eq.(29) and from the one including the logarithmic function of eq.(30): these data are taken from our previous paper of ref. 16. Note that the screening parameter, α, in Tables 5-2 was optimized at each order.

At order 9 (n = 9), 919 complement functions were generated from the Ei-type initial function given by eq.(27) and the corresponding energy was E_9 = **-2.903 724 377 034 119** 147 a.u., which has 16 digits accuracy. On the other hand, at n=9, 541 functions were generated from the initial function of eq.(29) and 9 digits accuracy was obtained: almost the same accuracy was obtained already at n = 5 (M_5 = 188) with the Ei case. In comparison with the calculations using the logarithmic initial function of eq.(30), the energy of the Ei case was almost the same at each order but the number of the complement functions was always smaller in the Ei case than in the logarithmic case. As seen in Table 5-1, the energy derivatives with respect to the screening parameter α, approached zero as the order increases, and therefore at large n, a small change in α little influenced the energy. The estimated best value of α seemed to converge to the constant around 1.55. This suggests that only linear parameters must be optimized as variational parameters and that the scaling parameter α may not really be the variational parameter but the quantity related to the physical property like ionization energy.[31] In principle, the free ICI formalism does not require the optimization of the non-linear parameters.[19,20] On the other hand, the optimal α of the exponential type function (eq.(29)) shown in Table 5-2 increased as the order increased and did not yet show a sign of the convergence.

At first order, seven complement functions were generated and they were listed in Table 5-3 together with their optimized coefficients. There, the function, $\phi_1^{(1)} = \exp(-\alpha s)$, that is identical to eq.(29), is included. Therefore, afterwards, the free ICI method generates

Table 5-4. Energy of helium atom calculated by the free ICI method with the initial function $\psi_0 = \mathrm{Ei}(-\alpha s)\left[1+\ln(u)\right]$ (eq.(28)), the derivatives with respect to α and the best estimated α.

n[a]	M_n[b]	α	Energy E (a.u.)	E-E_{best}	$\partial E/\partial\alpha$ [d]	$\partial^2 E/\partial\alpha^2$ [e]	Best α[f]
0	2	1.6	**-2.**666 888 282 498 509 506	2.37×10^{-1}	1.06×10^{0}	$1.57\mathrm{E}\times10^{0}$	1.262
1	14	1.6	**-2.90**2 295 055 973 125 945	1.43×10^{-3}	2.67×10^{-3}	1.97×10^{-2}	1.532
2	44	1.6	**-2.903** 640 326 345 850 979	8.41×10^{-5}	8.06×10^{-4}	2.46×10^{-3}	1.436
3	122	1.6	**-2.903 724 37**6 098 371 470	9.36×10^{-10}	1.52×10^{-8}	1.95×10^{-7}	1.561
4	222	1.6	**-2.903 724 377 0**21 228 247	1.29×10^{-11}	3.19×10^{-10}	3.35×10^{-9}	1.552
5	376	1.6	**-2.903 724 377 034** 097 813	2.18×10^{-14}	1.67×10^{-12}	1.72×10^{-11}	1.551
6	620	1.6	**-2.903 724 377 034 119** 430	1.68×10^{-16}	2.14×10^{-16}	3.65×10^{-15}	1.571
7	1010	1.6	**-2.903 724 377 034 119 59**5	2.65×10^{-18}	-3.82×10^{-20}	1.73×10^{-18}	1.611
	E_{best}[c]		**-2.903 724 377 034 119 598**				

a: Order of the free ICI.
b: Number of the complement functions.
c: Ref. 16
d: The approximate first derivative at α = 1.6 calculated from the quadratic interpolation of the energies at α =1.5, 1.6, and 1.7.
e: The approximate second derivative at α = 1.6 calculated from quadratic interpolation of the energies at α =1.5, 1.6, and 1.7.
f: Variationally best α estimated from the interpolated quadratic curve.

from this function the same series of complement functions as those that are generated from the starting function of eq.(29). This implies that the difference between the n-th order result of Table 5-1 and the (n-1)-th order result of Table 5-2 are the improvement due to the Ei type functions.

As shown above, the Slater type function is generated from the Ei function by applying the Hamiltonian operator according to eq.(21). This suggests that conversely the Ei function is generated by applying the inverse operator, H^{-1}, to the Slater type function. In Fig. 5-2, the inverse operation corresponds to generating functions from right to left direction. According to the linear algebraic formalism, quadratic convergence may be obtained with the inverse iteration method. Previously, one of the authors[32] applied the inverse Hamiltonian method to solve the SE of hydrogen atom and obtained a faster convergence than the regular Hamiltonian case. If we regard the Ei functions and the logarithmic functions to be generated by applying the inverse Hamiltonian operator to the exponential function, we may be able to understand an aspect of the origin of their fast convergence.

Table 5-4 shows the free ICI energy starting from the Ei function with the explicitly correlated term given by eq.(28) with α= 1.6. We performed the same calculation with α = 1.5 and α = 1.7 and calculated the approximate first and second derivatives of the energy with respect to the screening parameter α and the best estimated α, which are also shown in Table

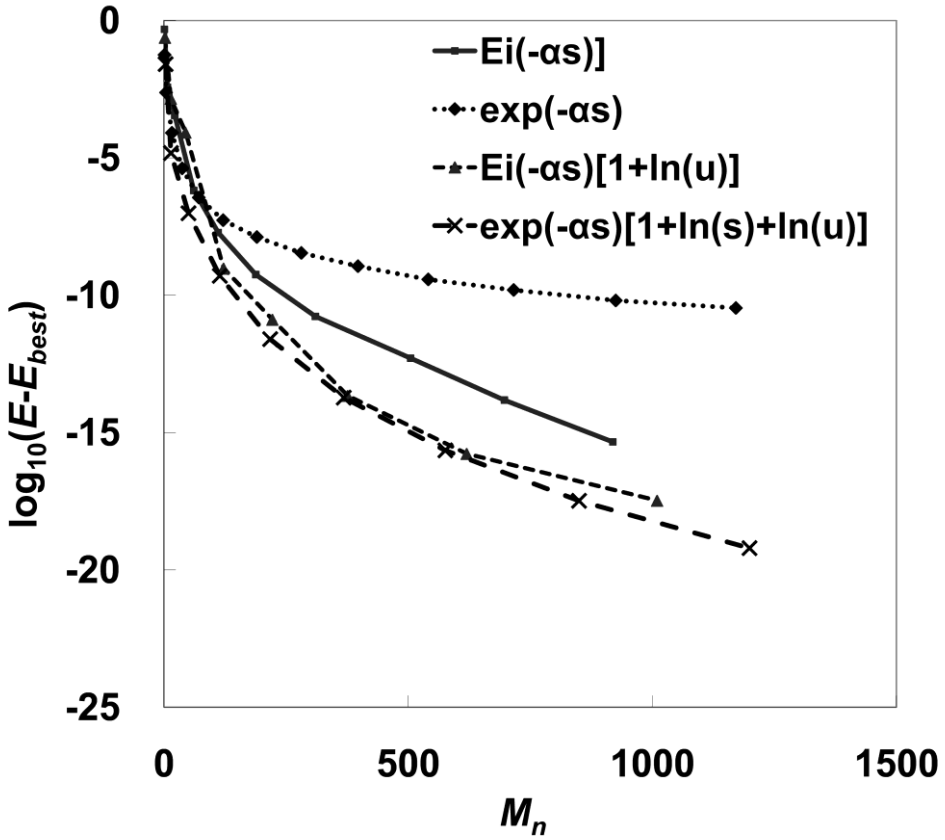

Figure 5-3. Energy convergence of the free ICI calculations with different types of initial functions, $\psi_0 = \mathrm{Ei}(-\alpha s)$ (solid line) (eq.(27)), $\psi_0 = \exp(-\alpha s)$ (dot line) (eq.(29)), $\psi_0 = \mathrm{Ei}(-\alpha s)[1+\ln(u)]$ (short dashed line) (eq.(28)), and $\psi_0 = \exp(-\alpha s)[1+\ln(s)+\ln(u)]$ (long dashed line) (eq.(31)). E_{best} is estimated to be the so-far best value, E = -2.903 724 377 034 119 598 311 159 245 194 404 446 696 9 a.u. obtained in ref.16.

5-4.

Fig. 5-3 shows the convergence speeds of the free ICI calculations starting from the four types of the initial functions given by eqs. (27), (28), (29), and (31). The logarithms of the energy differences from the so-far best value, E = -2.903 724 377 034 119 598 311 159 245 194 404 446 696 9 a.u.,[16] were plotted there. The convergence speed of the free ICI calculations starting from the Ei type function, given by eq.(28), was poor in the initial stage, but as the order increases, it became similar to that of eq.(31). The energy derivatives with respect to α approached zero as the order increased, but the best estimated value slightly increased in a oscillating manner. Similar behavior was also seen for the case starting from eq.(31).

We will give below the extensive calculations of helium atom starting from the Ei function of eq.(26) up to the order n = 27, but before that, we give the results for the helium isoelectronic ions.

Table 5-5. Energy of the helium isoelectronic ions calculated by the free ICI method with the initial function $\psi_0 = \mathrm{Ei}(-\alpha s)\left[1+\ln(u)\right]$ (eq.(28)) and a comparison with the energy obtained by Freund *et al.*[c] using the logarithm type functions.

		Free ICI results with Ei type function[a]		Logarithm type function[c]	
Character	Z	α[b]	Energy (a.u.)	α[b]	Energy (a.u.)
H	1	0.4477	-0.527 750 970 358 127	0.390	-0.527 751 015 3
He	2	1.550	-2.903 724 377 026 498	1.600	-2.903 724 377 034 0
Li	3	2.520	-7.279 913 412 662 821	2.820	-7.279 913 412 669 2
Be	4	3.493	-13.655 566 238 414 004	3.840	-13.655 566 238 423 5
B	5	4.365	-22.030 971 580 230 969	4.850	-22.030 971 580 242 7
C	6	5.300	-32.406 246 601 884 841	5.880	-32.406 246 601 898 4
N	7	6.288	-44.781 445 148 757 529	6.930	-44.781 445 148 772 6
O	8	7.162	-59.156 595 122 741 245	8.000	-59.156 595 122 757 8
F	9	7.852	-75.531 712 363 926 577	9.000	-75.531 712 363 959 4
Ne	10	9.116	-93.906 806 515 019 002	10.00	-93.906 806 515 037 4

a: The order is four, the number of the complement function is 222, and the initial function is $\psi_0 = \mathrm{Ei}(-\alpha s)\left[1+\ln(u)\right]$ (eq. (28)).

b: The screening parameter optimized at each ion.

c: The results of Freund *et al.*, taken from ref. 9. The wave function has the form of $\psi = \sum_{(abc)}^{230 terms} C_{abc} \exp(-\alpha s)\ln(s) s^a t^b u^c$.

4.4. Application to Helium Isoelectronic Ions

Here, we show briefly the results for the helium isoelectronic ions, represented as $M^{(Z-2)+}$ (Z = 1,2,3,…,10), starting from the Ei function with the explicitly correlated term given by eq.(28). The free ICI was done only up to order four (n = 4, M_4 = 222) and the value of α was optimized for each ion. The results are shown in Table 5-5, where the energies calculated by Freund *et al.*[9] using 230 logarithmic basis functions are also shown. We could obtain more than 11 digits accuracy for all ions except for the hydride ion H^-. More accurate energies of these ions were published in our previous paper.[16]

As Freund *et al.* noted, electrons of the hydride ion exist rather far from the nucleus, however, the logarithmic functions are suited for describing electrons near the nucleus. Therefore, it would be difficult to describe such electrons in high accuracy by using the logarithmic functions. This consideration holds true also for the Ei type wave functions of the present study.

The optimal α of each ion and the nuclear charge Z have a linear relation represented by $\alpha_{opt} = aZ - b$, where a and b were calculated, by the least square fitting, to be 0.9254 and 0.2583, respectively. This result is in accordance with the interpretation of α to be the screening parameter that is related to the ionization potential.

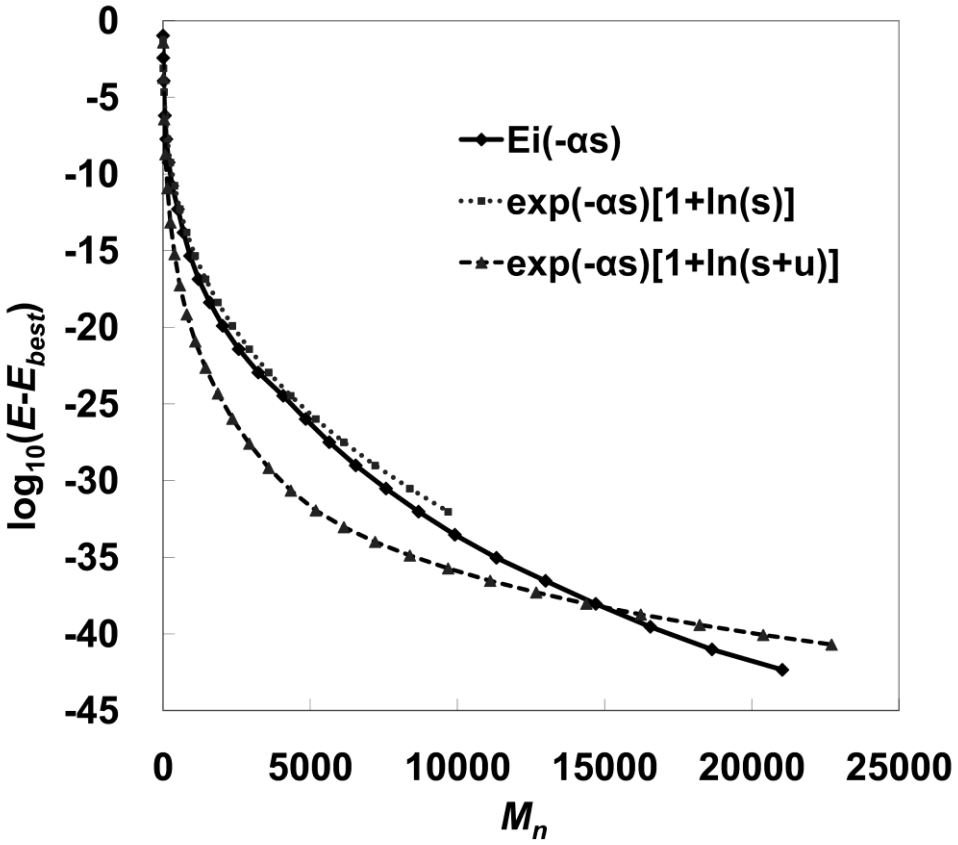

Figure 5-4. Energy convergence of the free ICI calculations with different types of initial functions, $\psi_0 = \mathrm{Ei}(-\alpha s)$ (solid line) (eq.(27)), $\psi_0 = \exp(-\alpha s)[1+\ln(s)]$ (dot line) (eq.(29)), and $\psi_0 = \exp(-\alpha s)[1+\ln(s+u)]$ (dashed line) (eq.(31)). E_{best} is estimated here to be the best value calculated here, E = -2.903 724 377 034 119 598 311 159 245 194 404 446 696 924 865 a.u, which is lower (better) than the value obtained in Ref.16.

4.5. Fully Extensive Calculations of Helium Atom Starting From the Ei Function

Finally, let us report the result of the fully extensive free ICI calculations of the helium atom with the Ei function given by eq.(26). Table 5-6 shows the converging series of energies up to n = 27 and the convergence indicator Δ_n at order n that is the logarithm of the energy difference from the best energy value, for which we adopted the best energy we obtained here at n = 27. The energy at n = 27 (M_{27} = 21035) was E_{27} = **-2.903 724 377 034 119 598 311 159 245 194 404 446 696 924** 865 a.u. which has 43 digits accuracy and variationally improves the best energy of our previous paper[16] for about 2-3 digits in spite of the smaller dimensions in the present case. The α value was fully optimized until n = 16 but the change became small and so from n = 17, α was fixed to 1.6.

Fig. 5-4 shows the energy convergence behaviors of the free ICI energies with ψ_0 given by eqs.(26), (29), and (31): it is a plot of Δ_n against M_n. When we compare the calculations

with ψ_0's of eqs.(26) and eq.(29), one notices that the two energies at the same order *n* are almost same, though the number of the generated functions, M_n is slightly smaller in the Ei case than in the logarithmic case. It suggests that the free ICI functional spaces generating from these two sets are almost the same but the Ei case is slightly more efficient because of the smaller dimension. It also becomes a numerical proof that the three-particle coalescence behavior is satisfactory also with the Ei function because the Ei function includes the logarithm property.

Comparing the Ei case to the calculation with ψ_0 given by eq.(31), the convergence of the latter case is better than the Ei case at small dimensions until about M_n = 14000. The speed of the convergence of the latter case becomes slow down after exceeding that dimension and two

Table 5-6. Energy of helium atom calculated with $\psi_0 = \mathrm{Ei}(-\alpha s)$ (eq.(27)). Δ_n shows the convergent digits defined as $\Delta_n = \log_{10}(E_n - E_{exact})$.

n	M_n	α	Energy (a.u.)	Δ_n
0	1	1.173	**-2.**797 959	-0.98
1	7	1.612	**-2.90**0 021	-2.43
2	22	1.363	**-2.903** 607	-3.93
3	61	1.562	**-2.903 72**3 737	-6.19
4	111	1.547	**-2.903 724** 358 271	-7.73
5	188	1.607	**-2.903 724 37**6 475	-9.25
6	310	1.599	**-2.903 724 377 0**17 385	-10.8
7	505	1.578	**-2.903 724 377 03**3 617	-12.3
8	697	1.576	**-2.903 724 377 034 1**04 549	-13.8
9	919	1.585	**-2.903 724 377 034 119** 147	-15.3
10	1206	1.585	**-2.903 724 377 034 119 5**84 790	-16.9
11	1589	1.591	**-2.903 724 377 034 119 59**7 905	-18.4
12	2027	1.586	**-2.903 724 377 034 119 598** 298 978	-19.9
13	2572	1.595	**-2.903 724 377 034 119 598 31**0 792	-21.4
14	3236	1.588	**-2.903 724 377 034 119 598 311 1**48 179	-23.0
15	4081	1.612	**-2.903 724 377 034 119 598 311 15**8 909	-24.5
16	4845	1.636	**-2.903 724 377 034 119 598 311 159 2**34 996	-26.0
17	5647	(1.6)	**-2.903 724 377 034 119 598 311 159 24**4 882	-27.5
18	6546	(1.6)	**-2.903 724 377 034 119 598 311 159 245 1**84 832	-29.0
19	7573	(1.6)	**-2.903 724 377 034 119 598 311 159 245 194** 108	-30.5
20	8679	(1.6)	**-2.903 724 377 034 119 598 311 159 245 194** 395 279	-32.0
21	9912	(1.6)	**-2.903 724 377 034 119 598 311 159 245 194 404** 160	-33.5
22	11326	(1.6)	**-2.903 724 377 034 119 598 311 159 245 194 404 4**37 749	-35.0
23	12994	(1.6)	**-2.903 724 377 034 119 598 311 159 245 194 404 446** 415	-36.6
24	14699	(1.6)	**-2.903 724 377 034 119 598 311 159 245 194 404 446 6**88 045	-38.1
25	16552	(1.6)	**-2.903 724 377 034 119 598 311 159 245 194 404 446 696** 642	-39.5
26	18646	(1.6)	**-2.903 724 377 034 119 598 311 159 245 194 404 446 696 9**15 844	-41.0
27	21035	(1.6)	**-2.903 724 377 034 119 598 311 159 245 194 404 446 696 924** 865	(-42.5)[a]
Ref. 16	22709		**-2.903 724 377 034 119 598 311 159 245 194 404 446 696 9**05 34	-40.7

a: The value presumed from the convergent behavior.

cases become almost equivalent at M_n = 14000 and the Ei case becomes faster at M_n>14000. The speed of the convergence does not become worse in the Ei case even at a very large dimension over M_n = 20000 and its plot of Δ_n in Fig. 5-4 is almost linear (a bit downward convex). Thus, although the most rapid convergence in M_n<14000 is obtained with ψ_0 given in eq.(31), i.e. the logarithmic form, the fastest convergence at very high dimension is obtained with the ψ_0 of the Ei function, eq.(26). This nice property would be due to the better behaviors of the Ei function over the logarithmic function as shown in Fig. 5-1

5. Conclusion

We introduced the Ei function as a new type of function that has a physical meaning similar to the logarithmic function, and yet does not show the unphysical behaviors that the logarithmic function shows. We have used here the Ei functions as the starting functions of the free ICI formalism to calculate the accurate wave functions and energies of the helium and its isoelectronic ions. The free ICI wave functions generated from the Ei function showed very good convergence and the speed of the convergence was almost the same as that with the logarithmic function. Further, when we perform highly extensive calculations, the free ICI wave function starting from the Ei function gave a better performance than the one starting from the logarithmic function, reflecting the good behavior of the Ei function in comparison with the logarithmic function. For this reason, we could improve the variational energy of helium atom correct up to about 43 digits.

The natures of these two types of functions are considered to be very similar and with the free ICI formalism, both functions produce identical set of complement functions at infinite orders. The logarithmic function has a node and a maximum, which seems to be unphysical for the ground state of the present system, while the Ei function has neither a node nor a maxima and decreases smoothly to zero. The Ei functions are considered to be suited for describing the electrons near the nucleus like those of inner shell region. The Ei function may also be understood as the function generated by operating the inverse Hamiltonian to the ordinary exponential function and this may be a reason why the Ei functions lead to a fast convergence. The more general functions widely used in the correlated methods like Gaussian function with the Jastrow functions[33,34] are also automatically generated from the Ei-type function, such as $\psi_0 = \exp(-\alpha r^2)\,\mathrm{Ei}\left(ar/(r+b)\right)$ or $\psi_0 = \mathrm{Ei}(-\alpha r^2)\exp\left(ar/(r+b)\right)$. They would be of some values for the general atomic and molecular calculations.

These results may be considered to support that the Ei function is a better function than

the logarithmic function for describing the three particle coalescence region.

The use of the Ei functions for larger atoms and molecules is also very interesting for accurate descriptions of atomic and molecular electronic structures in which the wave function must have the freedom that the exact wave function has in the three-particle coalescence region. Though we used the variation principle (VP) to calculate the variables in the free ICI wave function**,** we have published a method of using the Schrödinger equation directly instead of the variation principle.[35] This local Schrödinger equation (LSE) method is applicable to wider classes of many-electron atoms and molecules than the variation principle.

Acknowledgement

This study has partially been supported financially by a grant for Creative Scientific Research from the Ministry of Education, Science, Culture, and Sports of Japan.

Reference

(1) P. A. M. Dirac, *Proc. R. Soc. London, Ser. A*, **1929**, *123*, 714.

(2) E. A. Hylleraas, *Z. Phys.*, **1929**, *54*, 347.

(3) T. Kinoshita, *Phys. Rev.*, **1957**, ***105***, 1490.

(4) A. J. Thakkar and T. Koga, *Theor. Chem. Acc.*, **2003**, *109*, 36.

(5) J. H. Bartlett, Jr., *Phys. Rev.*, **1937**, *51*, 661.

(6) T. H. Gronwall, *Phys. Rev.*, **1937**, *51*, 655.

(7) V. A. Fock, *Izv. Akad. Nauk SSSR, Ser. Fiz*, **1954**, *18*, 161.

(8) K. Frankowski and C. L. Pekeris, *Phys. Rev.*, **1966**, *146*, 46.

(9) D.E. Freund, B. D. Huxtable, and J. D. Morgan III , *Phys. Rev. A*, **1984**, *29*, 980.

(10) C. Schwartz, *Int. J. Mod. Phys. E*, **2006**, *15*, 877.

(11) H. M. Schwartz, *Phys. Rev.*, **1956**, *103*, 110.

(12) T. Koga, *J. Chem. Phys.*, **1992**, *96*, 1276.

(13) S. P. Goldman, *Phys. Rev. A*, **1998**, *57*, R677.

(14) G. W. F. Drake, M. M. Cassar, and R. A. Nistor, *Phys. Rev. A*, **2002**, *65*, 054501.

(15) V. I. Korobov, *Phys. Rev. A*, **2002**, *66*, 24501.

(16) H. Nakashima and H. Nakatsuji, *J. Chem. Phys.*, **2007**, *127*, 224104.

(17) J. S. Sims and S. A. Hagstrom, *Int. J. Quantum Chem.*, **2002**, *90*, 1600.

(18) H. Nakatsuji, *J. Chem. Phys*, **2000**, *113*, 2949.

(19) H. Nakatsuji, *Phys. Rev. Lett.*, **2004**, *93*, 030403.

(20) H. Nakatsuji, *Phys. Rev. A*, **2005**, *65*, 062110.
(21) H. Nakatsuji, *Bull. Chem. Soc. Jpn.*, **2005**, *78*, 1705.
(22) Y. Kurokawa, H. Nakashima, and H. Nakatsuji, *Phys. Rev. A*, **2005**, *72*, 062502.
(23) H. Nakatsuji and H. Nakashima, *Phys. Rev. Lett*, **2005**, *95*, 050407.
(24) H. Nakashima and H. Nakatsuji, *J. Chem. Phys.*,**2008**, *128*, 154107.
(25) H. Nakashima, Y. Hijikata, and H. Nakatsuji, *J. Chem. Phys.*,**2008**,*128*,154108.
(26) I. S. Gradshteyn and I. M. Ryzhik, *Table of Integrals, Series, and Products* (Academic, New York), **2000**.
(27) M. Abramowitz and I. A. Stegun, *Handbook of Mathematical Functions* (Dover, New York), **1972**.
(28) S. Moriguchi, K. Utagawa, and S. Hitomatsu, *Mathematical Formula III, Special Functions* (Iwanami, Tokyo), **2005**.
(29) Computer code *MAPLE*, Waterloo Maple Inc., Waterloo, Ontario, Canada (see http://www.maplesoft.com/).
(30) About the GMP library, see http://swox.com/gmp/ and http://www.cs.nyu.edu/exact/core/gmp/.
(31) S. H. Patil, *J. Phys. B*, **1990**, *23*, 1.
(32) H. Nakatsuji, *Phys. Rev. A*, **2002**, *65*, 052122.
(33) P. T. A. Galek, N. C. Handy, and W. A. Lester Jr., *Mol. Phys.*, **2006**, *104*, 3069
(34) K. E. Schmidt, J. W. Moskowitz, *J. Chem. Phys.*, **1990**, *93*, 4172
(35) H. Nakatsuji, H. Nakashima, Y. Kurokawa, A. Ishikawa, *Phys. Rev. Lett*, **2007**, *99*, 240402.

General Conclusion

In Part I, the author investigated two kinds of chromium complexes and their analogues. In Chapter 1, the author elucidated the bonding nature of Cr-Cr quadruple bonds. In Chapters 2 and 3, the author investigated the spin multiplicities of the inverted sandwich type complexes. In Part II, the author succeeded in solving the Schrödinger equation of the hydrogen molecule and helium atom without any approximations. The other important conclusions presented in this thesis are summarized as follows:

In Chapter 1, open-lantern type dinuclear Cr(II) complex, $[Cr(R^1NC(R^2)NR^3)_2]_2$ (R^1 = Et, R^2 = Me, and R^3 = ^{t}Bu), was theoretically investigated with DFT, CASSCF, and MRMP2 methods. The DFT-optimized Cr-Cr distance (1.757 Å) is too short, compared to the experimental value (1.960 Å). The CASSCF method does not present the minimum in the range of the Cr-Cr distance from 1.75 to 2.05 Å. The MRMP2 method presents the optimized Cr-Cr distance of 1.851 Å, which is a little shorter than the experimental value. These results suggest that both non-dynamical and dynamical correlations are considerably large in this complex. The Cr-Cr bond order is evaluated to be 2.40 with the CASSCF method, which is much smaller than the formal bond order of 4. In the Mo analogue, on the other hand, the DFT, CASSCF, and MRMP2 methods present almost the same Mo-Mo distance (2.151 Å). The Mo-Mo bond order is evaluated to be 3.41, which is somewhat smaller than the formal value but much larger than the Cr-Cr bond order. These differences arise from the much larger d-d overlap integral of the Mo-Mo pair than that of the Cr-Cr pair. Though non-dynamical correlation effect is very large in this dinuclear Cr(II) complex, the Cr-Cr distance of this complex was experimentally discussed to be short, based on formal shortness ratio (*FSR*). The author proposed orbital shortness ratio (*OSR*) based on the distance providing maximum overlap integral to discuss the M-M bond distance. According to the *OSR*, one can understand that the Cr-Cr distance of 1.960 Å is long but the Mo-Mo distance of 2.151 Å is short. This understanding is consistent with much larger non-dynamical correlation in the dinuclear Cr(II) complex than in the Mo(II) analogue. Interesting differences are also

observed between M-M and Si-Si multiple bonds. The differences are discussed in terms of σ- and π-type overlap integrals and the participation of Si 3s orbital in the σ-bonding orbital.

In Chapter 2, inverted sandwich type chromium(I) and vanadium(I) complexes, $(\mu\text{-}\eta^6\text{:}\eta^6\text{-}\ C_6H_5CH_3)[Cr(DDP)]_2$ (DDPH = 2-(4-{(2,6-diisopropylphenyl)imino}pent- 2-ene) and $(\mu\text{-}\eta^6\text{:}\eta^6\text{-}C_6H_5CH_3)[V(DDP)]_2$, synthesized by Tsai *et al.* and $(\mu\text{-}\eta^6\text{:}\eta^6\text{-}C_6H_6)[Cr(DDP)]_2$ synthesized by Monillas *et al.* were theoretically investigated with MRMP2 and DFT methods, where model compounds, $(\mu\text{-}\eta^6\text{:}\eta^6\text{-}C_6H_6)[M(AIP)]_2$ (M = V or Cr; AIPH = (Z)-1-amino-3-imino-prop-1-ene), were mainly employed. Both computational methods succeeded in reproducing the experimental facts that the chromium and vanadium complexes take surprisingly high spin states, septet and quintet spin states, respectively. MO diagrams of these complexes present clear understanding of the reasons why they take such high spin states. The author also calculated their analogues, $(\mu\text{-}\eta^6\text{:}\eta^6\text{-}C_6H_6)[M(DDP)]_2$ (M=Sc, Ti, Mn, or Fe). The spin multiplicities of the Sc and Ti complexes were calculated to be singlet and triplet, respectively, by the DFT(B3LYP) method. Those of Mn and Fe complexes were calculated to be quintet and triplet, respectively, by the DFT(B3LYP) method, but nonet and singlet, respectively, by the MRMP2 method, suggesting that the DFT method cannot be applied to these complexes. The MRMP2 calculations indicate that the spin multiplicity increases upon going to Mn from Sc and reaches the maximum, nonet spin state, at Mn, and then suddenly decreases to singlet at Fe. This interesting change in spin multiplicity is discussed in terms of occupation of MOs.

In Chapter 3, inverted sandwich type complexes (ISTCs) of the second-row transition elements, $(\mu\text{-}\eta^6\text{:}\eta^6\text{-}C_6H_6)[M(DDP)]_2$ (DDPH = 2-(4-{(2,6-diisopropylphenyl)imino}pent-2-ene, *M* = Y, Zr, Nb, Mo, and Tc), were theoretically investigated with the DFT and MRMP2 methods, where model compounds, $(\mu\text{-}\eta^6\text{:}\eta^6\text{-}C_6H_6)[M(AIP)]_2$ (AIPH = (Z)-1-amino-3- imino-prop-1-ene), were mainly employed. When going to the right-hand side from the left-hand side in the second-row transition metal (TM) series of the periodic table, the spin multiplicity of the ground state increases in order singlet, triplet, and quintet for *M* = Y, Zr, and Nb, respectively. However, it decreases to singlet spin states for both *M* = Mo and Tc. The maximum spin multiplicity in the ground state is quintet which is presented by Nb, group 5 metal, in the

second-row TM complexes. This is in contrast to the first-row TM complexes, in which the maximum spin multiplicity was previously reported to be nonet for *M* = Mn, group 7 metal. Because the spin multiplicity is septet in the ISTC of Cr but singlet in that of Mo, the author investigated the ISTC of Mo in detail and discussed this interesting difference in the spin multiplicity between the ISTCs of Cr and Mo.

In Chapter 4, the free iterative complements interaction (ICI) method based on the scaled Schrödinger equation has been applied to the calculations of very accurate wave functions of hydrogen molecule in an analytical expansion form. All the variables were determined with the variational principle by calculating the necessary integrals analytically. The initial wave function and the scaling function were changed to see the effects on the convergence speed of the ICI calculations. The free ICI wave functions that were generated automatically were different from the usual wave functions and this difference was shown to be physically important. The best wave function reported in this chapter seems to be the best worldwide in the literature from the variational point of view. The quality of the wave function was examined by calculating the nuclear and electron cusps and other properties.

In Chapter 5, the author introduced the exponential integral (Ei) function for variationally solving the Schrödinger equation of helium and its isoelectronic ions with the free iterative complement interaction (ICI) method. In the previous study of helium atom, Nakashima and co-workers could calculate very accurate energies of these atoms by using the logarithmic function as the starting function of the free ICI calculation. The Ei function has a weak singularity at the origin, similarly to the logarithmic function, which is important for accurately describing the three particle coalescence region. The logarithmic function, however, has a node and a maximum along the radial coordinate, which may be physically meaningless. In contrast, the Ei function does not have such unphysical behaviors and so would provide an improvement over the logarithmic function. Actually, using the Ei function, instead of the logarithmic function, the author obtained the energy, *E* = **-2.903 724 377 034 119 598 311 159 245 194 404 446 696 924** 865 a.u. for the helium ground state with 21035 functions, which is a slight improvement over Nakashima's best result (the bold face shows the digit that is believed to have converged). This result supports that the Ei function is a better function than the logarithmic function for describing the three particle coalescence region.

As mentioned in General Introduction, elucidation and prediction are important goals of theoretical science. The author believes that his study in Part I could partially achieve to reach the goals. However, if the author is asked whether or not he *really* believes that his prediction and/or elucidation can be achieved in all chemical issues, he must answer "NO". It is because our method is based on inclusion of various approximations such as neglect of solvent or packing, statistical effect, motion of nuclei, *etc*. The only way to reach the truth as close as possible is to employ approximations as less as possible, which was developed in Part II. Application of our method is limited to very small systems now. In other words, it does not contribute to our everyday life yet. The author believes, however, that theoretical chemistry will develop a lot from now and it will bring us a revolutionary change in chemistry and our everyday life in the future, like the Newton's mechanics did.

List of Publication

Publications included in the thesis

Chapter 1

"Bonding Nature of Open-Lantern-type Dinuclear Cr(II) Complexes. Theoretical Study with the MRMP2 Method"

Yusaku I. Kurokawa, Yoshihide Nakao, Shigeyoshi Sakaki

J. Phys. Chem. A **2009** 113(13) 3202–3209.

Chapter 2

"Inverted Sandwich Type Dinuclear Chromium(I) Complex and Its Analogues of Scandium(I), Titanium(I), Vanadium(I), Manganese(I), and Iron(I): Theoretical Study of Electronic Structure and Bonding Nature"

Yusaku I. Kurokawa, Yoshihide Nakao, Shigeyoshi Sakaki

J. Phys. Chem. A, **2010**, 114 (2) 1191–1199

Chapter 3

"Inverted Sandwich Type Complexes of Second Row-Transition Metal Elements: Theoretical Prediction of Electronic Structures and Spin Multiplicities"

Yusaku I. Kurokawa, Yoshihide Nakao, Shigeyoshi Sakaki

To be submitted

Chapter 4

"Free ICI (Iterative Complements Interaction) Calculations of Hydrogen Molecule"

Yusaku Kurokawa, Hiroyuki Nakashima, Hiroshi Nakatsuji

Phys. Rev. A, **2005**, 72(6) 062502-1 – 062502-11

Chapter 5

"Solving the Schrödinger equation of helium and its isoelectronic ions with the exponential integral (Ei) function in the free iterative complement interaction method"
Yusaku I. Kurokawa, Hiroyuki Nakashima, Hiroshi Nakatsuji
Phys. Chem. Chem. Phys. **2008**, 10, 4486–4494

Other publications

"Solving the Schrödinger Equation of Atoms and Molecules without Analytical Integration Based in the Free Iterative-Complement-Interaction Wave Function"
H. Nakatsuji, H. Nakashima, Y. Kurokawa, and A. Ishikawa
Phys. Rev. Lett. **2007**, 99, 240402-1 - 240402-4